

Low-Profile Wideband Antenna Arrays for Mobile Satellite and 5G Communication



Swansea University
Prifysgol Abertawe

Benjamin J. Falkner

Faculty of Science and Engineering

Swansea University

2023

Submitted to Swansea University in fulfilment of the requirements for the degree of

Doctor of Philosophy

Copyright: The Author, Benjamin J. Falkner, 2023

Abstract

Three innovative low-profile antenna arrays are designed and tested for vehicular satellite and 5G communication. All of the systems presented target key challenges of GEO, LEO and 5G communication. Each design provides a high level of performance for the given application in a far more compact and lower cost design than existing systems.

Firstly, a wideband curl antenna array is developed to enable L-band GEO satellite communication for emergency vehicles. This novel 1×3 rotated array utilises a hybrid switch beam and phase shifting technique to enable full beamforming down to 70° in all directions with 40% lower cost than standard phased array systems. Uniquely, this provides excellent azimuth beam steering at low angles from a linear array. This system also utilises a high impedance surface to reduce the height of the antenna elements by 50% compared to existing curl antenna designs.


Secondly, a shared aperture antenna array is developed to enable Ka-band LEO satellite communication for vehicular integration. This system utilise a new combination of circular polarised triangular antennas in an interlaced planar triangular lattice such that the topology provides optimal tessellation. As a result, the system provides high performance beam steering and reconfigurable circular polarisation in a highly compact design. This array has been developed such that it is suitable for common PCB manufacturing methods. Unlike existing shared aperture arrays for LEO terminals, this topology enables reconfigurable circular polarisation in a single, planar PCB structure.

Finally, a low-cost wideband compressed spiral antenna array is designed and fabricated for global 5G ground-to-air communication for aircraft. An innovative spiral antenna optimisation is presented where the spiral is highly compressed such that it can provide an axial beam over a wide bandwidth while maintaining a lower profile than existing wideband solutions.

Keywords: Smart antenna, Vehicular antenna, Antenna arrays, Satellite Communication, LEO communications, GEO communication, 5G Antenna.


Declarations

This work has not previously been accepted in substance for any degree and is not being concurrently submitted in candidature for any degree.

Signed. 

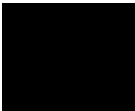
Date: 20/03/23

This thesis is the result of my own investigations, except where otherwise stated. Other sources are acknowledged by footnotes giving explicit references. A bibliography is appended.

Signed.. 

Date 20/03/23

I hereby give consent for my thesis, if accepted, to be available for photocopying and for inter-library loan, and for the title and summary to be made available to outside organisations.

Signed. 

Date 20/03/23

The University's ethical procedures have been followed and, where appropriate, that ethical approval has been granted.

Signed. 

Date 20/03/23

Acknowledgments

I would like to thank my supervisor, Professor Amit Mehta, for the opportunities, valuable support and thorough advice I have benefited greatly from throughout my PhD.

I would also like to thank my colleague, Dr. Hengyi Zhou, who's support, guidance and constructive debates has been invaluable throughout my candidature.

I also owe a great deal of thanks to Professor Nakano and Professor Mirshekar-Syahkal for their help and advice in the writing of my published journal papers.

Finally, I would like to thank my family for their moral support and my partner for their patience.

Table of Contents

Chapter 1. Introduction	1
1.1 5G Mobile Communication	1
1.2 Satellite Communication.....	3
1.3 Next Generation Vehicle Communication	5
1.4 Objectives of This Work	6
Chapter 2. Principles of Antennas & Wireless Communications	9
2.1 A Brief History of Wireless Communication.....	9
2.2 Fundamental Antenna Theory and Parameters	10
2.2.1 Antennas	10
2.2.2 Basic Antenna topology	11
2.2.3 Antenna Impedance	12
2.2.4 Antenna Efficiency	13
2.2.5 Reflection Efficiency & The Reflection Coefficient	14
2.2.6 Scattering Parameters.....	15
2.2.7 Material Efficiency	16
2.2.8 Radiation Pattern.....	16
2.2.9 Microstrip Antennas.....	23
2.2.10 Antenna Arrays.....	25
2.2.11 Antenna Simulation.....	26
Chapter 3. L-Band Beam Switching Antenna Array for GEO Satellite Applications	27

3.1	Existing Work	28
3.2	Quad-Arm Curl Antenna with HIS (QACH)	38
3.2.1	Element Design.....	38
3.2.2	Element's Results.....	42
3.3	1×3 QACH Antenna Array.....	44
3.3.1	Array Design.....	44
3.3.2	Array Performance Verification	46
3.4	Discussion	49
Chapter 4. Ka-Band Split & Shared Aperture Antenna Arrays for LEO Satellite Communication		
.....		51
4.1	Existing Work	52
4.2	Ka band LEO antenna array target requirements and limitations.....	58
4.3	Spilt Aperture Antenna Element Design	59
4.3.1	Design Requirements	59
4.3.2	Receive Antenna Design and Results	60
4.3.3	Transmit Antenna Design and Results	64
4.4	Spilt Aperture Antenna Array.....	67
4.4.1	Antenna array topology optimisation.....	67
4.4.2	Receive antenna array design and simulation.....	69
4.4.3	Transmit antenna array design and simulation	71
4.5	Spilt Aperture Antenna Array Prototype Measurements and Results	73
4.5.1	Receive measured results.....	73

4.5.2	Transmit measured results	77
4.6	Shared Aperture Antenna Array	80
4.6.1	Receive Element Design	81
4.6.2	Transmit Element	84
4.6.3	Shared Aperture Antenna Array Design	87
4.7	Shared Aperture Antenna Array Simulated Results	88
4.7.1	Receive Sub-Array	88
4.7.2	Transmit Sub-Array	89
4.8	Discussion	90
Chapter 5. Wideband 5G Antenna Array for Air-to-Ground Communication		93
5.1	Ground-to-Air Requirements and Challenges	94
5.2	Existing Work	95
5.2.1	Antenna Elements	95
5.2.2	Wideband Antenna Arrays	99
5.2.3	Proposed Solution	106
5.3	Antenna Element Design	107
5.3.1	Antenna Element Structure	107
5.3.2	Spiral Compression and Height Optimization	108
5.3.3	Single-arm spiral simulation & experimental validation	112
5.4	Compressed Single-arm Spiral Antenna Array in a Triangular Lattice Design	115
5.4.1	4×4 Array Design	115

5.4.2	Antenna Feeding Network and Beam Steering Measurement.....	116
5.5	Discussion.....	120
Chapter 6. Conclusion & Discussions		122
6.1	Low-Profile L-Band Switch Beam Phased Array	122
6.2	Ka-Band Shared Aperture Array with Reconfigurable Circular Polarisation 123	
6.3	Wideband Compressed Spiral Array for Global Mid-Band 5G.....	125
6.3.1	Summary.....	125
List of Figures.....		127
List of Tables.....		136
References.....		137

Papers Published by Author Through PhD

Journal Papers

B. J. Falkner, H. Zhou, A. Mehta, T. Arampatzis, D. Mirshekar-Syahkal and H. Nakano, "A Circularly Polarized Low-Cost Flat Panel Antenna Array With a High Impedance Surface Meta-Substrate for Satellite On-the-Move Medical IoT Applications," in *IEEE Transactions on Antennas and Propagation*, vol. 69, no. 9, pp. 6076-6081, Sept. 2021, doi: 10.1109/TAP.2021.3070011.

B. J. Falkner, H. Zhou, W. Zhang, G. Metaxas, A. Mehta, V. Ziegler, T. Multerer, D. Mirshekar-Syahkal and H. Nakano, "A Low-Profile Wideband Compressed Single-arm Spiral Antenna Array for Mid-band 5G Beam Steering Applications," in *Nature Scientific Reports*, vol. 12, no. 1, pp. 13790, doi: 10.21203/rs.3.rs-1597307/v1.

N. Litov *et al.*, "Radar Cross Section Analysis of Two Wind Turbines via a Novel Millimetre-Wave Technique and Scale Model Measurements," in *IEEE Access*, vol. 10, pp. 17897-17907, 2022, doi: 10.1109/ACCESS.2022.3148064.

Conference Papers

B. Falkner, H. Zhou, S. Singh and A. Mehta, "A Dual-Band Polarisation-Reconfigurable Half E-Shaped Antenna Array for Q-Band Applications," *2020 IEEE International Symposium on Antennas and Propagation and North American Radio Science Meeting*, 2020, pp. 215-216, doi: 10.1109/IEEECONF35879.2020.9329571.

B. Falkner, H. Zhou, W. Zhang, A. Mehta, V. Ziegler and T. Multerer, "A Low-Profile Ultra-Wideband Spiral Antenna Array for Global Mid-band 5G Aerospace Applications," *2021 15th European Conference on Antennas and Propagation (EuCAP)*, 2021, pp. 1-3, doi: 10.23919/EuCAP51087.2021.9411055.

B. Falkner, H. Zhou and A. Mehta, "A Machine Learning Based Traveling Wave Antenna Development Methodology," *2021 IEEE International Symposium on Antennas and Propagation and USNC-URSI Radio Science Meeting (APS/URSI)*, 2021, pp. 2040-2041, doi: 10.1109/APS/URSI47566.2021.9704305.

B. Falkner, H. Zhou, A. Mehta and A. Modigliana, "Flat Panel Interlaced Shared Aperture Antenna Array for LEO Ka-band High Throughput Satellite Communication Applications," *2021 IEEE International Symposium on Antennas and Propagation and USNC-URSI Radio Science Meeting (APS/URSI)*, 2021, pp. 777-778, doi: 10.1109/APS/URSI47566.2021.9704197.

S. Singh, H. Zhou, B. Falkner, A. Mehta and A. Modigliana, "A Hybrid Rx/Tx Phased Array Antenna With a Spiral Lattice for Sidelobe Level Reduction," *2020 IEEE International Symposium on Antennas and Propagation and North American Radio Science Meeting*, 2020, pp. 1837-1838, doi: 10.1109/IEEECONF35879.2020.9330418.

W. Zhang *et al.*, "3D Metal Printed Polarization Reconfigurable Horn Antenna with Solid & Meshed Structures: Future works for SATCOM applications," *2020 IEEE International Symposium on Antennas and Propagation and North American Radio Science Meeting*, 2020, pp. 1501-1502, doi: 10.1109/IEEECONF35879.2020.9329613.

Chapter 1.

Introduction

In wireless communications today, the role of vehicles in communication networks are growing rapidly and there is an increasing focus on vehicular antennas and communication to enable this development. Cars, for instance, have gone from mainly mechanical vehicles with simple forms of wireless communication (radio, mobile telephony etc.) to all-singing all-dancing “*computers on wheels*” [1]. That is, cars are now built with high-speed computing devices capable of delivering up-to-date traffic information, entertainment, cloud computing and general internet access. There is now an expectation from all types of users that modern cars provide the same quality of service and functionality as a home broadband connection. It is therefore vital that such vehicles are capable of receiving reliable, high speed internet access in any location.

1.1 5G Mobile Communication

The obvious method for providing internet access for vehicles is existing terrestrial 5G networks. These networks are capable of providing high speed, low latency wireless internet access. Unlike the previous generation 4G standard, the 5G standard employs several methods of increasing capacity and speed. Firstly, while 4G uses sectorised base station cells where only a section of the overall licensed spectrum is used in any particular area to avoid interference, 5G revolutionises frequency reuse by generating targeted pencil beams on a per-user basis, allowing each user to be provided greater bandwidth without risk of interference. Secondly, 5G utilises mmWave frequencies (>24 GHz) alongside lower frequencies to enable far greater

communication speeds as, at higher frequencies, a greater amount of data can be sent over the same period of time. Of course, mmWave frequencies would fatally limit the range of a 4G system as such systems use wide beamwidth antennas with low directionality. At high frequencies, increased absorption of the signal in the atmosphere [2] will result in the received signal being overwhelmed by noise in the surrounding environment by the low directivity antenna. However, beamforming is implemented in 5G systems so as to reduce noise in the received signals from undesirable directions such that the range at mmWave frequencies are greatly increased over a 4G system. As a result, mmWave 5G base stations can provide coverage in small cells that each provide access for approximately the length of a street. These mmWave 5G systems are highly compact and so can be fairly simple to build, particularly in urban areas.

While 5G network access is growing at a remarkable pace [3], there are still limits to the coverage capability of the standard. As previously mentioned, high frequency 5G has a limited range and, in order to ensure low latency, requires a direct optical fibre connection at each base station. This is not a major issue for urban centres where base stations can be easily added to existing buildings and optical fibre networks have already been installed. However, in rural areas the cost of such systems can become exponentially more expensive as optical fibre must be specially laid to each base station. Furthermore, as there is a lower density of users in rural areas, the cost per customer will be far greater when compared to an urban area. Due to these challenges, providing universal 5G coverage is entirely unfeasible.

Moreover, even if full land coverage of 5G were possible, because the 5G standard allows for a wide range of frequencies to be utilised, it is up to government bodies to unilaterally decide which frequencies to dedicate to the technology. As a result, different regions and countries have selected different licenced bands for utilisation (e.g., 3.4 - 3.8 GHz in the EU and 3.7 - 5 GHz in the USA) [4]. This is a significant issue, particularly for aircraft

regularly traveling between countries and regions, as they therefore need to be able to cover a very wide range of frequencies to achieve true global operability.

1.2 Satellite Communication

Satellite communication provides an attractive alternative for vehicular internet access as, unlike 5G, there is no requirement for complex and large physical networks on the ground. Indeed, satellite networks (often called constellations) with wide areas of coverage are already commonplace in a number of industries. For example, satellite broadcasting of television is widely available without the need for local infrastructure. In maritime industries, satellite internet and radio is a vital part of communication, as it enables reliable communication when no other internet infrastructure is available. Both of these systems utilise satellites in geostationary orbit (GEO) which have historically been very popular for two primary reasons. Firstly, as these systems are geostationary, the satellites provide coverage to a consistent and targeted location. This allows for easy targeting by ground terminals and limits the need for handover between satellites. Secondly, due to the distance between the geostationary orbit and the earth, global coverage is easily obtainable with only a handful of satellites. However, these systems have typically been limited in capacity when utilised for two-way communication, due to the large number of users per satellite. Further, as a result of the large distances involved, latency will always be high.

However, while GEO communication has succeeded in niche applications such as marine and military, the technology has had limited success in expanding to a wider market. This is predominantly due to technical challenges that have resulted in increased cost and size of ground terminals. As the GEO orbit is located around the equator, for many markets such as Europe, North America and China, the beam is required to steer down to just 20° above the horizon. This is a significant challenge for phased arrays and therefore most systems today utilise mechanical antenna movement. As a result, these systems are expensive, large and heavy

and hence, such systems have failed to access key markets that could benefit from satellite internet access.

The latest generation of satellite internet access currently in development has moved away from geostationary orbit and focused on Low Earth Orbit (LEO). LEO systems utilise hundreds of smaller satellites far closer to the earth's surface. As a result, LEO constellations can provide far greater capacity per user and lower latency than GEO constellations. While there is an increased cost in launching these constellations due to the high number of satellites, this is partly offset by the closer orbit and compact cube-sat design that allow for many satellites to be launched from a single rocket.

Compared GEO networks, LEO networks are far superior in terms of data rate and latency. The increase in data rate has partially been achieved by the utilisation of higher frequencies in the Ku – Ka-bands. LEO constellations do however require constant handover between satellites due to the far lower orbital period of satellite in LEO orbit. Compared to 5G networks, LEO networks do provide similar data rates but they are not able to provide the same ultra-low latency 5G can deliver.

However, such developments are not without their challenges. A particular struggle faced by the industry is the development of compact and low-cost terminal antenna arrays at the high frequencies utilised LEO networks. At K-band (18 GHz to 27 GHz), the antenna element and feeding structure of any system must become very small. As a result, there is a significant challenge in developing antenna array designs that provide effective performance while staying within the parameters of existing PCB fabrication techniques. Furthermore, many of the techniques used to enable necessary key benefits such as reconfigurable polarisation and a shared aperture are simply not possible at such high frequencies.

1.3 Next Generation Vehicle Communication

Given the compromises of existing technologies detailed here, it is likely that future vehicles will not rely on only a single form of wireless communication. Rather, vehicles will be compatible with a variety of communication types, predominantly 5G and satellite networks. For ground vehicles, 5G is preferable in urban environments due to the high speeds and low latency afforded by the technology. In rural areas, where 5G coverage is inconsistent or non-existent, LEO satellite communication will provide a highspeed fall-back with a slight increase in latency compared to 5G. In some specialist cases GEO networks may also be utilised because of their reliability. The increased connectivity permitted will also allow vehicles to act as part of the network infrastructure, accessing internet via LEO satellites and distributing it to personal devices in or around the vehicle via 5G or Wi-Fi.

Such an approach is also beneficial for aircraft where hybrid internet is already in use. In areas such as Europe with terrestrial mobile networks, LTE internet access is streamed to aircraft via the European Aviation Network [5] and then, when the aircraft crosses large bodies of water, the aircraft can switch to satellite communication. These systems, however, still rely on LTE network standards instead of higher capacity 5G technology. Yet, as already mentioned, the switch to 5G will require aircraft to cover very wide bandwidth.

It is for these reasons that it is inevitable that both aircraft and ground vehicles will require the integration of many antennas and antenna arrays. Many existing solutions rely on mechanical components or high-profile antenna element structures. This not only impacts the ease of integration into such vehicles, but also impacts the efficiency of the vehicles. The increase in drag caused by large antenna designs will greatly impact the fuel use of aircraft and the range of electric cars. It is for this reason that existing antenna designs can severely limit the ability to integrate such systems. Therefore, it is vital to ensure that any antenna system introduced to the market is effective whilst also retaining a low profile and low cost. This is a

key challenge facing both industry and academia as beamforming becomes a widespread component of wireless network design.

1.4 Objectives of This Work

This work investigates areas of beam steering communication where, due to the limitations in antenna design, existing systems struggle to meet key performance requirements while remaining compact. Here, innovations are present in three key applications of vehicular terminal antennas: L-band GEO satellite communication; Ka-band LEO satellite communication and ground-to-air mid-band 5G.

Firstly, in Chapter 2, a history and the fundamental principles of wireless communication and antenna design is presented.

Chapter 3 presents a compact antenna array for L-Band communication utilising the Inmarsat BGAN network. Here, emergency vehicles are the key consideration as there is a clear need for consistent and reliable communication in this application. However, for full terminal coverage of the Inmarsat BGAN network, beam steering to $20^\circ < \theta < 70^\circ$ from the antenna boresight is required. Firstly, the existing solutions for vehicular L-band GEO communication are investigated. Most existing systems available rely on mechanical movement of the antenna. The size, weight and cost of such systems make them almost impossible to be fully adopted by emergency services. This chapter then presents a novel Quad-Arm Curl with a High impedance surface (QACH) array that enables the purely electronic beam steering to all required angles in a highly compact and low-cost system, ideal for the target application. To achieve this, two innovative techniques have been implemented. Firstly, a High Impedance meta-Surface (HIS) has been designed that reduces the antenna height by 50%. Secondly, the unit antenna elements have been placed in a rotated linear array that enables accurate beam steering across all azimuth angles. This is believed to be the first compact linear array with the azimuth beam steering performance presented here.

Chapter 4 presents a split aperture antenna array design suitable for vehicular integration and fabrication with existing PCB manufacturing techniques. This is then prototyped and verified to ensure the accuracy of the design and fabrication. A shared aperture design is then presented that provides similar performance to the split aperture design but in a greatly reduced footprint. This is enabled by utilising a novel combination of circular polarised triangular antenna elements in an interlaced triangular array lattice with sequential rotation. This combination allows for optimal tessellation of the receive and transmit antenna elements on a single plane to greatly improve beamforming capability. This is achieved while utilising the prototyped PCB structure and parameters such that it can be fabricated with commonly used PCB manufacture techniques without risking the functionality of the fabricated board. This is a vital improvement over existing state of the art systems that require a multi-layer antenna array structure and often cannot provide polarisation reconfigurability.

Chapter 5 presents an investigation into global ground-to-air 5G communication for aircraft. As previously explained, each country and region has licensed different bands within the 5G spectrum. The challenge today is to provide suitable beam steering for the application over the entire bandwidth required for all countries. Several leading works are investigated and found to be limited in either beam steering capability or the profile of the antenna (limiting integration into the vehicle). A design for a novel compressed spiral antenna array is then presented that can provide the required beam steering from 3.3 GHz to 5 GHz in a low profile and low cost antenna design. Here, an innovative approach to spiral antenna design is presented where the spiral antenna is compressed and placed on a low-profile substrate such that an axial beam pattern over a wide bandwidth is achieved. As a result, when placed in an antenna array, the design provides excellent beam steering performance over a wide bandwidth in a lower profile than any existing antenna array design suitable for the application.

Finally, Chapter 6 presents the final conclusions of the work and highlights the key innovations presented.

Chapter 2.

Principles of Antennas & Wireless Communications

2.1 A Brief History of Wireless Communication

The history of wireless communication is widely understood to have begun in 1842 when Joseph Henry, during his experimentation with magnetic induction, found that an electric current could be induced wirelessly [6]. Initially, Henry's experiments allowed him to magnetise a needle between two identical circuits over a distance of 30 feet. After further experimentation he was able to detect a flash of lighting over many miles and induce a signal in a telegraph line over 220 feet. While these initial experiments were somewhat limited in practical purpose, they demonstrated the existence of electromagnetic (EM) waves and their potential for wireless communication.

It would not be until 1864 that James Clerk Maxwell mathematically described electromagnetic waves, their generation and their interaction [6]. In 1888, Heinrich Hertz would verify these theories practically. Hertz also went further by describing the polarisation of an EM field and develop and early loop antennas.

In 1891, Thomas Edison patented a "Means for transmitting signals electrically" [7]. This induction-based system utilized two large antennas placed at a high altitude to transmit an electrical signal over long distances. He proposed using such a design for communicating with marine vehicles.

Central to this work, in 1889, Sidney Brown first proposed using two elements in close proximity to provide a higher level of directivity [8]. It was then Karl Ferdinand Braun who, in 1906, proposed the use of phase to electronically direct a wireless signal [8]. Thus, the first phased array was developed.

Since the start of the 20th century, these early developments and theories have revolutionised how we communicate and how society functions. Radio broadcasting, first started in 1906, has enabled instant communication over almost any distance. During World War II, Sydney Brown's antenna array concept was utilised to great effect to create the RADAR system that allowed for detection of aircraft long before it was visible to the naked eye. Today almost 5 billion people have access to the internet [9]. Throughout this ground-breaking progress, antenna development has been at the heart of innovation by enabling new radiation methods, increased gain, wider bandwidths, lower cost and extremely compact designs.

2.2 Fundamental Antenna Theory and Parameters

2.2.1 Antennas

As defined by Kraus and Marhefka [10], a radio antenna is *“the structure associated with the region of transition between a guided wave and a free-space wave, or vice versa”*. That is to say, the antenna is a component that transitions a guided wave from a transmission line (be this a coaxial cable or waveguide) to free space. We can go further and summarise that what makes an antenna “good” is to achieve this transition *“as efficiently as possible, while at the same time the radiated power has a certain desired pattern of distribution in space”* [11]. With this definition of an antenna and our essential goal of antenna design, we can begin to explore the fundamental workings of an antenna, its place in a communication system and how we can measure its effectiveness. To provide a complete basis for analysis, this section will present a

few basic antenna configurations before detailing the key parameters and metrics that are central to antenna development.

2.2.2 Basic Antenna topology

Most standard antennas have three basic components: an excited conductor, a grounded conductor and a dielectric gap between these two. This is true for both early monopoles and more modern microstrip and horn antennas. Such designs are presented in Figure 1.

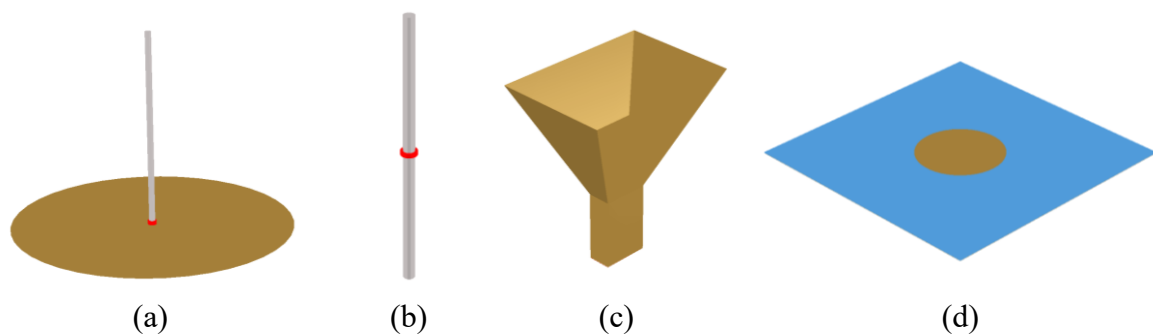


Figure 1. Three type of standard antennas: (a) monopole antenna, (b) dipole antenna, (c) horn antenna and (d) microstrip antenna

A monopole antenna is a wire antenna that consists of an excited wire and a ground plane. In large scale monopole antennas, the earth surface acts a suitable ground plane. It is closely related to a dipole wire antenna that uses a second ground wire mirrored below the excited wire to provide suitable coupling. Here, the air acts as a dielectric gap. Other wire antenna designs include helical and loop antennas.

Horn antennas can often take the form of a flared waveguide when excited directly from a waveguide but can also be fed via a coaxial probe. Here, the waveguide edge and horn itself is grounded, with an air gap between the excited probe and the ground.

A microstrip antenna consists of a thin layer of conductive material adhered to a thicker layer of dielectric material, and finally a ground plane adhered below that. Here the signal is fed to the top of the microstrip from the bottom by pin or coupled slot or alternatively from the

side via a co-planar waveguide. Microstrip can be used to design a wide variety of antennas, including reflector backed dipole antennas and patch antennas. They are a particularly practical due to their low-profile design and relatively simple fabrication.

2.2.3 Antenna Impedance

As with any electrical component, antennas have a complex impedance. Figure 2 displays the equivalent circuit of a microstrip antenna with a number of common feeding types. For example: Resistance can be affected by the resistivity of the conductor used or the dimensions of the design; Reactance can be created by the coupling between the antenna and ground. Structures such as tightly coupled antennas and meta-surfaces can be designed to provide further control of the overall impedance.

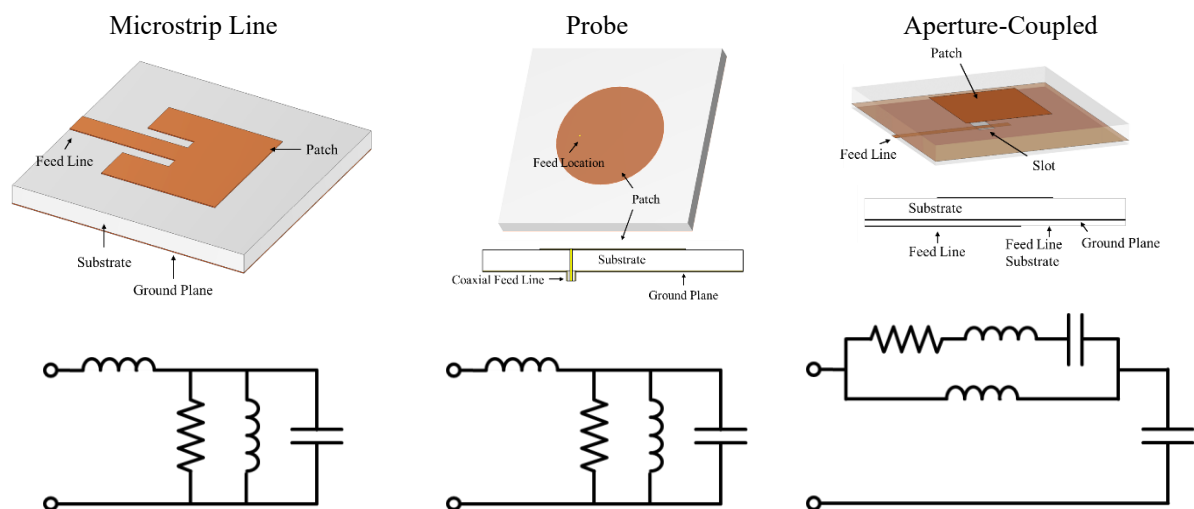


Figure 2. The equivalent circuit of a microstrip antenna with alternative feeding methods.

It is a general standard that transmission lines target 50Ω input impedance, as this value is found to provide a good balance between power handling and attenuation. Hence, an antenna design will normally target 50Ω to enable suitable matching. To aid impedance matching of an antenna and feeding network, a Smith chart can be utilised. An example of a Smith chart and its function is presented in Figure 3. Here the normalised impedances of the antennas in Figure 2 is shown. Invented in the 1930s by Phillip Hagar Smith, the Smith chart plots the relative

impedance of an antenna relative to the input impedance, such that a perfectly matched antenna will have relative impedance of 1. From such a plot, it is relatively simple to see where aspects of an antennas design could be altered to provide a better impedance match. For example, in Figure 3, the impedance matching of the microstrip antenna at 3 GHz is limited by a high capacitance component in its equivalent circuit. Reducing this capacitive component, by reducing the substrate height for example, could result in better impedance matching. Further, the impact of tuning stubs, quarter wave transforms and other matching techniques can be calculated in order to match the feeding transmission line to the antenna.

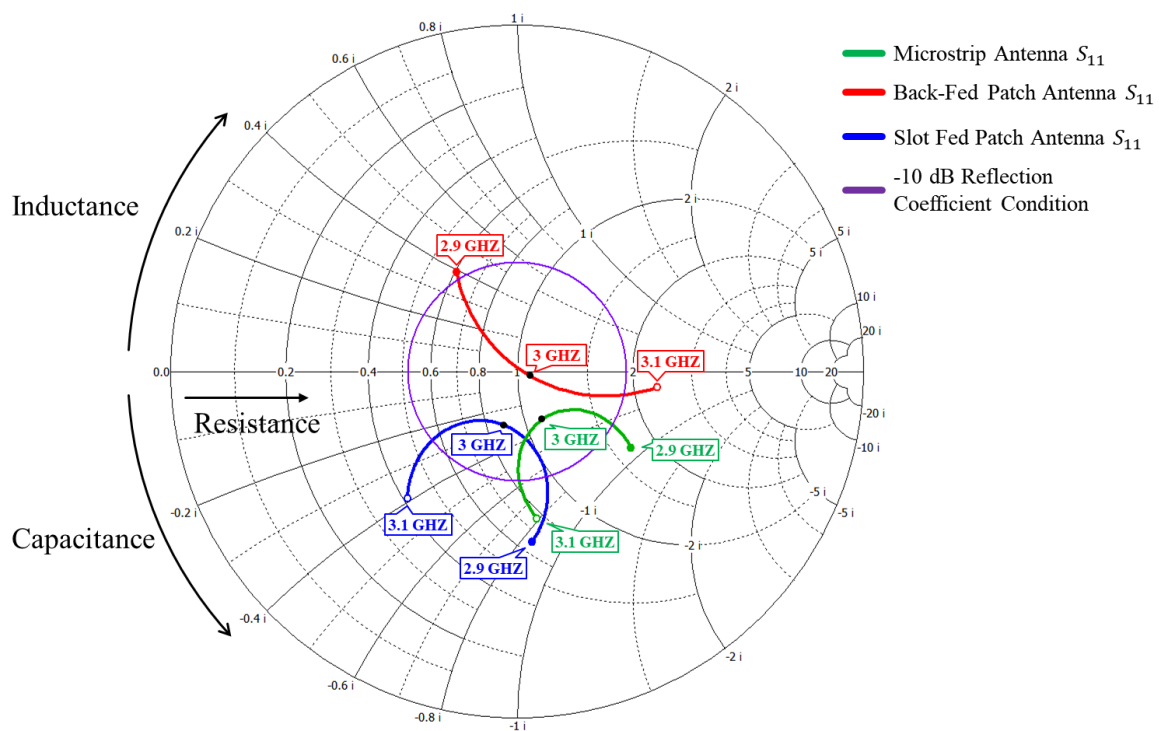


Figure 3. A Smith Chart displaying normalised impedance of the antennas shown in Figure 2 for the frequency range of 2.9 – 3.1 GHz. The reference circle for the -10 dB reflection coefficient is also shown.

2.2.4 Antenna Efficiency

As defined earlier, the efficiency of an antenna is perhaps the most important parameter to consider when designing an antenna.

The total efficiency of antenna (e_0) can be described as the sum of the reflection efficiency (e_r), the conduction efficiency (e_c), and the dielectric efficiency (e_d) [12]. However, the conduction and dielectric efficiency are almost impossible to separate in the measurement of an antenna as we can often only measure the total output power for the complete antenna design. Therefore these two values can be combined into a single material efficiency value (e_{cd}).

$$e_0 = e_r e_{cd} \quad (1)$$

2.2.5 Reflection Efficiency & The Reflection Coefficient

Reflection efficiency can be best understood through the lens of transmission line theory. A transmission line such as a coaxial cable or waveguide is “*a distributed parameter network, where voltages and currents can vary in magnitude and phase over its length*” [13]. Within standard transmission line theory, we typically encounter a generator, the transmission line itself and a load. In theory, this load could be any kind of electrical device. As the load, the antenna has a complex impedance that is characterised by its structure and geometry. Therefore, the key to any good antenna design is the optimisation of the antenna geometry to ensure a close match between the antenna impedance (Z_L) and the characteristic impedance of the transmission line (Z_0). As previously detailed, in an RF system an impedance of 50Ω is often targeted as this value provides a suitable balance between power capacity and attenuation.

Where there is a mismatch between these impedances, a percentage of the signal will be reflected back along the transmission line. This reflection percentage can be quantified by the reflection coefficient (Γ), which is the ratio of reflected voltage to the incident voltage,

$$\Gamma = \frac{V^-}{V^+} \quad (2)$$

We can also calculate the reflection coefficient directly from the characteristic impedance of the transmission line and the impedance of the antenna,

$$\Gamma = \frac{Z_L - Z_0}{Z_L + Z_0} \quad (3)$$

Because of this relation, when plotted on a Smith chart, it will appear as a perfect circle around the central value (1+j1). This is demonstrated in Figure 3 where a reflection coefficient of -10 dB is plotted. In this case the -10 dB bandwidth of the antennas would therefore be the frequencies of the normalised impedance that fall within this circle.

From the reflection coefficient, we can also derive the reflection efficiency (e_r) of the transition,

$$e_r = 1 - \Gamma^2 \quad (4)$$

The bandwidth of an antenna can be defined from the reflection coefficient, defined as the continuous range of frequencies for which the reflection coefficient is suitably low. It is common to use a reflection coefficient value of -10 dB as the benchmark by which to calculate the bandwidth.

The reflection coefficient can also be used to calculate the Voltage Standing Wave Ratio (VSWR),

$$VSWR = \frac{1+|\Gamma|}{1-|\Gamma|} \quad (5)$$

VSWR is the ratio between the node and anti-node of the standing wave formed in a transmission line and is sometimes used as an alternative measure of the impedance matching performance of an antenna.

2.2.6 Scattering Parameters

The reflection coefficient is an important variable for a singular antenna. However, when multiple antennas are used in a system or a single antenna requires multiple feed lines, it becomes only one part of the overall analysis. In these cases, the power transmitted by one port often be received and absorbed by another. To measure the isolation between ports as well as the reflection coefficient we use what is called a scattering matrix.

$$\begin{pmatrix} b_1 \\ b_2 \end{pmatrix} = \begin{pmatrix} S_{11} & S_{21} \\ S_{21} & S_{22} \end{pmatrix} \begin{pmatrix} a_1 \\ a_2 \end{pmatrix} \quad (6)$$

Equation 6 shows the scattering matrix for a two-port network. In this equation, a_i represent the incident waves and b_i represent the reflected waves for each port. The scattering parameters (often known as s-parameters) represent the relationship between these the incident and reflected waves for each measured port. The parameters S_{11} and S_{22} represent the reflection coefficient for port 1 and 2 respectively. The parameter S_{21} represents the ratio of the incident wave in port 1 to the wave received in port 2. This represents the isolation between these ports. The parameter S_{12} represents the isolation between port 1 and 2 when there is an incident wave at port 2.

2.2.7 Material Efficiency

The material efficiency of an antenna is determined by two factors: the conductive efficiency (e_c) and the dielectric efficiency (e_d). These describe the power lost in the antenna due to losses in an antenna's conductive materials and dielectric materials respectively. As detailed earlier, these values are often grouped to a single material efficiency e_{cd} . When designing an antenna material, efficiency can be improved via conductive and dielectric material selection or utilising air as a dielectric substrate.

2.2.8 Radiation Pattern

As stated at the start of this section, there are two primary goals of antenna design: efficiency and radiation pattern. Here, the categorisation, plotting and measurements regarding the radiation pattern of an antenna will be detailed. The radiation pattern of an antenna is defined as “*The spatial distribution of a quantity that characterizes the electromagnetic field generated by an antenna. (This) distribution can be expressed as a mathematical function or as a graphical representation. The quantities that are most often used to characterize the*

radiation from an antenna are proportional to or equal to power flux density, radiation intensity, directivity, phase, polarization, and field strength.” [14].

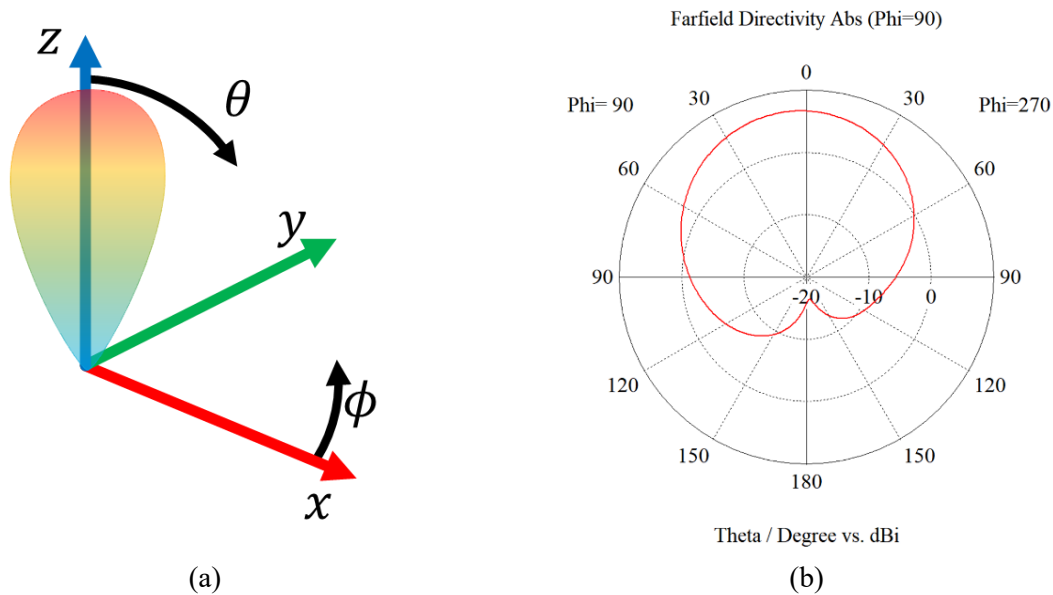


Figure 4. Antenna Pattern and Coordinates (a) in 3D and (b) via a 2D cut of the antenna pattern.

The radiation pattern can be plotted in 3D space as displayed in Figure 4 (a). Here, each coordinate angle is defined by the azimuth angle (ϕ) and the elevation angle (θ) as displayed in Figure 4(a). Typically (and exclusively in this work) the antenna plane will face towards the z axis. This angle perpendicular to the antenna plane is described as the boresight direction or axial direction. From this 3D pattern, 2D cuts of the radiation pattern can be taken over a constant θ or ϕ angle to provide a 2D plot of the pattern, as displayed in Figure 4(b).

There are three general categories of radiation pattern: Isotropic, Omnidirectional and Directional, (Figure 5). Isotropic antenna patterns are a purely theoretical concept where power radiates in all directions equally. In a directional pattern, power radiates predominantly in one direction. An Omnidirectional pattern radiate in all directions in one plane, and only in two directions in the other plane. Thus, creating an antenna pattern resembles a torus in shape.

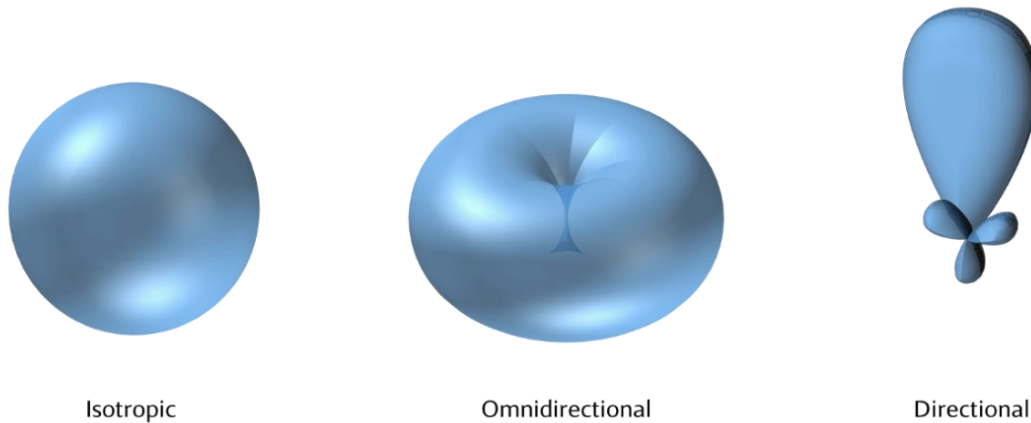


Figure 5. The three broad categories of radiation patterns

2.2.8.1 Antenna pattern characteristics

In an antenna pattern there are a number of characteristics and terms that allow us to glean useful analysis of an antenna's performance. A labelled diagram of an antenna pattern is displayed in Figure 6.

The first and most obvious aspect of an antenna pattern are the various lobes produced. These radiation lobes are a “*portion of the radiation pattern bounded by regions of relatively weak radiation intensity*” [12]. The largest of these lobes is the major or main lobe (also sometimes referred to as the Main Beam). More accurately the main lobe is defined as “*the radiation lobe containing the direction of maximum radiation*” [14]. In a standard patch antenna, this lobe is perpendicular to the plan of the antenna. The key characteristic of the main lobe, aside from its maximum value, is the beamwidth of the lobe. To measure this, the half-power beamwidth or 3 dB beamwidth is often utilized. The half power beamwidth is the “*angle between the two directions in which the radiation intensity is one-half the maximum value*” [14].

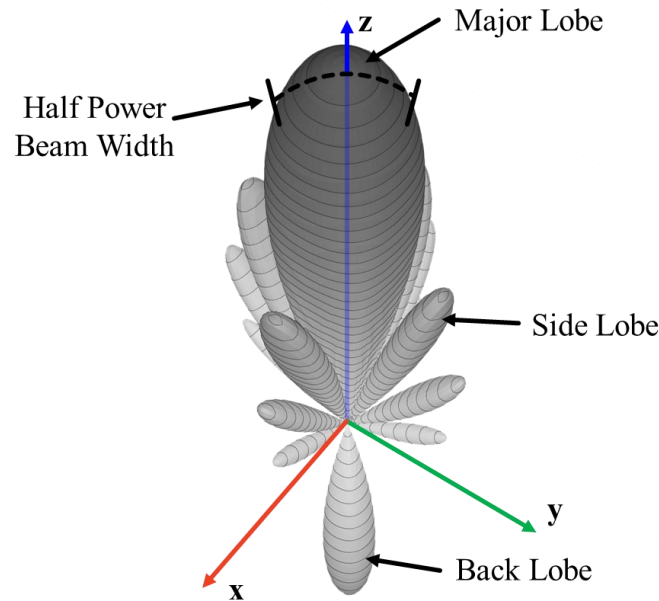


Figure 6. Anatomy of a radiation pattern.

Aside from the major lobe there are a number of smaller lobes. These are known as minor lobes or side lobes. In the opposite direction of the main lobe, a back lobe can also occur. The ratio of the directivity or gain of the main lobe and back lobe is described as the front-to-back ratio.

2.2.8.2 Radiation Intensity

The radiation intensity (U) of the antenna in a given direction is simply the “*the power radiation from an antenna per unit solid angle*” [14]. This can be obtained by multiplying the radiation density by the distance from the antenna squared. The units of radiation intensity are watt per steradian W/sr. Thus, it can be expressed as so,

$$U = r^2 W_{rad} \quad (7)$$

where,

r = distance of the point of measurement from the antenna

W_{rad} = radiation density

As such, the radiation of an isotropic source can also be expressed,

$$U = \frac{P_{rad}}{4\pi} \quad (8)$$

2.2.8.3 Directivity & Gain

As radiation intensity can be affected by variables other than the antenna design (such as input power) it is common to instead plot the radiation of an antenna as directivity (D). Directivity is given by “*the ratio of the radiation intensity in a given direction from the antenna to the radiation intensity averaged over all directions*” [14] and is measured in dBi,

$$D = \frac{U}{U_0} = \frac{4\pi U}{P_{rad}} \quad (9)$$

Directivity has also historically been referred to a directive gain. Often, directivity is also used to describe the maximum directivity of an antenna. Therefore, when an angular coordinate of a measurement is not given, it can be discerned that the maximum directivity of an antenna is implied.

However, by plotting directivity we forgo any information about the efficiency of the antenna. In order to provide a single value that defines both the directivity of an antenna and reflection efficiency (but without regard for the input power) we can instead use gain (G). The IEEE standard definition for gain is “*the ratio of the radiation intensity in a given direction to the radiation intensity that would be produced if the power accepted by the antenna were isotopically radiated*” [14]. As with the definition itself, antenna gain is almost identical to directivity, except that it takes account of the power accepted by the antenna (the material efficiency). As such, we can express this mathematically as directivity multiplied by the material efficiency,

$$G(\theta, \phi) = e_{cd}D(\theta, \phi) \quad (10)$$

Again, as with directivity, gain can be used without a direction to indicate the maximum gain of the antenna.

Of course, this measure only takes account of the material efficiency and not the total efficiency of an antenna including the reflection efficiency. If we wish to account for the total efficiency of the antenna, we can instead use realised gain. This value is “*the gain of an antenna reduced by its impedance mismatch factor*” [14]. It can be expressed like so,

$$G_0(\theta, \phi) = e_0 D(\theta, \phi) \quad (11)$$

These three measures (directivity, gain and realised gain) are the most common measures used when plotting an antenna pattern as they can each provide useful data isolated from inconsistent and unnecessary variables.

2.2.8.4 Phase

So far in this work, the radiation pattern has been described only as a product of radiation intensity (in essence, its magnitude). However, there is a second vital component to the radiation pattern: the phase pattern. The phase pattern of an antenna is “*the spatial distribution of the relative phase of a field vector excited by an antenna*” [14]. It acts exactly as phase would act in any other context, that is, as a complex counterpart to the signal magnitude. This is vital regarding for beamforming theory, as explained later in this chapter.

2.2.8.5 Polarisation Pattern

The polarisation of a radiated wave is the “*property of an electromagnetic wave describing the time-varying direction and relative magnitude of the electric field vector, specifically, the figure traced as a function of time by the extremity of the vector at a fixed location in space, and the sense in which it is traced, as observed along the direction of propagation.*” [12]. There are three primary categories of polarisation: linear, elliptical and circular. Diagrams for these are shown in Figure 7. Linear Polarisation (LP) is the case where the electric field vector oscillates across a single plane. Circular Polarisation (CP) is the case where the electric field vector traces a circular path over time at a single point in space. This

can be described as Left-Hand Circular Polarisation (LHCP) where the path traced by the field vector is anti-clockwise from the point of view of the receiver and Right-Hand Circular Polarisation (RHCP) where this field vector is clockwise from the point of view of the receiver. As one would therefore expect, elliptical polarisation is the case where the field vector traces an ellipse over time. Elliptical polarisation can also be left hand or right hand polarised.

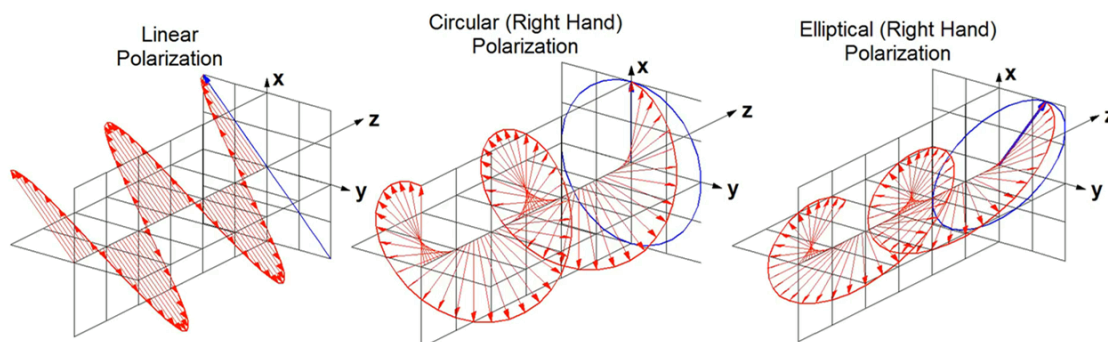


Figure 7. Three categories of polarisation. Diagram taken from [15].

When plotting the radiation pattern of an antenna, it can be beneficial to plot only radiation of a specific polarisation. Such a plot is not so different from plotting the total radiation magnitude in directivity or gain. However, when plotting circularly polarised directivity the unit will become decibel isotropic circular (dBic) to denote the circular polarisation of the radiation.

2.2.8.6 Axial Ratio

In order to differentiate and quantify circular and elliptical polarisation types, we can compare the major and minor axis of a wave. We can do so by calculating “*the ratio of the major to minor axes of a polarization ellipse*” [12]. This quantity is the Axial Ratio (AR),

$$AR = \left| \frac{E_y}{E_x} \right| \quad (12)$$

Hence, a perfectly circularly polarised wave will have an axial ratio value of 1, and a linear polarised wave will have an infinite axial ratio. In most applications we can consider an axial ratio level of less than 3dB (i.e., less than 50% difference between the major and minor axis) to be suitable for circular polarised communication links, as polarisation loss will be limited at this level. However, Chapter 3 discusses applications where this 3dB level is not a strict requirement.

2.2.9 Microstrip Antennas

Microstrip antennas encompass a wide variety of compact antennas that share similar physical design properties and fabrication methods. They generally comprise a thin layer of conductive material backed by a dielectric material and a ground plane, often fabricated using PCB fabrication techniques. While the general 2D structure is consistent, variations such as conductive layers between the substrate are sometimes used. Here, a few of the more common types of microstrip antennas will be detailed.

2.2.9.1 Patch Antennas

Patch antennas are a commonly used antenna for a variety of applications. Patch antennas consist of a conductive patch backed by a dielectric layer and a reflective ground plane. Such antenna designs are very popular as they are planar and compact, making them easy to integrate with mobile devices and vehicles. These antennas can be square, circular, elliptical or far more complex shapes. Patch antennas are resonant antennas i.e. they radiate around a single resonant frequency. This allows for fairly simple design, but it can significantly limit the bandwidth of the antenna. Patch antennas can be fed by a microstrip line or coaxial feed from below. Figure 8 shows a standard side-fed patch design.

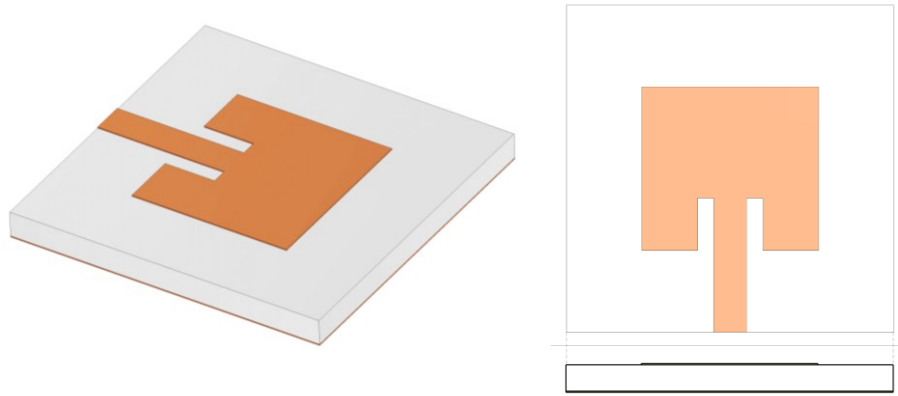


Figure 8. Common patch antenna design.

With proper mode selection, such antennas can radiate a broadside beam, conical beam, tilted beam or end-fire beam. Further, techniques such as slotted patches can be used for multi-band resonance, and quadrature feeding can be used to enable reconfigurable circular polarization. These variety of options have made patch antenna development an attractive area of innovation.

2.2.9.2 Planar Spiral & Curl Antennas

Spiral and curl antennas are not so commonly utilised as patch antennas because, for many current applications, patch antennas are quite adequate and simpler to design and fabricate. However, spiral and curl antennas can allow for far greater bandwidth as, unlike resonant antennas, spiral and curl antennas radiate via a traveling wave. A traveling wave antenna, such as a spiral is an antenna the excitation of which has a quasi-uniform progressive phase, as the result of a single feeding wave traversing its length only in one direction. This is achieved by properly terminating the antenna line such that reflections are minimised or eliminated. This traveling wave will change modes beyond $0.5\lambda_g$ to radiate energy out, this is known as the active region. By unitising a traveling wave mechanism, the bandwidth of the antenna can be greatly increased as the active region of the antenna will vary with frequency. Further, with careful design and optimisation, a phase shift can be induced across the spiral or curl so as to generate circular polarisation or a tilted beam.

2.2.10 Antenna Arrays

It was found early on in the design of antennas [8] that arrays could be utilised to improve the performance of a system. When two antennas are placed at a certain distance from one another in a planar fashion, the radiation of each antenna will interfere in an often-advantageous manner. Each antenna in an array is described as a unit element of the array.

When an array of two unit elements are excited with a uniform amplitude and phase, the radiation in the boresight direction will interfere constructively such that the radiation intensity in that direction will double. As the distance between antenna elements (d) is varied, the difference in phase between the radiation pattern of the two elements in any direction other than the boresight axis will change. Due to this, the distance between elements will determine the location and amplitude of side lobes in the antenna pattern. The distance between elements will also impact the beamwidth of the lobes such that, as the distance between elements is increased, the directivity of the main lobe will increase.

By altering the phase between the antenna elements, the angle of maximum constructive interference will move. This technique is known as beamforming or beam steering. The resultant pattern of an antenna array with a phase applied to each element can be calculated using the Array Factor (AF). Here, we use the frequency, antenna element spacing and excitation phase to calculate a resultant pattern of destructive and constructive interference in a given direction,

$$AF = \frac{\sin\left(\frac{N\psi}{2}\right)}{\sin\left(\frac{\psi}{2}\right)} \quad \text{where} \quad \psi = \beta d \cos \theta + \alpha \quad (13)$$

where:

N = Number of elements

θ = Calculated angle

β = Phase constant

$d = \text{Distance between elements}$

$\alpha = \text{Phase difference between elements}$

This result can be multiplied by the unit element antenna pattern to produce an estimated resultant pattern. By using directional antennas in an array, back-lobes will be significantly reduced. It should be noted that when two antenna elements are in close proximity to each other, the radiation pattern of each element can be significantly impacted by mutual coupling between the antennas. As a result, the array factor calculation should be treated only as an estimation instead of a physically accurate result. Beamforming calculations in this work have been calculated by simulating the antenna array as a whole, including mutual coupling, and then calculating the resultant array pattern from the accurate simulated unit element complex patterns.

As the phase is changed and the beam is steered to extreme angles, it is common for grating lobes to appear in the opposite ϕ direction to the main lobe. These grating lobes should be avoided in most cases as they will result in interference and increased noise. Grating lobe requirements can vary from application to application, but -10 dB is a common rule of thumb for most beamforming applications.

2.2.11 Antenna Simulation

All the antenna array simulation in this work has been achieved using CST Microwave Studio 2022 [16]. This is a 3D Electromagnetic (EM) simulator that is built to accurately calculate the electromagnetic characteristics of a given design. This software can provide accurate s-parameters and radiation patterns. CST Studio has also been used to calculate the result of beamforming by simulating the entire antenna array and combining the resultant element patterns with phase and amplitude variation.

Chapter 3.

L-Band Beam Switching Antenna Array for GEO Satellite Applications

In this chapter, an L-band antenna array is developed for Inmarsat BGAN internet access in emergency vehicles. Firstly, a review of the application and the existing state-of-the-art antenna designs are presented. Then, a solution to the challenges faced in this area is presented that achieves the required performance in a system that is lower cost and more compact than existing work.

Reliable connectivity is vital for emergency communication where an interrupted connection can have a major impact on precision, effectiveness and security of the service. As previously explained, vehicular communication today often relies on cellular networks [17] which, while providing low-cost connectivity over a wide area, suffers from regions with little or no coverage [3]. Hence, there is demand for a system that provides reliable communication with global coverage. For this reason, satellite communication is a natural fit for reliable and un-interrupted mobile connectivity.

The Inmarsat Broadband Global Area Network (BGAN) satellite constellation provides high speed internet access and near-global coverage [18], [19], [20]. It is an ideal candidate for device-to-cloud connectivity, especially for vehicular applications. This is because its services are relatively cheap, certified for medical applications and, importantly, it is fully functional globally today. Due to the geostationary (GEO) orbit of the BGAN satellite constellation, a beam steering range of $20^\circ < \theta < 70^\circ$ is required for most of Europe, Australia, China, India

and the United States [19]. For data rates of 340kbps, the BGAN terminals must have a gain greater than 6.5 dBic. However, steering to low elevation angles while maintaining a compact design is a significant challenge for on-the-move satellite terminals, both from a technological and commercial perspective.

3.1 Existing Work

Many existing commercial BGAN vehicular on-the-move systems use mechanical movement of the antenna to steer the beam to high elevation angles in order to maintain the required directivity [21], [22]. Unfortunately, these antenna systems are typically large, costly, and prone to wear due to their mechanical components.

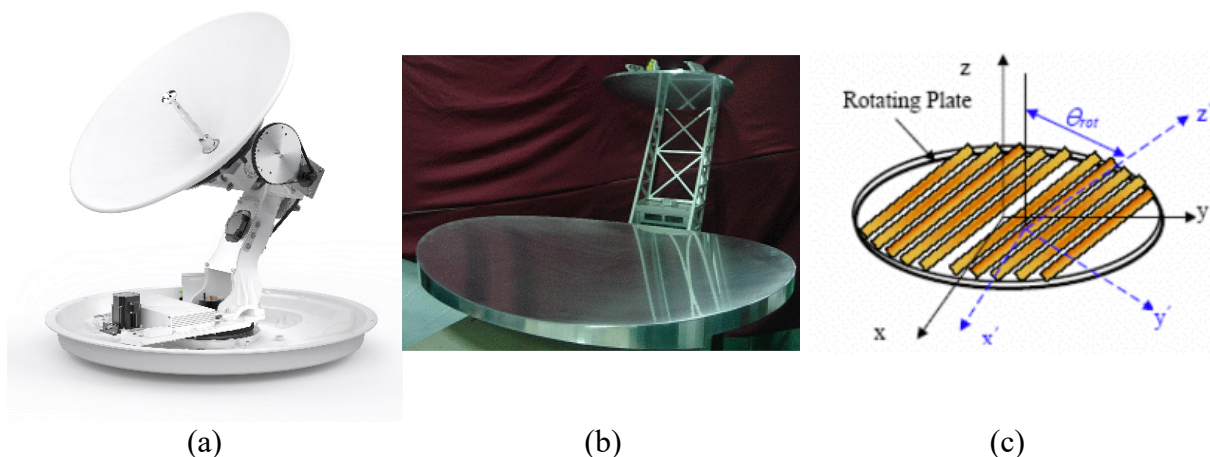


Figure 9. Three beamforming solutions for vehicular antennas. (a) Fully mechanical reflector antenna [23] (b) Hybrid mechanical and electronic reflector antenna [24] (c) Hybrid mechanical and electronic phased array antenna [25].

A popular solution in the current commercial markets are reflector antennas that are steered via a mechanical gimbal such as the Intellian GX60NX [23] shown in Figure 9 (a). These systems allow for consistent directivity at all angles and use gimbals to absorb any movement from the vehicle. However, these devices are large, heavy and expensive. Therefore, while GEO satellite systems are popular for marine applications, they are unsuitable for ground vehicles.

Hybrid systems that attempt to combine mechanical movement and limited electronic beamforming have been proposed. Reflector antenna systems such as [24] use a simplified system with reduced degrees of mechanical movement to enable the electronic beamforming to provide superior beamforming capabilities compared to a purely electronic system. However, hybrid reflector antennas still require a great amount of space and weight, and any cost saved on the gimbal can be easily exceeded by the electronic beamforming network.

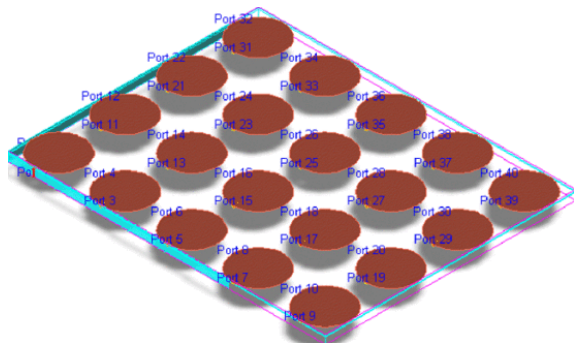


Figure 10. An electronic beam steering antenna array [26]

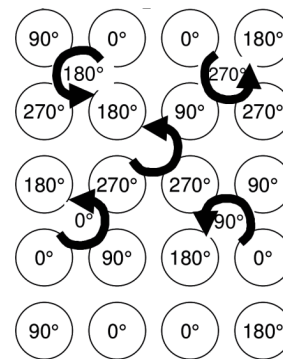


Figure 11. Sequential element rotation utilised to improve axial ratio at low steering angles [26]

A hybrid method has also been used to expand the range of a full phased array by the use of rotation on a single axis [25], as shown in Figure 9 (c). These systems are beneficial as they allow for expanded beam steering coverage while greatly reducing the profile over other mechanical systems. This does not necessarily lead to a reduction in cost however, as the increased cost of a full 2D phased array can be prohibitive.

A number of purely electronic alternatives have been proposed [27]. For example, an array designed for the purpose of BGAN was presented in [26] which was able to provide the required bandwidth and Right Hand Circularly Polarized (RHCP) beam steering down to 40° elevation. This was achieved using a 4×5 array of 61mm diameter patches as shown in Figure 10. In order to achieve circular polarisation, quadrature feeding of each patch is used. To complement this technique sequential element rotation is used to further improve the axial ratio of the array at lower steering angles and subdue mutual coupling. Figure 11 illustrates the sequential location method utilised. Here, within 2×2 sub arrays, each antenna is rotated by 90°

around the centre of the sub array. By properly applying a phase shift of $+$ or -90° to the array, the axial ratio of the resultant radiation will be reduced. Such a technique in a square lattice can result in increased back lobes when scanning but here sequential rotation of these 2×2 sub arrays is utilised to suppress this effect.

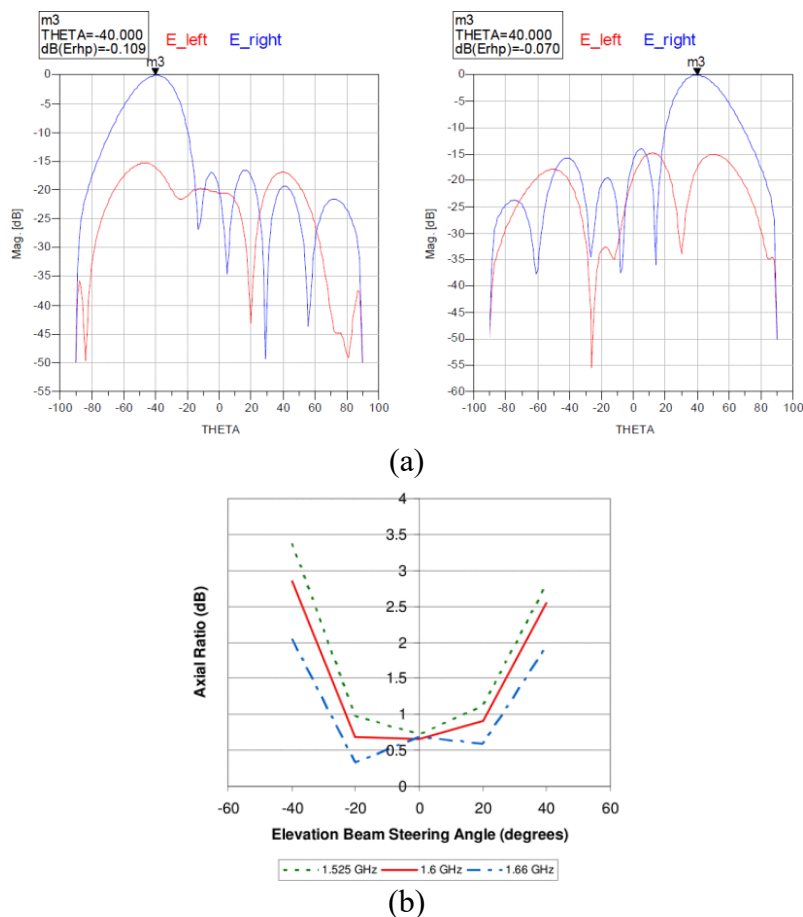


Figure 12. Beam steering capability of the antenna array presented in [19] (a) Fairfield of array beam at $\pm 40^\circ$ (b) Axial ratio of the array across elevation steering angles.

The key results of this design [26] are displayed in Figure 12. Here it is shown that grating lobes are suppressed to less than -13dB at elevation angles of 40° from the boresight. Further the axial ratio remains less than 3.5 GHz for the same elevation angles across the operational bandwidth. This is axial ratio suitable for most BGAN applications.

However, as mentioned above, the limited beam steering is not suitable for BGAN communication for much of the earth's surface. Furthermore, the feed circuit for such an array would require a total of 40 phase shifters and 20 High Power Amplifiers (HPA), Low Noise

Amplifiers (LNAs) and duplexers. With so many components required, the cost of the feed-network will raise the price of the overall system significantly.

Given that the BGAN network only requires RHCP, it may be possible to implement patches that are naturally circularly polarised such as those used in [28]. This antenna design could reduce the number of phase shifters required by 50%. However, such a design could impact the polarisation isolation over the operation bandwidth of the antenna.

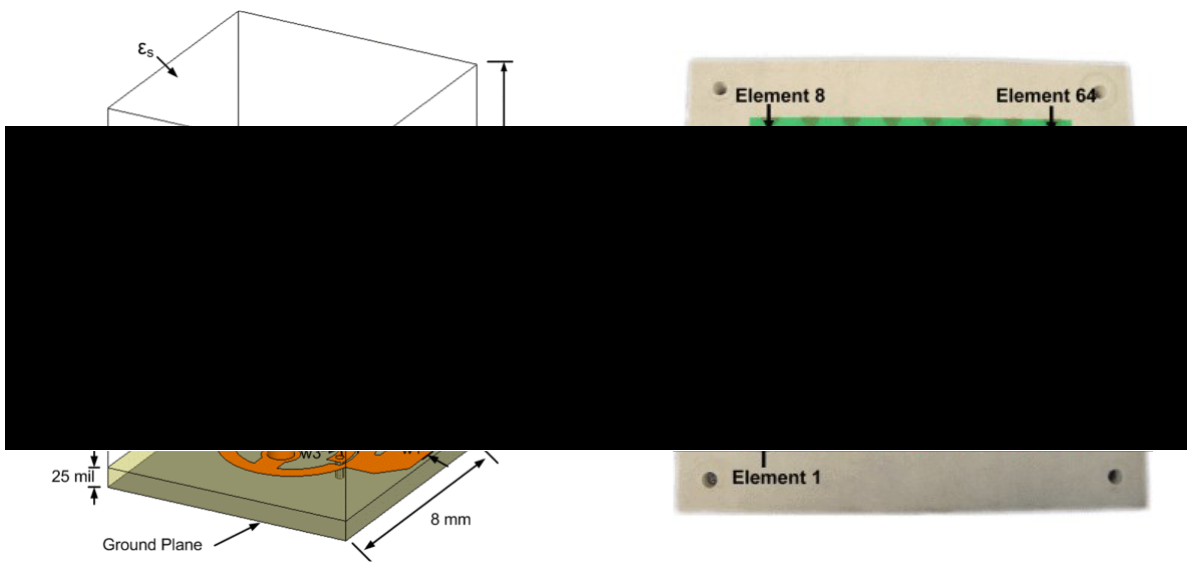


Figure 13. Geometry of the unit cell presented in [29].

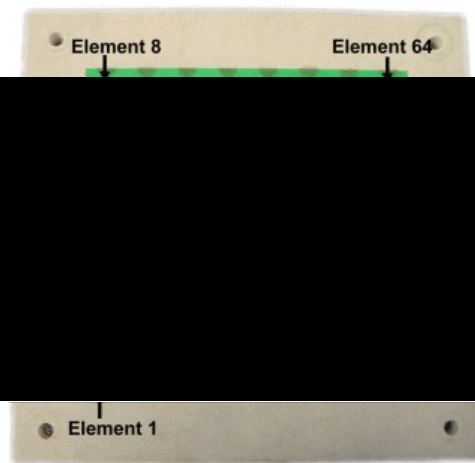


Figure 14. Fabricated phased array as presented in [29].

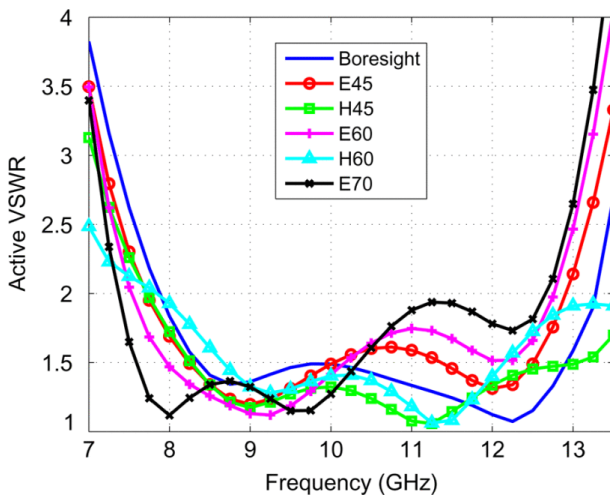


Figure 15. Active VSWR of the antenna array at various steering angles in the E and H-plane as presented in [29].

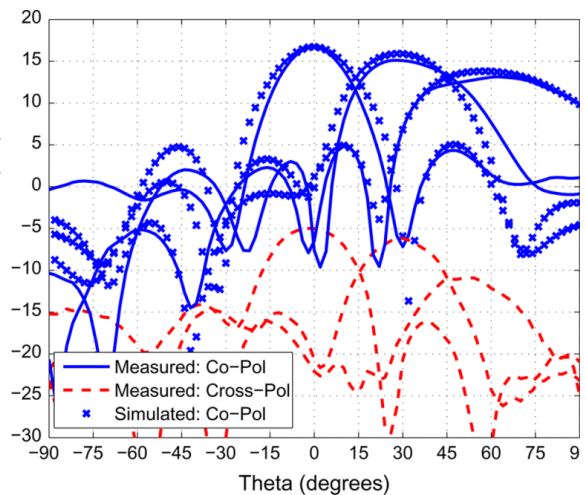


Figure 16. Measured and simulated co and cross polar performance of the antenna array presented in [29].

Other systems and structures have been developed [29] [30] [31] that provide functionality such as wideband coverage and wide beam steering, albeit with moderately high complex feeding networks. They deliver many of the antenna functionalities that are required of the BGAN communication. However, none of them can deliver all of the required BGAN functions simultaneously at a low cost, especially pertaining to producing CP beam steering at low elevation angles. A comparison of these designs with the original work presented in this chapter is displayed in Table 1 in Section 3.4.

In [29], non-symmetrical, closely coupled dipole antennas are utilised to enable a wide bandwidth even when placed over a ground plane. This coupling method, as shown in Figure 13, allows for control of the element capacitance to counteract the inductance between the element and the ground plane. As a result, a bandwidth of 43% (Figure 15) can be achieved. Beam steering performance is displayed in Figure 16 and shows good steering to $\theta = \pm 60^\circ$. However, this array only provides circular polarisation and is therefore not suitable for BGAN communication. Further, an antenna height of 0.17λ (not including the ground plane) is required as well as a full planar antenna array. As a result of this size, it would be difficult to implement and integrate at L-Band frequencies.

In [30] a dipole microstrip antenna is combined with an Artificial Magnetic Conductor (AMC) substrate layer enables wide beam scanning angles electronically. The prototype of this design is shown in Figure 17. The dipole elements demonstrate 24% bandwidth with a peak in the reflection coefficient above -10 dB at around 6.2 GHz as displayed in Figure 18. This bandwidth is impressive given the antenna height ($< 0.1\lambda$) and implementation of a metasurface in the substrate. Even more impressive is the beam steering capability of this array. Figure 19 demonstrates both beam steering with phase shifting only and with both amplitude and phase control. By changing both the amplitude and phase of the excitation signal in each array element, methods such as tapering or (as in this case) time-reversal synthesis can be

utilised to reduce sidelobe levels in the array pattern as demonstrated here. As many works utilise only phase shifting when verifying the performance of an array, the plot of phase only steering is more useful for direct comparisons. In this configuration, beam steering to $\theta = \pm 90^\circ$ has been demonstrated while maintaining gain variation of less than 3 dB, and a grating lobe lower than 5.1 dB below the main lobe. While array steering to $\theta = \pm 70^\circ$ has not been explicitly shown, given the -10 dB sidelobe level demonstrated at $\theta = 60^\circ$, it is expected that the side lobe level at $\theta = \pm 70^\circ$ better than -5.1 dB.

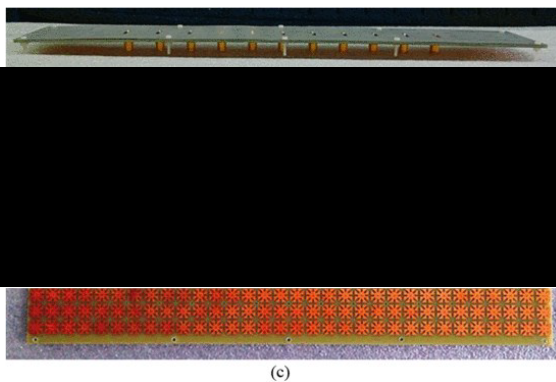


Figure 17. A linear 1x11 antenna array presented in [30] (a) side view, (b) top view, and (c) substrate meta-surface

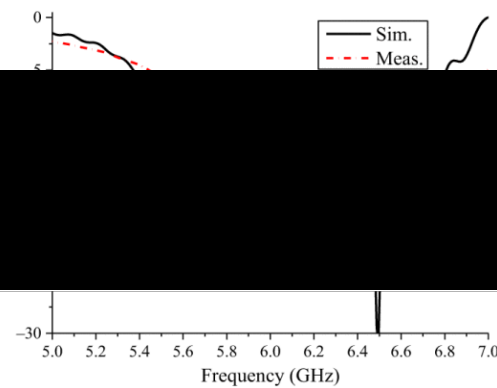


Figure 18. Simulated and measured reflection coefficient of the antenna presented in [30].

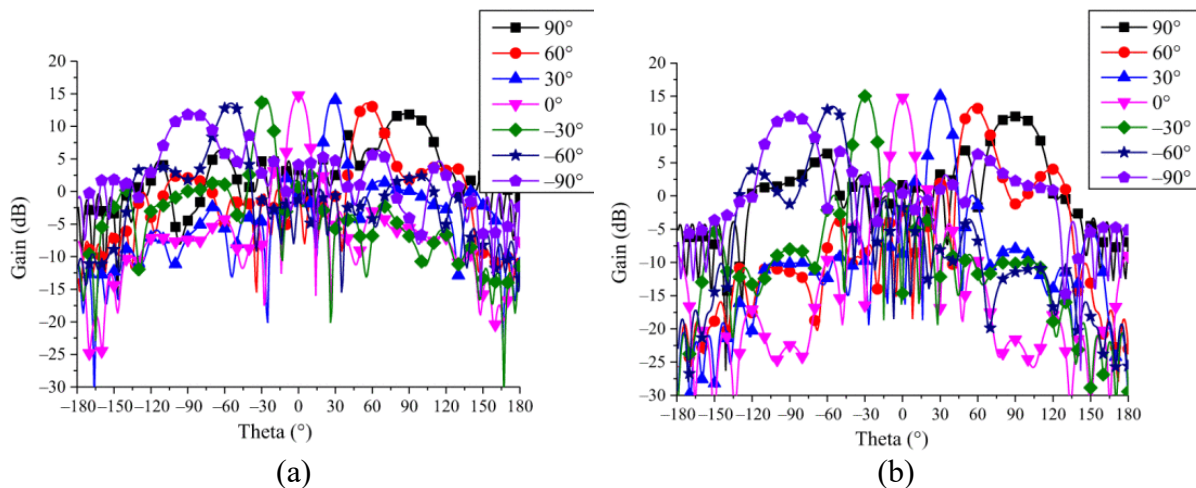


Figure 19. Beam steering capabilities of the antenna array presented in [30]. This displays the H-plane pattern of the antenna array when steered using (a) phase control only and (b) amplitude and phase control.

This result presented in [30] clearly demonstrates a capable system with wide beam steering capability. However, there are some significant limitations of this systems that are not addressed in this work. Firstly, this system is only shown in a linear array and hence no azimuth steering is possible. However, even if this antenna element design were placed in a rectangular 8×8 array and maintained the same performance at all azimuth angles, the cost and complexity of the feeding network would be very high. Indeed, with an 8×8 array 64 phase shifters and 64 amplifiers would be required.

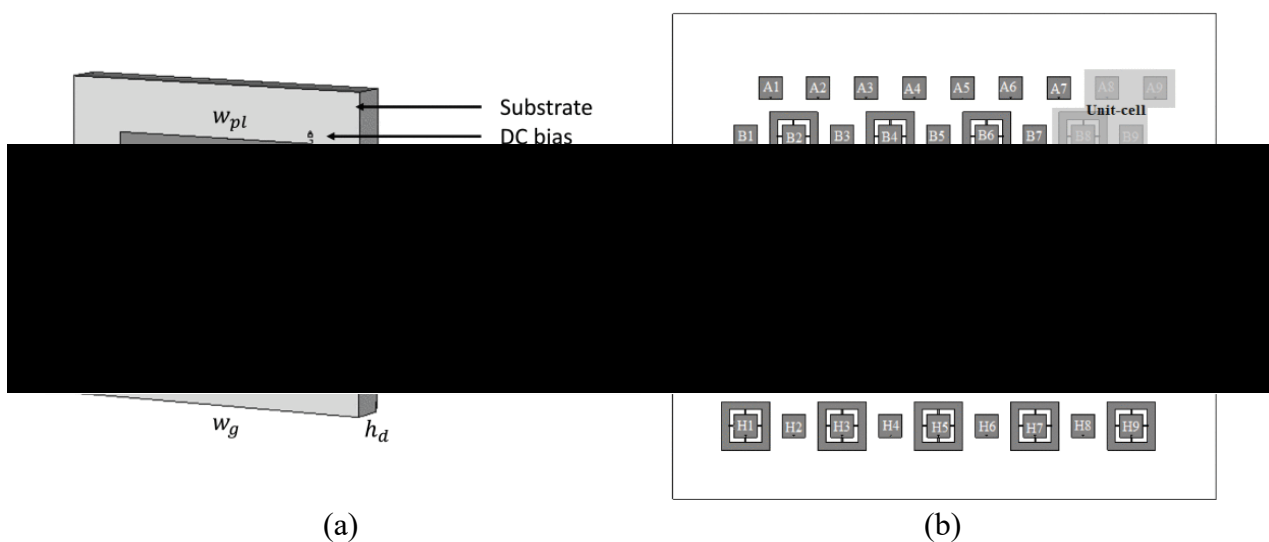


Figure 20. A multiband, wideband phased array design, presented in [31] showing (a) the antenna element geometry and components and (b) the antenna array geometry.

Both the antenna arrays in [29] and [30] demonstrate the use of static antenna elements in order to enable wide-angle beamforming over a wide bandwidth. However, there are some benefits to using active antennas (unit element antennas that can alter their characteristics as needed) to improve the overall performance of the array.

An active antenna design demonstrated in [31] utilises RF switches on the surface of the antenna patch to provide variable bandwidth to suit requirements. This design is shown in Figure 20 where an inner patch is connected to an outer ring patch by four surface mounted RF switches.

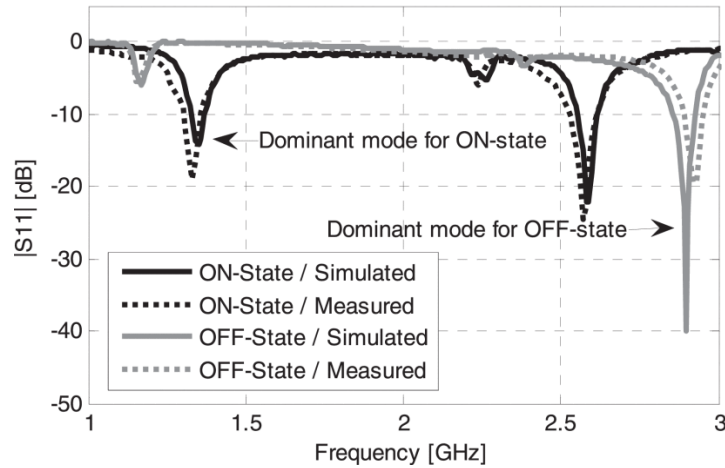


Figure 21. Reflection coefficient of the antenna element presented in [31]. By changing the state of the RF switches, shown in Figure 20 (a), multiple bandwidths can be targeted.

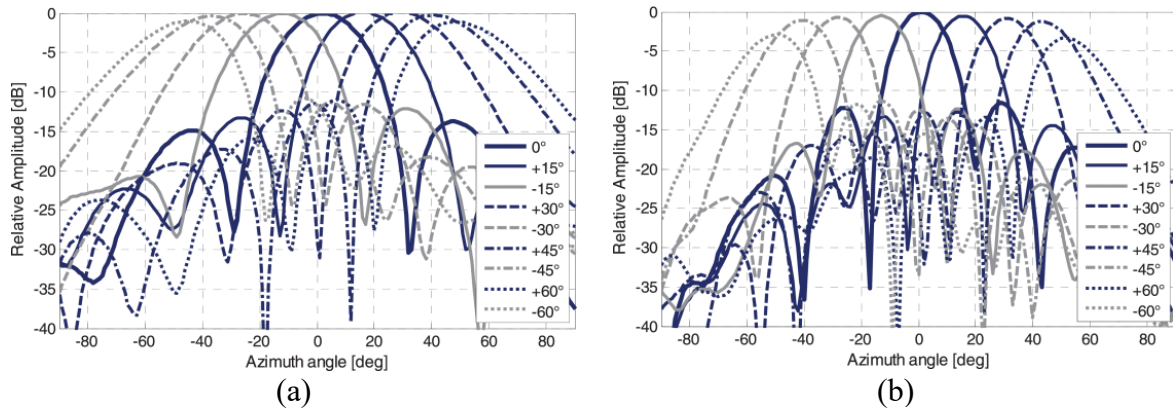


Figure 22. The beamforming performance of the antenna array presented in [31] at (a) 1.35 GHz and (b) 2.95 GHz.

Figure 21 demonstrates the reflection coefficient of the antenna element for both the on-state and off-state. The on-state results show a resonance at 1.33 GHz and the off-state returns a resonant at 2.95 GHz. While other resonances are present in the on-state, these are of a non-dominant mode.

Figure 22 presents the beamforming capability of the antenna array presented in Figure 20 (b). Here, the antenna array demonstrates beamforming down to $\theta = \pm 50^\circ$ from the boresight at both target frequency bands. At both frequency bands, the grating lobes remain 10 dB below the main lobe at all angles and the reduction in gain over steering angles remains below 3 dB. As the radiation pattern is normalised, the difference in directivity cannot be discerned. However, a significant narrowing of the beamwidth at 2.95GHz indicates a higher directivity at this frequency.

The use of RF switching in [31] has allowed for an adaptive bandwidth for antenna types that typically exhibit narrow band characteristics. However, when an already wideband antenna type is utilised, other key performance factors can be improved, or the cost of the feeding network can be reduced. In [32] such a system has been developed.

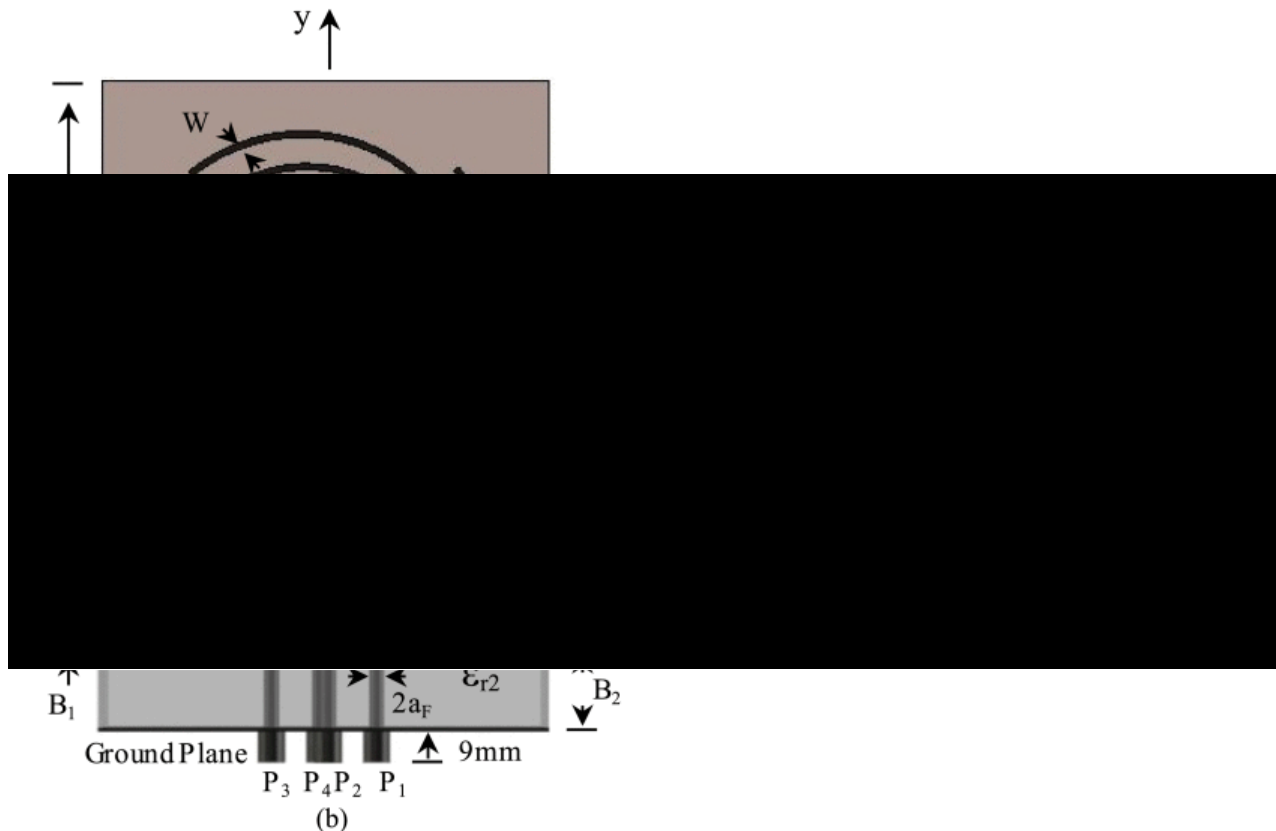


Figure 23. The 4-arm curl antenna design utilised in [32] showing port assignments, P1 to P4: (a) top view, (b) side view.

Figure 23 displays the design of a 4-arm curl antenna developed in [32]. In this antenna element, four curls are placed in 90° rotation from one another. These curl antennas radiate via a traveling wave mechanism whereby the wavefront travels along the length of the curl. As the frequency of the excitation signal changes, the active region of the curl also varies such that the curl can provide effective impedance matching across a wide bandwidth. As a result of this radiation method, a phase shift will occur across the length of the curl. In [32], this phase shift has been used to produce a tilted beam within the unit element. When placed in the 4-arm configuration, [32] proposes a switched beam technique where azimuth beam steering can be achieved from a signal switchable antenna element.

This method is limited in application in a number of ways, however. Firstly, the height required to produce such a sufficiently tilted beam is $1.8\lambda_c$, resulting in a large and heavy antenna at the target frequency. Secondly, as with many switch beam systems, the beam steering functionality is limited to four radiation directions, resulting in poor coverage in other azimuth directions and at low elevation angles.

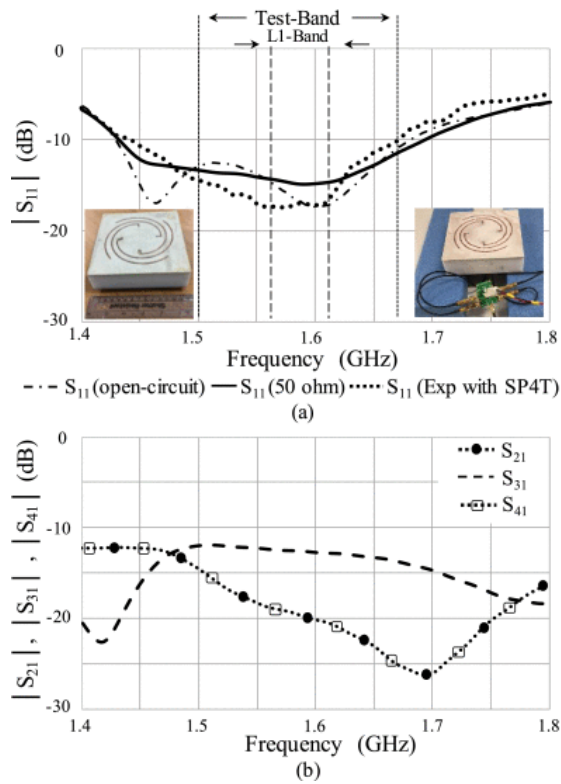


Figure 24. The s -parameters of the antenna element presented in [32]: (a) reflection coefficient, (b) isolation.

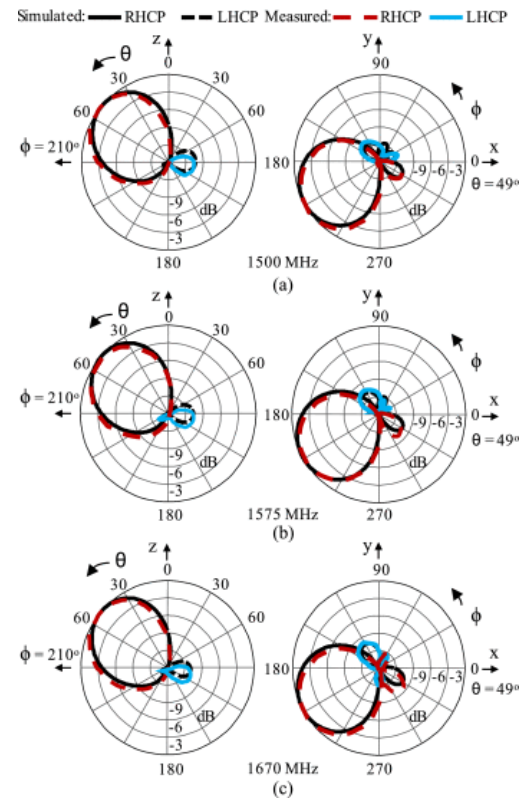


Figure 25. The tilted beam provided by the 4-arm curl in [32] at (a) 1500 MHz, (b) 1575 MHz and (c) 1670 MHz

As a solution to the challenges faced by vehicular GEO communication, a 1×3 linear array consisting of Quad-Arm Curl antennas with a High Impedance Surface (referred to as 'QACH') that is capable of providing wideband coverage and high gain beam steering covering elevation angles of $20^\circ < \theta < 70^\circ$ has been developed. This design uses only a fraction of the components of a typical square phased array. The ability for a linear array to provide complete azimuth steering is one of the key innovations of this work.

The proposed quad-arm curl antenna unit element can cover a wide operating bandwidth and hence allows shared aperture functionality. A High Impedance Surface (HIS) layer has been inserted into the quad-arm curl antenna element to provide a 54% reduction in height from previous designs [32] while also optimizing the antenna performance. The High Impedance Surface reduced the height required for the element to radiate by altering the phase distribution within the substrate.

This chapter also proposes a hybrid feeding network to excite the array. The entire feeding system requires only 4 phase shifters, 3 HPAs, 3 LNAs, 3 duplexers and 3 switches for both the Rx and Tx bands. This underpins a major reduction in the number of components required in comparison with feeding networks of typical planar arrays [33]. In practical terms, this represents a cost saving of over 75 %, providing opportunity for mass commercialization of low-cost terminals. In this regard, a prime example of the applications of this work is IOT for ambulances.

3.2 Quad-Arm Curl Antenna with HIS (QACH)

3.2.1 Element Design

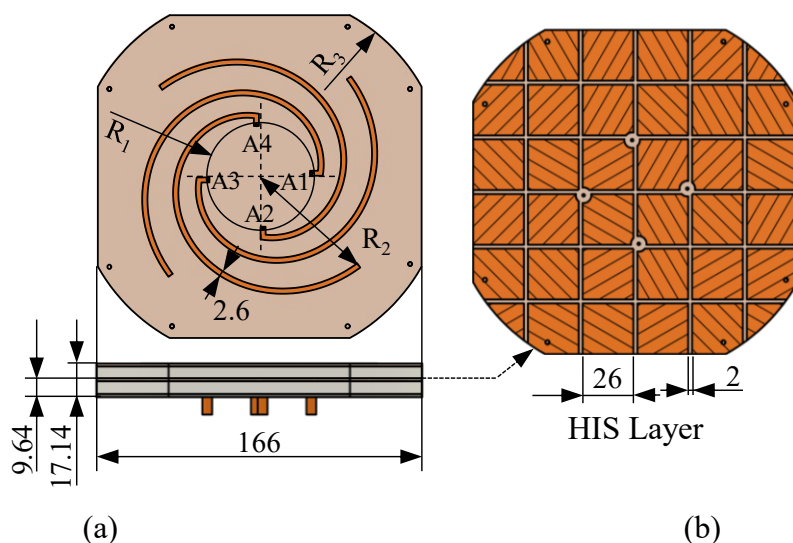


Figure 26. QACH element: (a) Antenna geometry top and side view, (b) HIS configuration. All units are in mm.

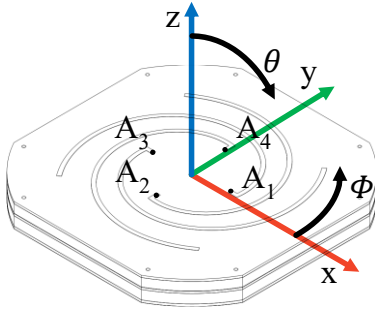


Figure 27. Isometric view of the antenna design (with ports and coordinates).



Figure 28. Fabricated QACH element prototype

The Quad-Arm Curl antenna with HIS (QACH) is constructed of five layers (net height = 17.14 mm), as displayed in Figure 26 (a). The antenna element has a width of 166 mm and bevelled corners of $R_3 = 95$ mm to allow for rotation in the array as presented in Section IV. The curl strip has an inner radius of $R_1 = 26.59$ mm, an outer radius of $R_2 = 68.28$ mm and a strip width of 2.6 mm. On the top layer, the curl antenna microstrips are printed on 1.5 mm thick Rogers RO4035B substrate ($\epsilon_r = 3.48$ and $\delta = 0.0037$). Below this is a low-cost 6 mm thick layer of Delrin plastic ($\epsilon_r = 2.6$ at 1.597 GHz and $\delta = 0.005$). Delrin plastic has a far lower cost than an equivalent thickness of Rogers RO4035B or FR-4, hence it is used here for constructing the majority of the antenna height. The central layer is a planar HIS as shown in Figure 26 (b) which is also printed on Rogers RO4035B of 1.5 mm in thickness. Again, Delrin layer with a height 6.5 mm is used as a thick substrate below this. Finally, a ground layer made from single sided copper plated FR-4 ($\epsilon_r = 4.8$ at 1.597 GHz and $\delta = 0.025$) of thickness 1.6 mm is placed at the bottom of the structure. Copper plated FR-4 is used as a ground layer due to its low cost and weight compared to a standalone copper sheet. This five-layer stratified antenna design allows for a simple, efficient and cost-effective fabrication. The QACH is fed from the bottom using four SMA (SubMiniature version A) connectors (A1-A4) with a feeding pin of radius 1.3 mm.

Figure 27 displays the isometric view of the antenna design and the coordinate system throughout this chapter and Figure 28 presents the fabricated antenna prototype.

Figure 26 (a) shows the QACH geometry where an HIS [34], [35], [36], [37] [38] metamaterial layer is inserted within the substrate layer. An HIS is a metamaterial structure that consists of a series of periodic patches above a ground plane. These are often, but not always, connected to the ground plane via pins or plated through-holes. This structure is electrically equivalent a corrugated ground plane in function and creates an open circuit within the structure, thus producing a region of high impedance within its vicinity. By placing it within the substrate of an antenna, this structure introduces its own phase and therefor alters the phase distribution within the structure such that the antenna can be far closer to the ground plane while still radiating efficiently. This allows for the antenna height to be reduced from 37.5 mm [32] to 17.2 mm ($\lambda_{1.597}/10.9$). Figure 29 shows the HIS unit model where its height from the ground plane is defined as x . Using established theory, the initial HIS unit model was optimized such that the zero-reflection phase point to occur at 1.597 GHz and covers the required bandwidth for a reflection phase of $\pm 90^\circ$. This was achieved where $x = 5.82$ mm (Figure 29 (b)). However, when placed in the QACH element it was found that the antenna reflection coefficient bandwidth was not meeting the necessary requirements. Using an EM simulator optimizer, the height of HIS was varied to achieve the desired impedance bandwidth. The required steady state was accomplished where $x = 9.66$ mm.

Typically, the zero-reflection phase point is calculated normal to the surface and not at an oblique angle. However, the QACH has a tilted beam not normal to the HIS surface leading to the final optimal value of x which was higher in comparison with the initial theoretical value.

Figure 30 shows the surface currents of the antenna element. It can be seen that the primary current component is confined to the excited curl arm. However, lower amplitude current is also present on the other three passive curls and on the HIS metal patches. These all

contribute to radiation for producing a circularly polarized tilted beam [32]. In this configuration, the antenna produces a tilted beam with a maximum gain of 8 dBic at $\theta_{\max} = 40^\circ$.

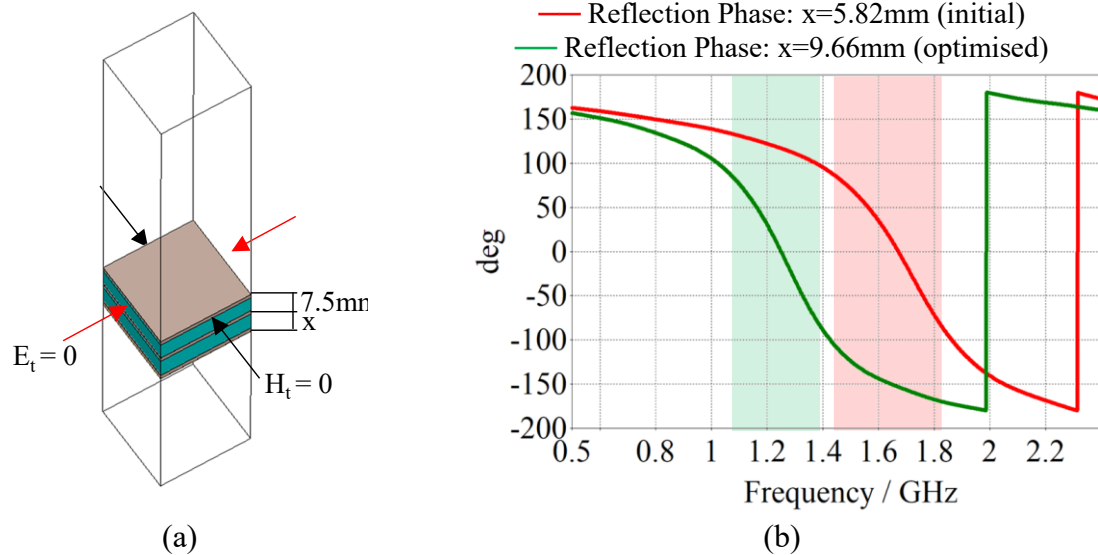


Figure 29. (a) Initial HIS unit model. (b) The resultant reflection phase diagram. The initial theoretical design where $x = 5.82$ mm showing good phase matching for radiation normal to the surface. Optimization within QACH element done to provide better performance for the tilted beam application, resulting in x becoming 9.66 mm.

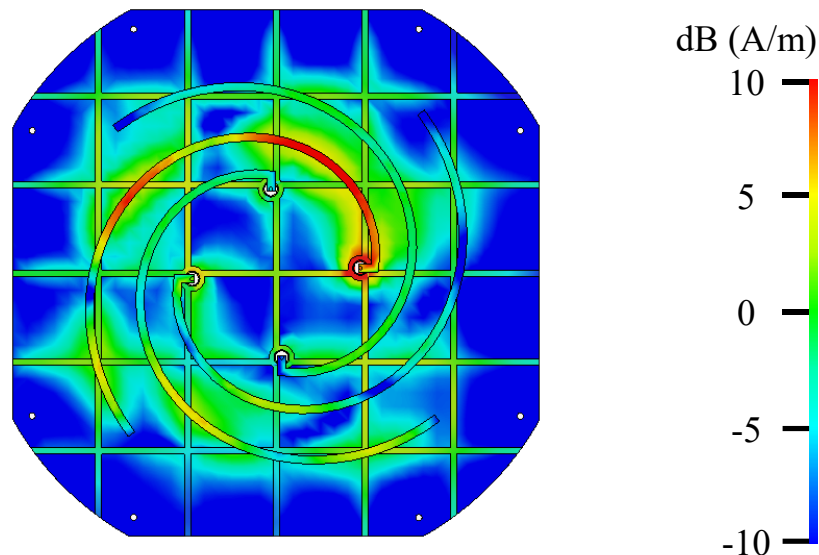


Figure 30. The average surface currents over the QACH antenna element at the centre frequency of 1.597 GHz.

Each element consists of four curl arms [39], each fed from a port at the beginning of the curl (Figure 27). Excitation of each port produces a circularly polarized tilted beam covering a quadrant [34]. The antenna provides a tilted beam of right-hand circular polarization over a wide bandwidth, as explained in [32] and [39].

3.2.2 Element's Results

The reflection coefficient measurements are taken with a Rohde & Schwarz ZNA40 four port VNA [40]. Each port is measured individually by connecting a single port to the VNA and leaving the remaining ports open. The antenna is able to operate both when the remaining ports are open-circuited or 50Ω terminated. Open-circuit conditions have been chosen in the final design to provide higher efficiency. This is effective as, choosing an open circuit solution, the remaining curl antennas will still receive the signal but this power will not be absorbed by the impedance load. When a single port is excited and the remaining ports are open-circuited, the non-excited curl arms act as parasitic elements and so are not included in the scattering matrix, hence port isolation is only applicable when the element is placed in an array in Section 3.3. In final product integration, open-circuit Single Pole 4 Throw (SP4T) switches will be used to select a single curl arm per element. The measured and simulated reflection coefficients in Figure 31 show that the measured reflection coefficient is below -9 dB for all ports within the targeted band. Similar to many cellular communication devices [41] [42], a reflection coefficient better than -6 dB can be sufficient to provide the required performance. In here, by maintaining a reflection coefficient less than -9 dB and an antenna array gain greater than 6.6 dBic at all angles, we are able to meet the link budget requirements of Inmarsat Class 12 [18]. If necessary, the reflection coefficient could be further expanded by improved matching and bringing the second resonance at 1.74 GHz to a lower frequency. However, this may require a slightly greater antenna height. While there is a small shift in the

resonant frequency between measurement and simulation, the results are in good agreement, and both cover the required bandwidth.

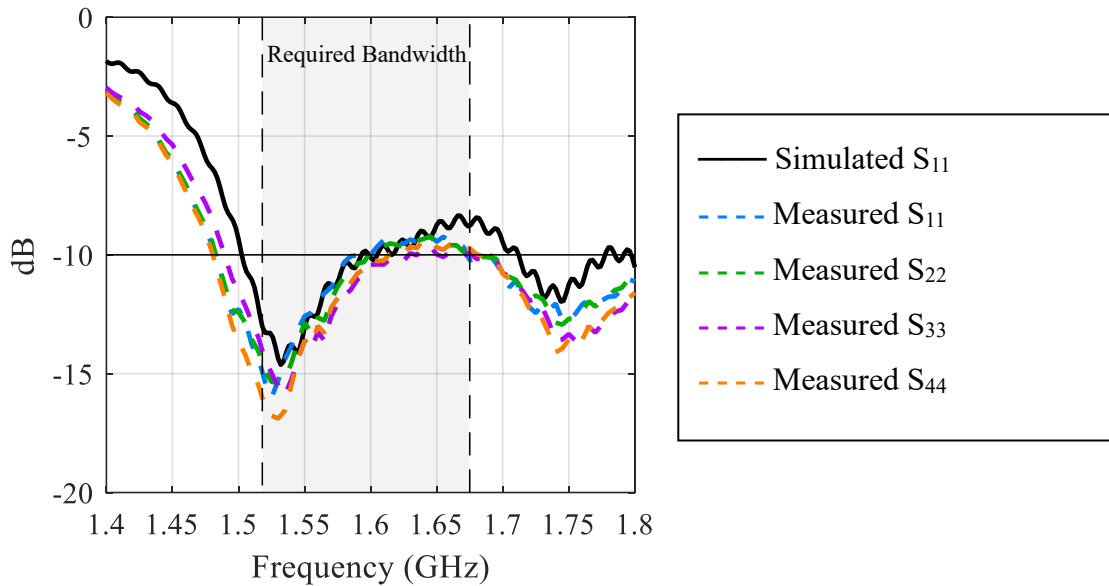


Figure 31. Simulated and measured S -parameters of QACH antenna element shown in Figure 26.

The element radiation patterns were measured with a SATIMO/MVG StarLab testing chamber [43] and are shown in Figure 32 together with those captured in simulations. The results confirm that the quad-arm curl antenna generates an RHCP tilted beam with an RHCP gain greater than 8 dBic. The tilt of the beam is maintained at $\theta = 40^\circ$ at all test frequencies. The axial ratio is maintained below 8 dB across the 3 dB beam width for all frequencies. This is suitable as the requirements for the target Inmarsat BGAN class 12 only necessitate an axial ratio below 8 dB for its ground terminal applications [18]. It is possible for a curl antenna and HIS to have a further improved axial ratio, however this would require increasing the height of the antenna substrate. Here we have optimized the antenna to reduce its height and in turn, its weight as far as possible while meeting Inmarsat BGAN Class 12 link requirements.

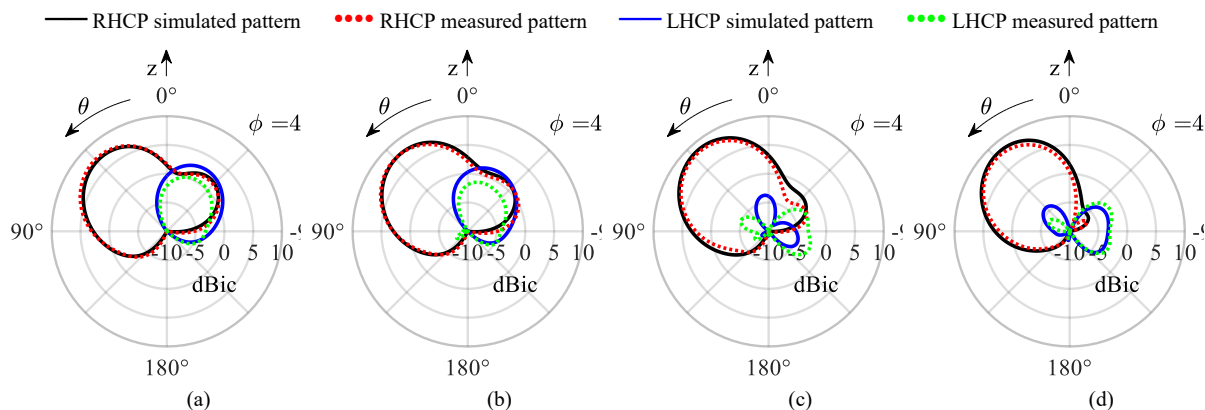


Figure 32. Simulated and measured RHCP and LHCP radiation patterns of QACH antenna element at (a) 1.518 GHz, (b) 1.559 GHz, (c) 1.627 GHz and (d) 1.675 GHz over the operating frequency band.

3.3 1×3 QACH Antenna Array

3.3.1 Array Design

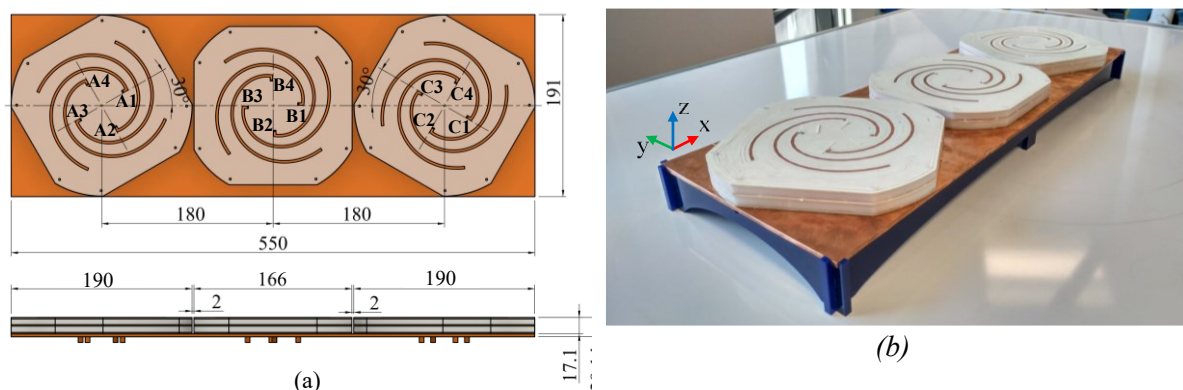


Figure 33. QACH array: (a) 1×3 linear array design (units in mm); (b) array prototype.

Previously, [44] has developed a C-band 2×2 quad-arm curl antenna array, albeit without the key size benefits of an HIS and the vital low-cost implementation presented here. An L-band 2×2 QACH array configuration would be physically sizable (332 × 332 mm) even with the application of an HIS. Therefore, in order to reduce size and cost, a 1×3 rotated linear array has been considered, as shown in Figure 33(a) and (b) where antenna elements are physically rotated along the directions of -30° , 0° and 30° . The rotation results in a total of 12 beams distributed evenly across the azimuth plane with 30° separation. By combining each

element beam with its two adjacent beams the directive gain increases and, with a phase shift applied across the array, precision beam steering can be achieved. Using this hybrid switched beam and phased array method (Figure 34) the array can uniformly cover the entire azimuth plane despite its linear topology. With this method, wide beam steering while only requiring 3 HPAs, 3 LNAs, 4 phase shifters and 3 switches has been achieved.

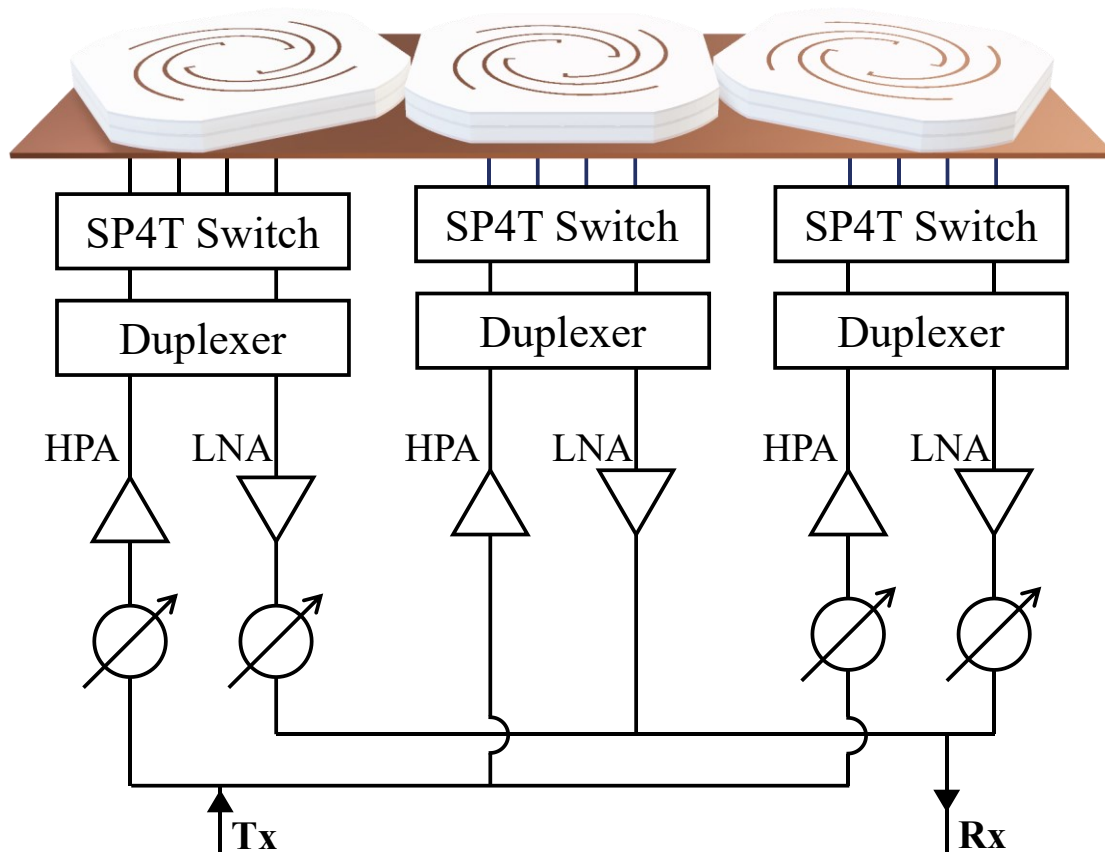


Figure 34. Diagram of the simple, low-cost feeding network for the 1x3 QACH array.

In operation, three adjacent ports (1 port from each element, e.g. A1, B1 and C1) are selected with Single Pole 4 Throw (SP4T) switches. Phase shifters placed before each switch are used for precise beam forming for the selected ports. An example of how we have achieved a combined array beam is shown in Figure 35. In this example, a beam is targeted along $\theta = 70^\circ$, $\phi = 0^\circ$. In order to target these coordinates, ports A1, B1 and C1 are excited with equal amplitudes and phases of -20° , 0° and 50° respectively.

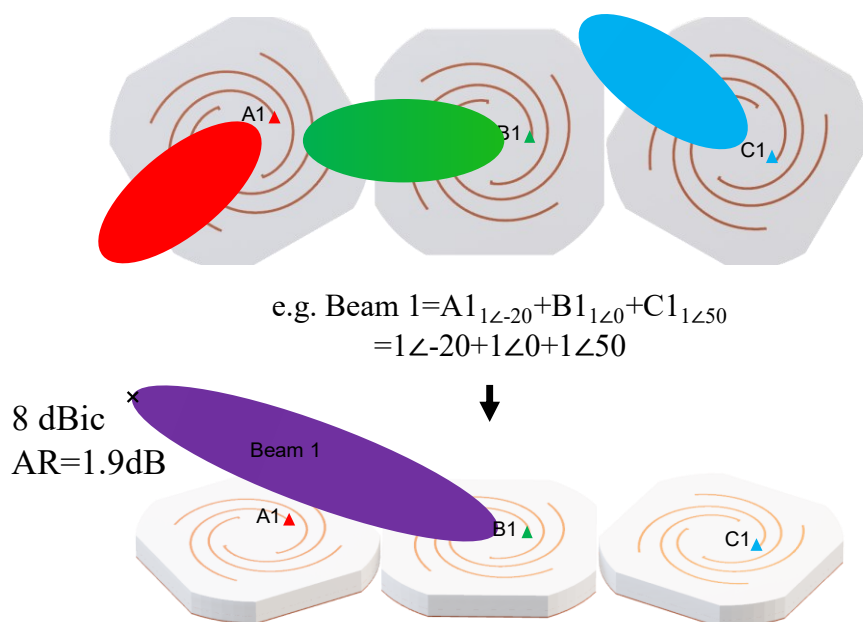


Figure 35. Example diagram of the hybrid beam-steering method.

3.3.2 Array Performance Verification

The antenna array has been measured in a NSI-MI Technologies and Frequency's near-field anechoic test chamber. A bespoke feeding network, Figure 36, controls both the phase shifting and port switching. This RF board uses commercially available components (e.g. MACOM MAPS-010163, Mini-Circuits CMA-545G1+, Analogue Devices ADRF5047) and follows a broadly similar scheme to that shown in Figure 34.

Figure 37 (a) and (b) show the azimuth scanning performance of the proposed array at elevation angles of 20° , 45° and 70° . The average gain at $\theta = 70^\circ$ is 7.96 dBic and ranges from 6.63 dBic to 12.78 dBic for the three elevation angles shown. Some reduction in gain can be seen around $\phi = 0^\circ$ and $\phi = 180^\circ$. This is due to the linear array topologies and asymmetrical placement of antenna elements. The measured results at 70° elevation are close to the simulated results for both the Rx and Tx bands.

The axial ratio of the respective beams is shown in Figure 37 (c) and (d). The axial ratio remains below the required 8 dB for the majority of the targeted angles. The measured axial

ratio for the beams at $\theta = 70^\circ$ matches the simulated results well, showing very little variation for most points.

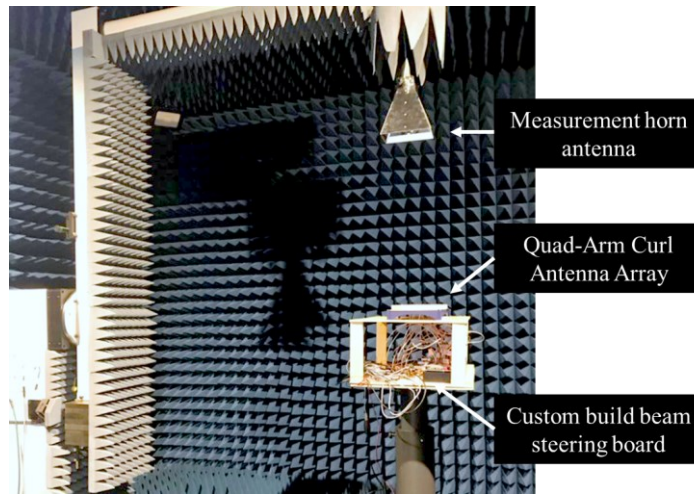


Figure 36. QACH array performance test setup.

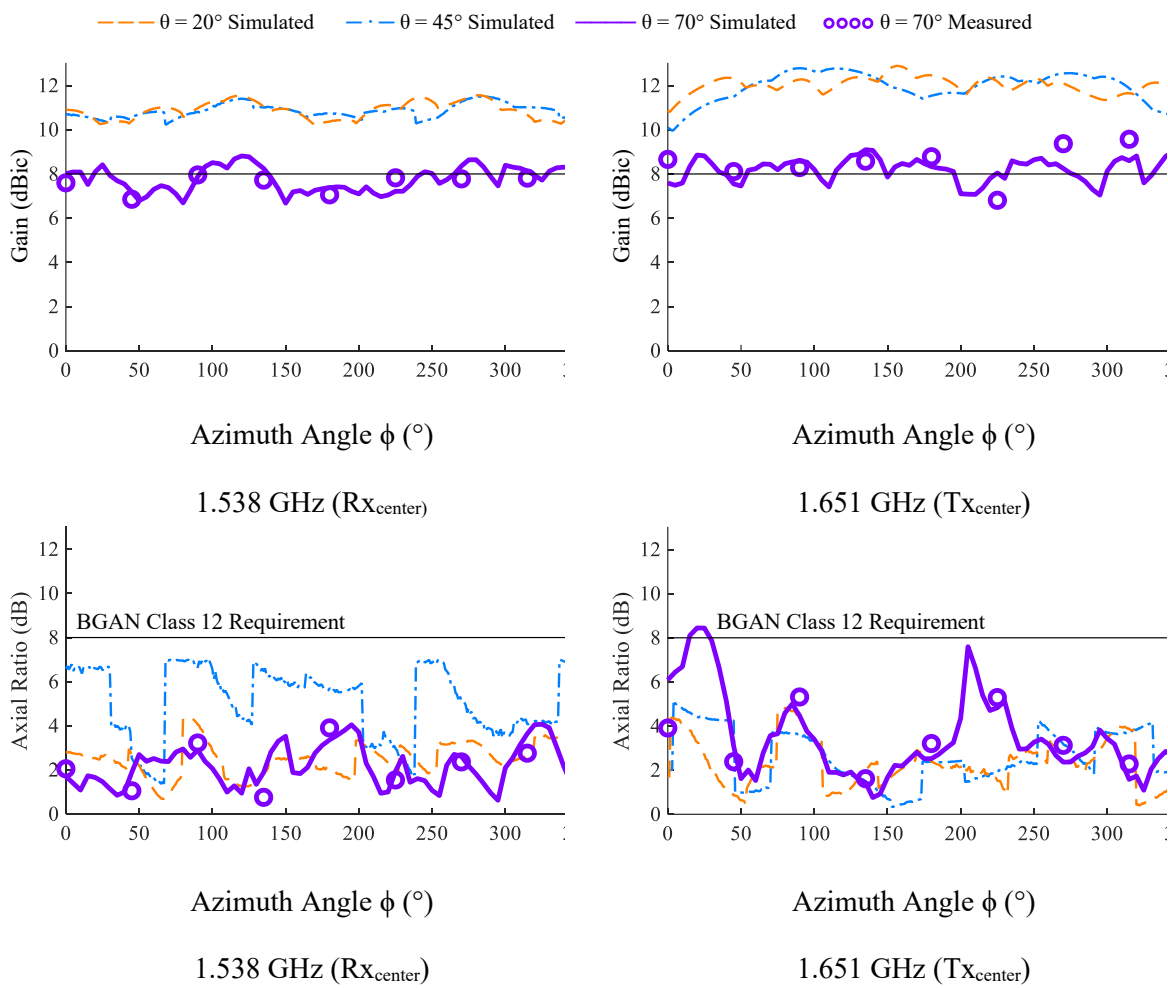


Figure 37. Beam steering performance (predicted & measured) of the 1x3 QACH array: (a) & (b) gain and (c) & (d) axial ratio at 1.538 GHz & 1.651 GHz.

Figure 38 shows the measured and simulated RHCP and LHCP radiations patterns of the array steering when a beam targeting in the direction of $(\theta, \phi) = (70^\circ, 45^\circ)$ and $(45^\circ, 90^\circ)$ for receive and transmit frequency bands. As the receive band does not causes interference, the back lobes are non-concerning for the satellite link. In transmit mode, the RHCP back lobe obtained was found to be better than -9 dB in the majority of cases. The measured radiation patterns show good agreement with the simulated data.

The s-parameters of the array have been measured with an R&S ZVA40 VNA. In operation, as explained previously, only three ports in the array (one port in each element) are in use at any one time while the other nine ports are left open-circuited. Therefore, when measuring the reflection coefficient and isolation between ports, only three ports are used per measurement.

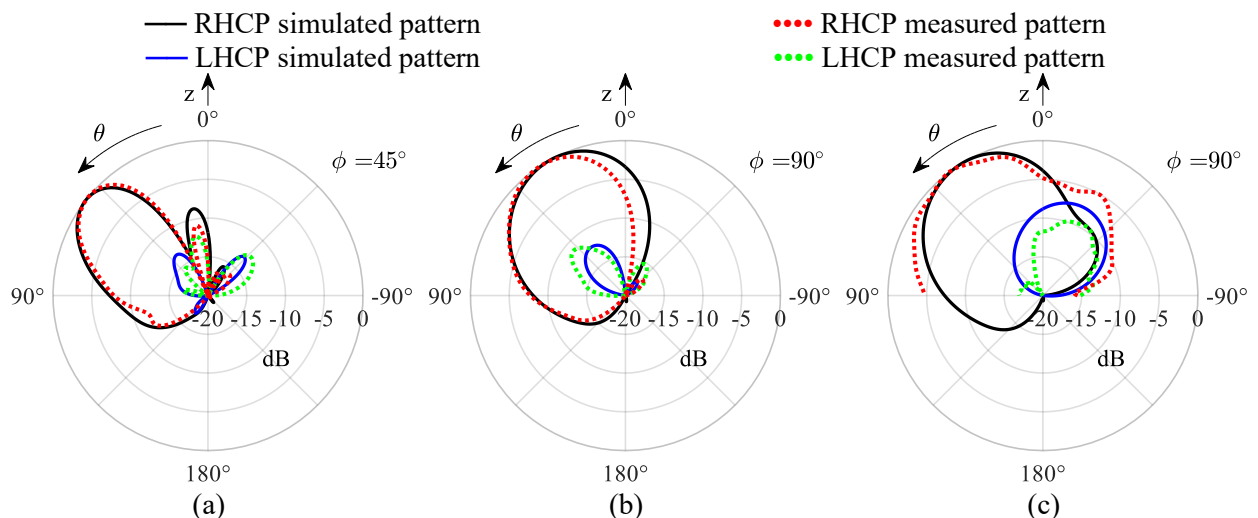


Figure 38. Simulated and measured RHCP and LHCP polar patterns showing the array steering performance for Tx and Rx beam maximum. (a) Tx beam targeting $(\theta, \phi) = (70^\circ, 45^\circ)$; (b) Tx beam targeting $(\theta, \phi) = (45^\circ, 90^\circ)$ & (c) Rx beam targeting $(\theta, \phi) = (45^\circ, 90^\circ)$.

Figure 39 shows the S-parameters measured for all 12 ports (e.g SA1, A1 - SC4, C4) with unexcited ports left open circuited. The measured reflection coefficients remain below -9 dB for the required frequency band, as anticipated by the simulation. The isolation between ports remains below -20 dB for all ports. The radiation efficiency remains above 98 % for both single port and array configurations. The total efficiency of the array remains above 90 %.

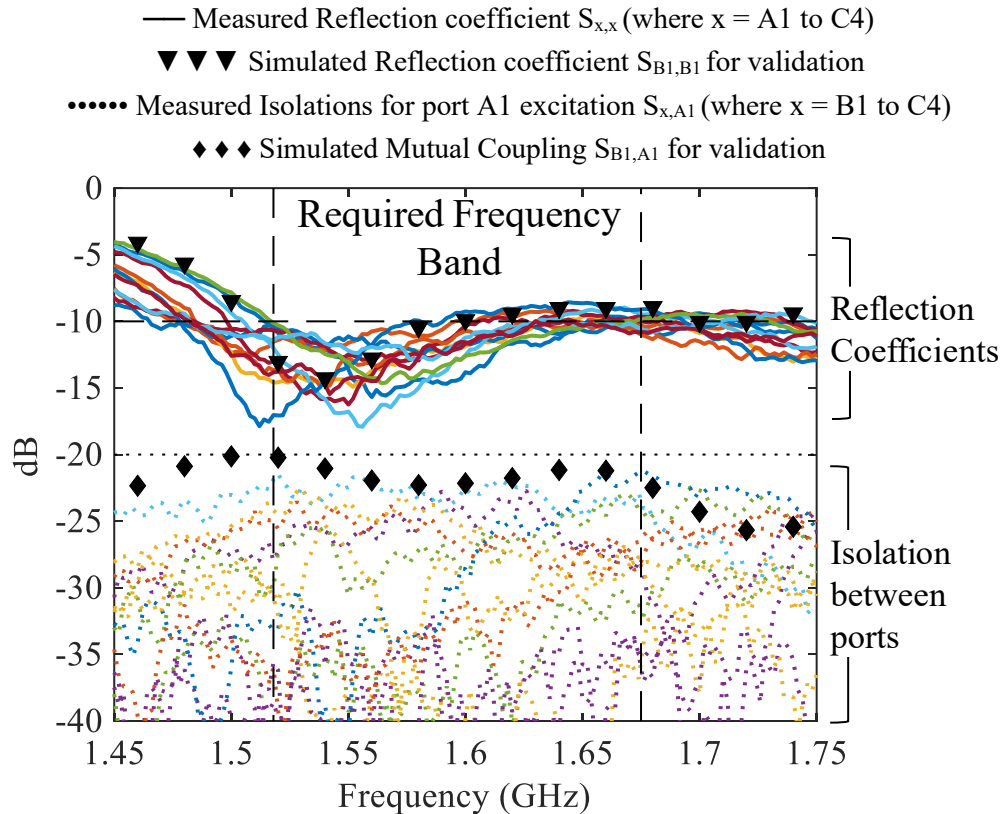


Figure 39. Array reflection coefficients and isolation between the 12 ports.

3.4 Discussion

Table 1. A comparison between this work and existing works.

	This work	[29]	[30]	[31]
Array Type	Linear	Planer	Linear	Planer
Elevation Steering Angles	+/-70	+/-60°	+/-90	+/-60°
Bandwidth	10%	43%	5%	3.5%
Full Azimuth Coverage	Yes	Yes	No	Yes
Thickness	0.09 λ	0.17 λ	0.04 λ	0.04 λ
RF Network Cost	Low	High	Medium	High
Circular Polarization	Yes	No	No	No

A 1×3 quad-curl antenna with an HIS substrate in a linear array configuration has been presented for L-band satellite communications. The QACH antenna unit element provides an operating bandwidth of greater than 10 % (1.518 - 1.675 GHz), allowing for shared-aperture functionality. The height of the antenna has been reduced by the application of an HIS

metamaterial layer. As a result, it is only 17.2 mm in height ($0.1\lambda_{1.597}$). The proposed array can provide RHCP beam steering within elevation $20^\circ < \theta < 70^\circ$ and full azimuth coverage, while still maintaining an average gain of 7.96 dBic at $\theta = 70^\circ$. In addition, as the proposed antenna array only consists of three elements, the feeding network requires only 4 phase shifters, 3 duplexers, 3 switches, 3 HPAs, and 3 LNAs. In comparison with a typical 4×4 patch array, this small number of components significantly reduces the number of required components by more than five times. This will greatly reduce the cost of such a system, particularly in regards to expensive components such as the power amplifiers and phase shifters, but will also reduce cost in regard to design and fabrication of power and control circuits within the board. Further, lower cost controllers can be used given the limited number of interfaces required.

A complete comparison between the proposed antenna array design and a number of similar works [12-14] is shown in Table 1. The work presented in this chapter is shown to provide an advantageous combination of functionality that uniquely makes it ideal for low-cost GEO satellite applications. Because of the array's low cost, small size, and high gain at angles near to the horizon, it delivers an innovative solution for on-the-move satellite IoT applications. Future systems with such a flat panel curl array will be able to provide mass deployable, uninterrupted internet access to market segments that would have previously found satellite communication impractical or unaffordable.

Chapter 4.

Ka-Band Split & Shared Aperture Antenna Arrays for LEO Satellite Communication

Chapter 3 presented a low-cost solution for GEO satellite communication for emergency vehicles. While GEO satellite networks provide absolute reliability and emergency certification today, much of the focus on future consumer satellite communication is now squarely on LEO constellations. While these constellations are still in their early stages, it promises high speed internet access (>100 Mbps) from any location in the globe. Unlike GEO communication, LEO constellations will use thousands of interconnected satellites close to the earth to deliver higher capacity and lower latency than previous technologies. Furthermore, advances in RF systems allow for low-cost utilisation of frequencies in the Ku to Ka spectrum region, allowing for the high data rates expected by the system.

The work presented in this chapter details the development of a split aperture antenna array where receive and transmit elements are placed in separate arrays and then a shared aperture antenna array where receive and transmit elements are interlaced in a single antenna array. As a result the antenna array provides high performance in a compact design that allows for easy fabrication.

This work was produced as part of the CASISS project in collaboration with a number of UK companies including Ensilica [45], Celestia UK [46] and Satellite Applications Catapult [47]. The goal of this project to develop a system for LEO communication that can be easily

integrated into a vehicle at low cost. A Ka band RFIC has been developed by Ensilica for this project that enables phase and amplitude control for both receive and transmit channels in a signal compact chip. The split aperture is designed for the first revision of the RFIC, however a second revision that greatly reduces the footprint of the chip has been developed that enables the shared aperture capability presented in section 4.6.

4.1 Existing Work

There are a number of companies currently competing in the LEO market including SpaceX Starlink, Amazon Kuiper and OneWeb. All of these companies are investing large sums of money to develop their own LEO constellations with the expectation of the sector becoming a vital part of future communications. Alongside these large players are smaller companies focused on developing cutting edge technology to enable the expansion and adoption of LEO networks.



Figure 40. Third Generation Starlink Terminal [48].

This section will investigate the current state of the art antenna array designs currently available or in development. Unfortunately, given that much of the latest developments in this

area are developed by industry, there are no complete papers detailing the exact working of such systems. However, as will be shown, a great deal can be discerned from the limited material that is available.

Of the large constellations in this space, only SpaceX has released a publicly available user terminal for accessing their network. Their system targets Ku-band frequencies of 10.7-12.75 GHz for receive and 14-14.5 GHz for transmit [49].

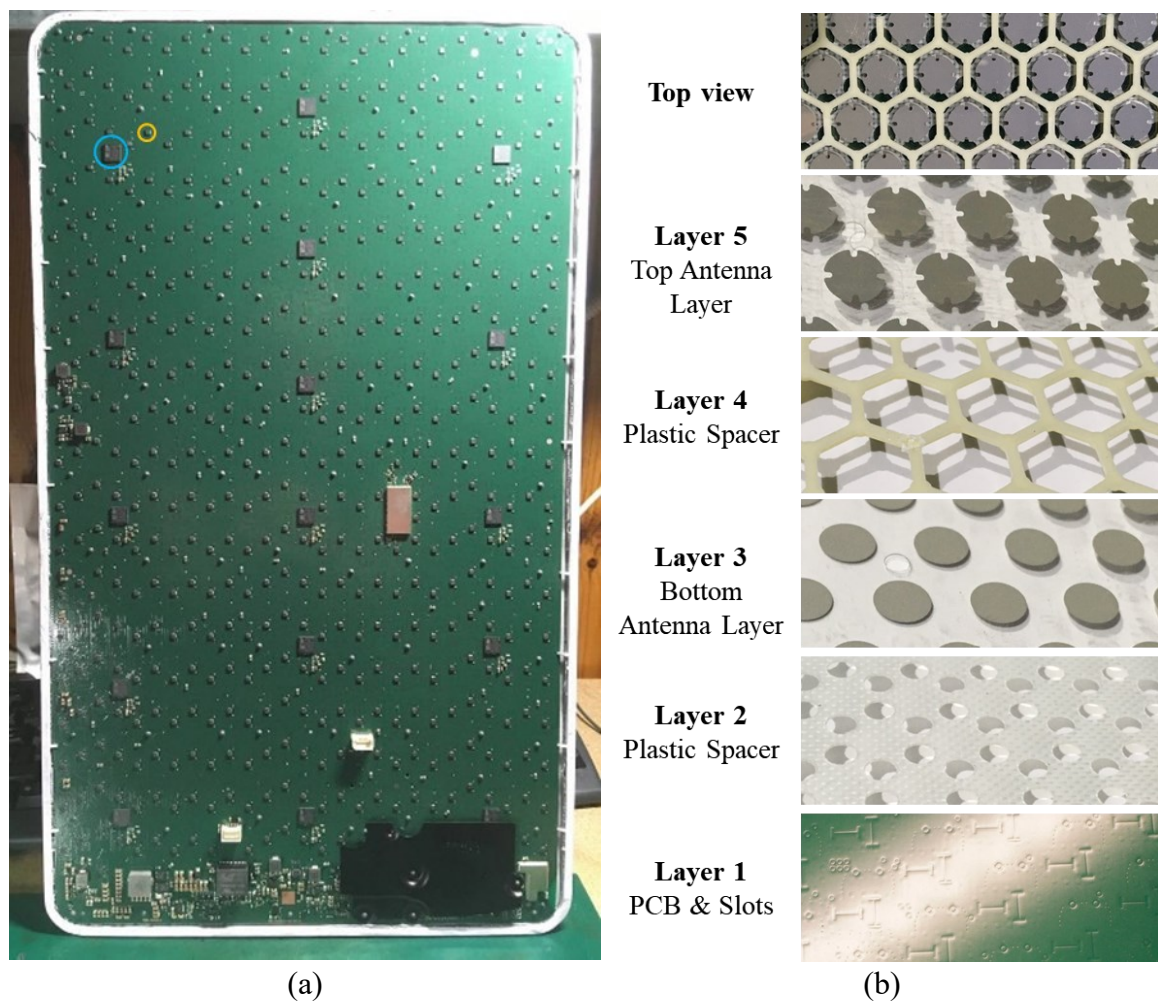


Figure 41. A teardown of a Starlink third generation phased array antenna showing (a) back view [50], (b) close up of slot feeding outline [51] and (c) a view of the antenna layers and hexagonal spacer [52].

This system uses a shared aperture hybrid beamforming antenna array. That is, the system mechanically steers the antenna array for broad beam pointing and then electronically steers the array beam for accurate targeting. The tripod and mechanically controlled phased

array panel are shown in Figure 40. The array panel itself is 303×513 mm in size. There is limited information on the exact performance details of this system due to the commercial nature of the work, however Figure 41 presents a dismantled Starlink antenna array from which some information can be intuited. At the back of the phased array antenna (Figure 41 (a)), a series of small chips can be seen covering the back of the PCB (an example is highlighted in orange). Each one of these small chips could potentially be RFIC that could feed the surrounding antennas while also providing phase and amplitude control. These small chips surround 16 larger chips across the board (an example is highlighted in blue). The larger chips could be used to distribute the RF signal to the smaller RFICs and may even be ADC/DACs that are fed the signal directly from the digital baseband.

The antennas clearly use a slot feeding method where a slot is made in the ground plane of the antenna, and the excitation microstrip is placed below the slot such that it resonates. The antenna patches are then placed above the slots such that they couple with the slot to resonate and radiate themselves. In this design, a PCB is only used up to the slotted ground layer. These slots can be clearly seen in Layer 1 in Figure 41 (b). A layer of plastic (Layer 2 in Figure 41 (b)) is then placed on top of the PCB to provide an air gap between the slots and the first antenna layer which are printed on a thin flexible plastic sheet (Layer 3 in Figure 41 (b)). These antennas are distributed in a triangular lattice. Upon the first array layer a thick hexagonal plastic layer is added, again, to provide an airgap (Layer 4 in Figure 41 (b)). Finally, the top antenna elements, also printed on a thin flexible plastic sheet, and placed directly above the antenna elements below (Layer 5 in Figure 41 (b)).

This system is clearly designed with a low cost in mind. Slot feeding mechanisms can often lead to inefficiencies and limited bandwidth performance but are far less complex than direct feeding would be at high frequencies. Unfortunately, this system appears to be limited in its electronic beam steering performance given the requirement for mechanical steering

alongside electronic steering. The mechanical steering does appear to aid in reducing the overall size of the array as, by enabling physical rotation of the array around the azimuth plane, there is less need for beam steering along with width of the array to provide full azimuth coverage. As a result, the array width has been reduced to 300mm compared to a length of 500mm. SpaceX has stated that, as of April 2021, each terminal costs around \$1300 to produce [53].

However, in spite of the benefits of mechanical steering for static ground terminals, the system is unsuitable for vehicular integration where pure electronic steering is required. It is, nevertheless, an impressive state of the art design in the field of antenna array design.

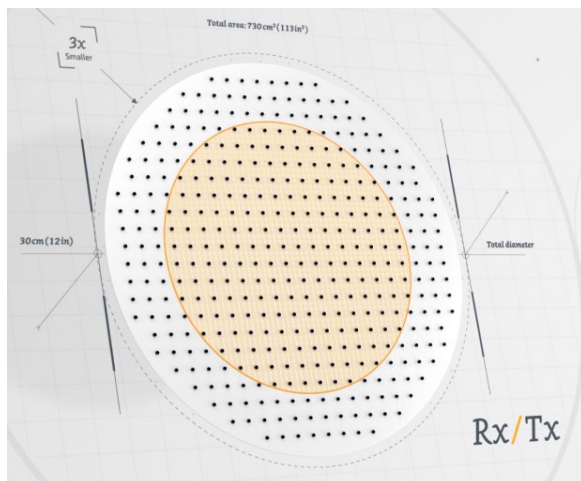


Figure 42. A stylised diagram of the shared aperture antenna array currently in development by Amazon project Kuiper [54].



Figure 43. A side view of the Amazon Kuiper terminal antenna [54].

Another large company developing LEO communications is Amazon and their Project Kuiper division. This project targets higher Ka-band frequencies (17.7-19.3 GHz at receive and 28.5 – 29.1 GHz at transmit [54]) than Starlink. There is unfortunately even less information available in regard to their ground terminal antenna other than a stylised diagram presented in Figure 42, and a side view of the antenna array displayed in Figure 43. This antenna array developed here combines the Rx and Tx into a single multilayer element and results in a 1:1 ratio of Rx and Tx feeding requirements. However, due to the ~ 10GHz difference in frequency

between Rx and Tx, there will therefore be a large variation in array directivity for each Rx and Tx subarray. This is likely the reason for the smaller Tx subarray area (shown in orange in Figure 42), as outer Tx elements were likely not needed to meet the directivity requirements. A second important difference visible in Figure 43 is the single PCB design used.

Unlike the Starlink antenna array, the feeding network and antenna elements appear to be manufactured in a single PCB board. This will add complexity to the PCB design, but may allow for higher efficiency and greater performance, as well as a lower overall profile. Finally, this design uses purely electronic steering, with seemingly no mechanical components suggesting greater beamforming performance over that developed by Starlink. This system only requires a single circular polarisation mode for Rx and Tx i.e. RHCP for receive and LHCP for transmit. Thus, there is no need for polarisation reconfigurability, and so this can significantly simplify the antenna array design. However, this choice does limit the spectral efficiency of the satellite constellation. Much of the difference in design choices between these two systems may be explained by the difference in frequencies between the Rx and Tx bands. The greater difference in wavelength used by the Starlink system Rx and Tx bands has allowed two Tx element to be interlaced per Rx elements. At the frequencies utilised by Amazon Kuiper, this would not be easily possible. The Kuiper project is still at the prototype stage and (at the time of writing) has yet to launch even a prototype satellite [55].

Aside from the large LEO constellation companies, there are a number of researchers and companies working to develop standalone K and Ka band antenna arrays for mobile LEO communication. One novel alternative topology is that developed by ALL.SPACE (formally Isotropic Systems) [56]. The design and methodology of the system is shown in Figure 44. This system utilizes an array of dielectric lenses that can steer the radiation beam such that, as an antenna below is moved away from the centre of the lens, the resultant beam will tilt away from the boresight direction (Figure 44 (b)). In the full system, an array of patches is placed

below each lens. These patches are not excited simultaneously, instead only a single patch is excited per lens (Figure 44 (c)). By switching between patches at different locations the beam can then be directed to a specific direction. In an array of these switch beam lenses, a phase shift can then be applied across the lenses for high accuracy steering. Even at Ka band frequencies, because of the limited phase shifting required, grating lobes will remain low despite the large distance between lenses used in the design. Overall, the technique used in this system allows for high performance in a low-cost system even at high frequencies. Unfortunately, the distance required between the lens and the antenna switching array below results in a very high-profile system. This is suitable for a unit placed on existing vehicles with suitable mounting support, but unworkable for widespread fully integrated communication systems.

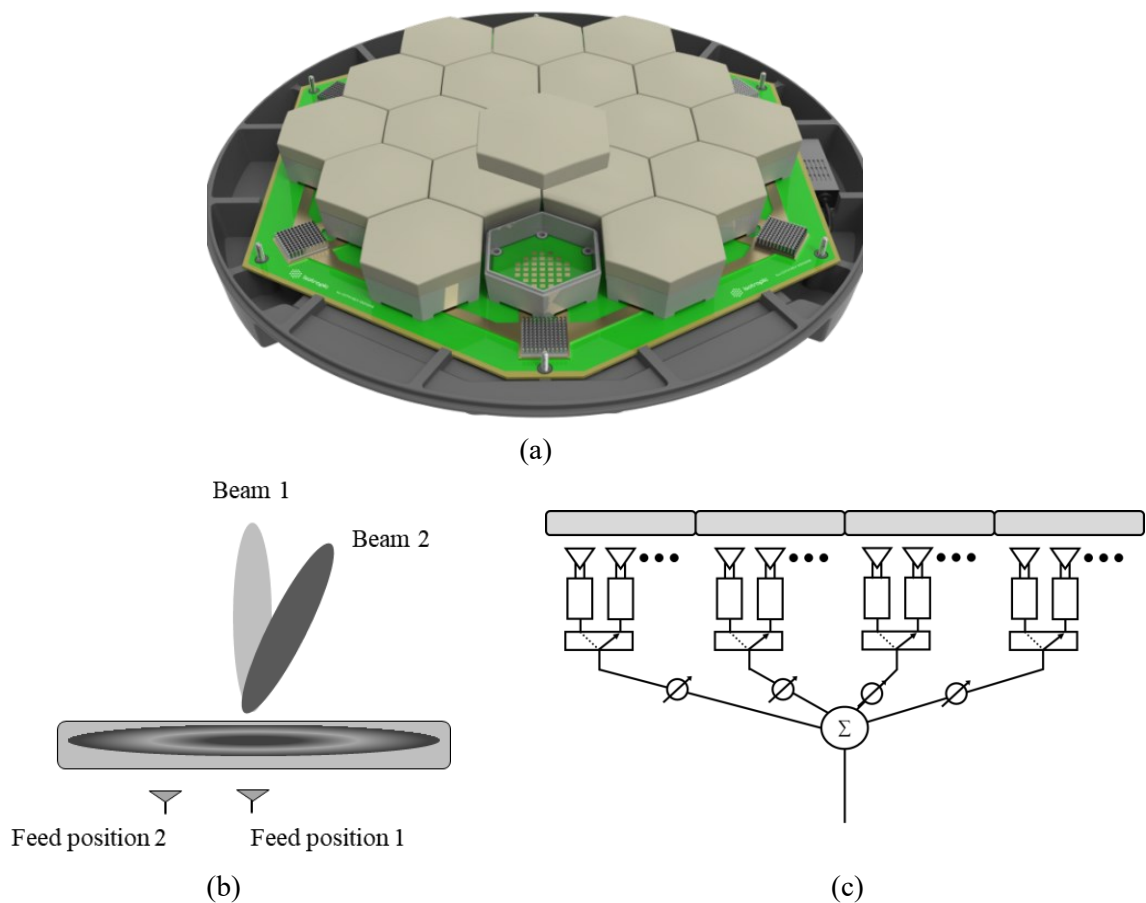


Figure 44. Design and function of the lens antenna systems: (a) isometric view of the lens antenna system [57], (b) the method of switch beam steering for the lens [56] and (c) switch beam steering network [56].

4.2 Ka band LEO antenna array target requirements and limitations

As previously explored, each LEO network has its own requirements and limitations. For this work, rather than targeting a single network, a set of requirements have been developed that target existing licensed frequency bands with a set of features that can provide compatibility with any network within this bandwidth. Table 2 displays the full set of performance requirements selected for the system. Here, a receive band of 18.8 GHz to 20.2 GHz and a transmit band to 27.5 GHz to 30 GHz has been selected. This is in line with currently licensed Ka band LEO constellations such as Amazon Project Kuiper [54]. A beam scanning range of $\theta = \pm 40^\circ$ is theoretically suitable for most LEO constellations, however in practicality $\theta = \pm 50^\circ$ is ideal to allow for factors such as the tilt of the vehicle. Finally, an axial ratio of less than 3 dB is required to ensure suitable circular polarisation efficiency. This system also targets polarisation reconfigurability to ensure maximum compatibility across LEO networks and to allow for any frequency re-use configuration. There is no quantitative gain requirement for the antenna array as this can be varied by the number of elements in the array. However, the array has been designed such that its gain stays close to the theoretical maximum at the antenna array size.

Table 2. Selected requirements for a Ka band LEO phased array antenna.

Requirement	Min	Max
Rx Frequency	18.8 GHz	20.2 GHz
Tx Frequency	27.5 GHz	30 GHz
Beam Scanning Range θ (Grating Lobe < -10 dB)	- 50°	+ 50°
Axial Ratio	0 dB	3 dB
Polarisation reconfigurable	RHCP & LHCP	

This work presents two approaches to reaching these targets. Firstly, a split aperture antenna is developed that is able to fully meet the requirements presented above in a single

low-cost PCB design. A prototype has then been manufactured to validate that this design can be realised by testing a selected set of excited elements in an array. Secondly, a shared aperture array has been developed utilising the same verified PCB manufacturing process. This design uses a triangular antenna element to ensure maximum tessellation between elements and improved isolation. This enables the shared aperture array to meet most of the requirements in a far more compact design compared to the split aperture design while still ensuring simple fabrication.

4.3 Spilt Aperture Antenna Element Design

4.3.1 Design Requirements

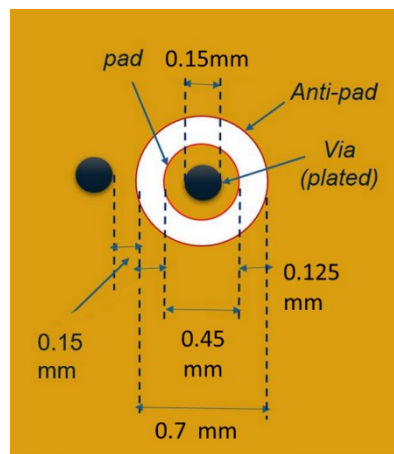


Figure 45. Parameters and limitations of PCB manufacturing. Image courtesy of Celestia UK.

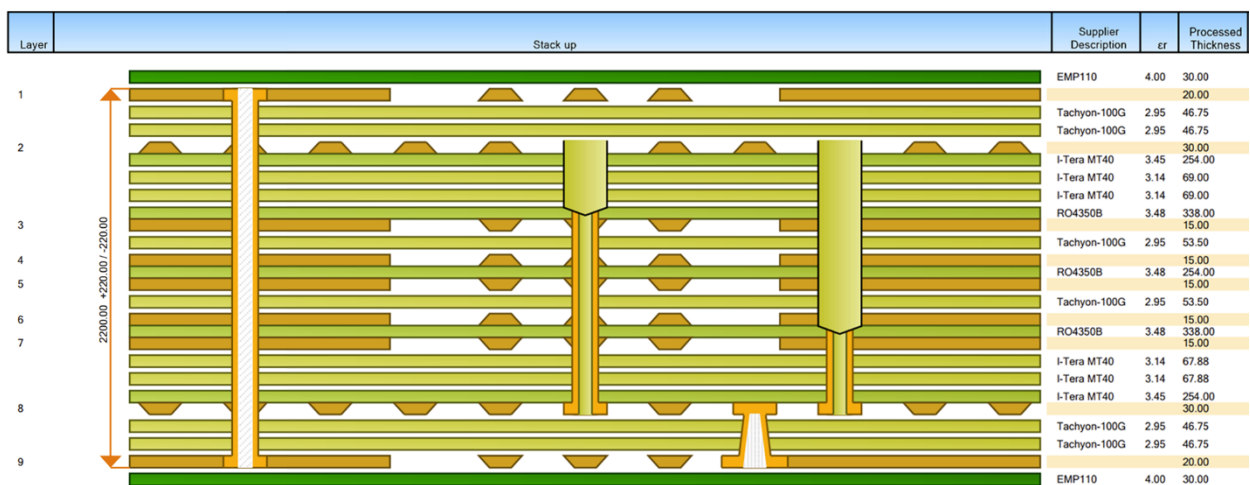


Figure 46. PCB structure and material information. Thickness is displayed in μm .

The key geometric limitations that must be taken into account when designing a phased array system are primarily dictated by the manufacturing technique used. This PCB has been designed to be manufactured using common and available techniques. For the PCB thickness and material combination used here the minimum sizes required are displayed in Figure 45. Here, the minimum plated through hole diameter is 0.15mm and a metal margin of 0.45mm is required around this hole on each metal layer of the PCB.

The PCB layer stack is presented in Figure 46 including the plated through-hole types utilised. The antennas are printed on conductive layer 1. Conductive layer 2 is left blank under the antenna to provide an un-interrupted dielectric substrate from the antenna layer to conductive layer 3. This provides a total antenna dielectric thickness of 8.23mm. While the antenna only utilises the material down to the third conductive layer, the entire PCB must be simulated in order to ensure the accuracy of EM simulations. The antenna array will be fed by a bespoke RFIC developed by Ensilica [58] that will be connected to the antenna by the plated through holes and placed on the underside of the PCB. This RFIC will control both the phase and amplitude of the antenna excitation signal. Like most RF components, this RFIC requires an impedance of 50Ω on the RF input and outputs.

4.3.2 Receive Antenna Design and Results

A circular patch antenna has been designed that covers the required bandwidth for the target receive band. This is displayed in Figure 47. The antenna element has a diameter of 4.52 mm and a net substrate thickness of 8.23mm. The antenna uses a quadrature feeding technique such that reconfigurable circular polarisation is achieved. Below the ground plane of the antenna a coaxial feeding structure has been designed using plated through holes. However, due to the limitations of the PCB manufacture and the close distance between feed locations, a standard coaxial feeding structure was not possible to implement in practice. To solve this challenge, two techniques have been implemented:

Firstly, a plated through hole is shared between both coaxial structures such that the excitation feeds can be brought closer together. This is necessary in order to place the feeding vias in their optimal location for the antenna while keeping within the PCB manufacturing requirements and maintaining a suitable impedance. As will be shown in the results, this has little impact on the isolation between these ports.

Secondly, the radius of the ground via locations around excitation feed has been reduced to target an impedance higher than 50Ω . The diameter of the patch antenna is also optimised for this higher impedance. In order to provide a 50Ω match to the RFIC, an impedance matching coplanar waveguide network has then been implemented on the bottom layer of the PCB.

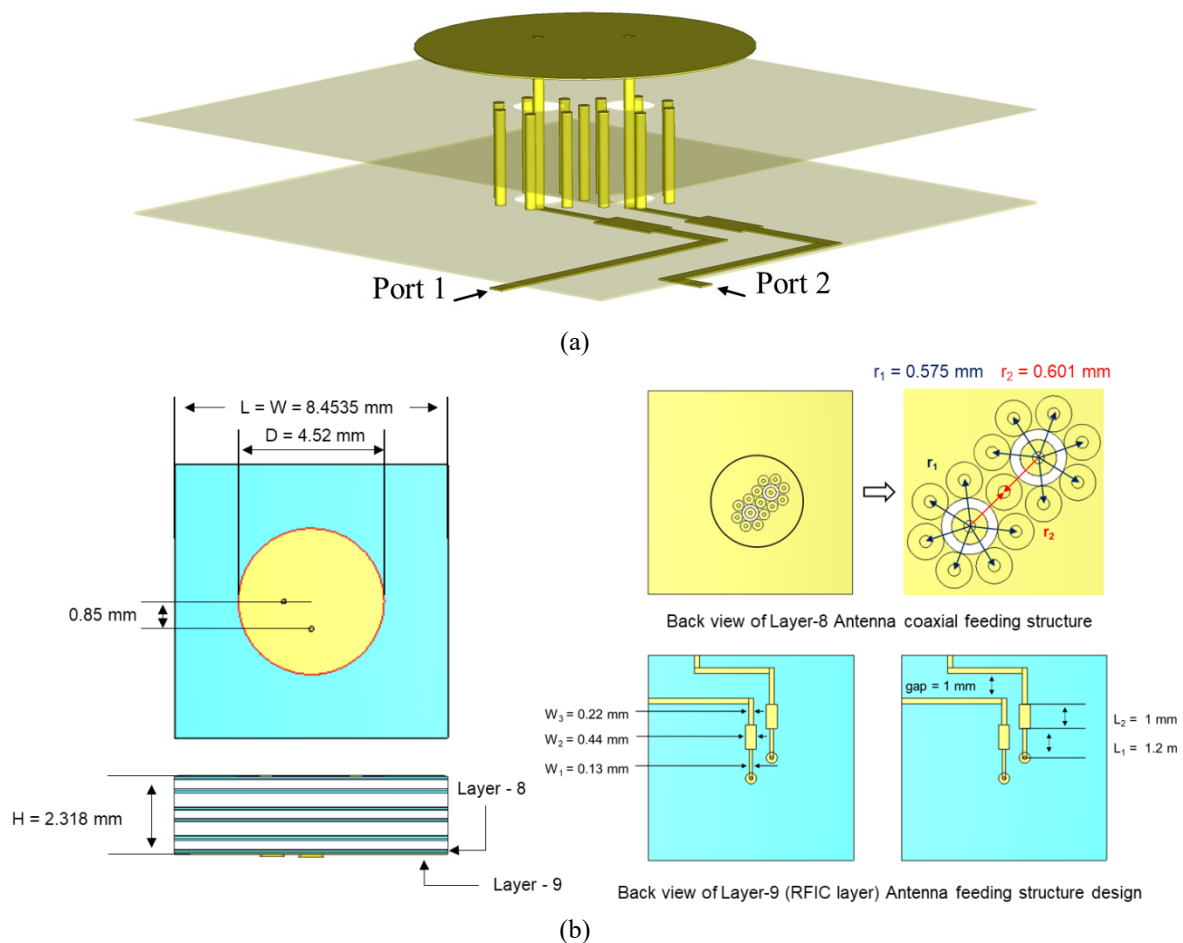


Figure 47. Receive PCB antenna design with coaxial feeding structure and transform microstrip waveguide with (a) perspective view of the antenna feeding structure including port allocation, (b) detailed top side and back views.

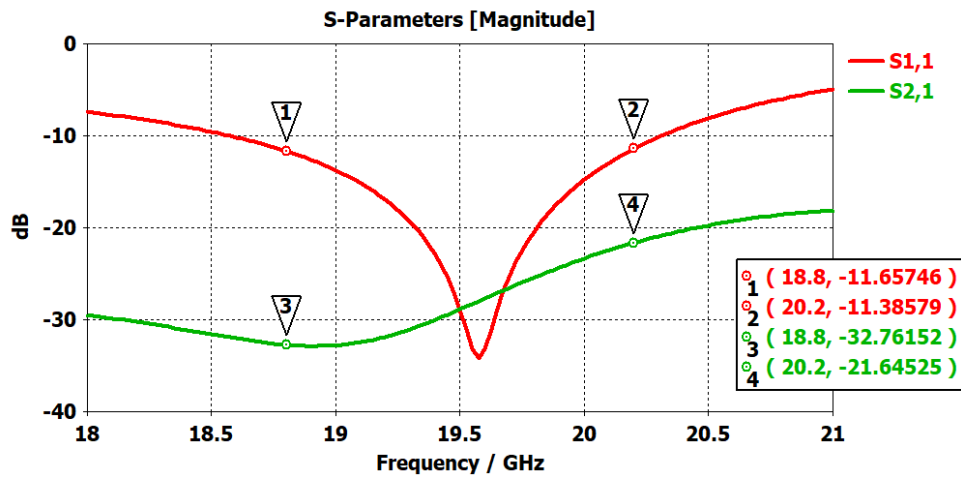


Figure 48. Reflection coefficient and isolation of the Rx circular patch antenna design

Figure 48 displays the reflection coefficient and isolation of the receive patch antenna. The design has a reflection coefficient below -11 dB across the required bandwidth. The isolation between the two excitation feeds remains below -20 dB for the required bandwidth. For both of these values, it is important to have some margin for manufacturing error.

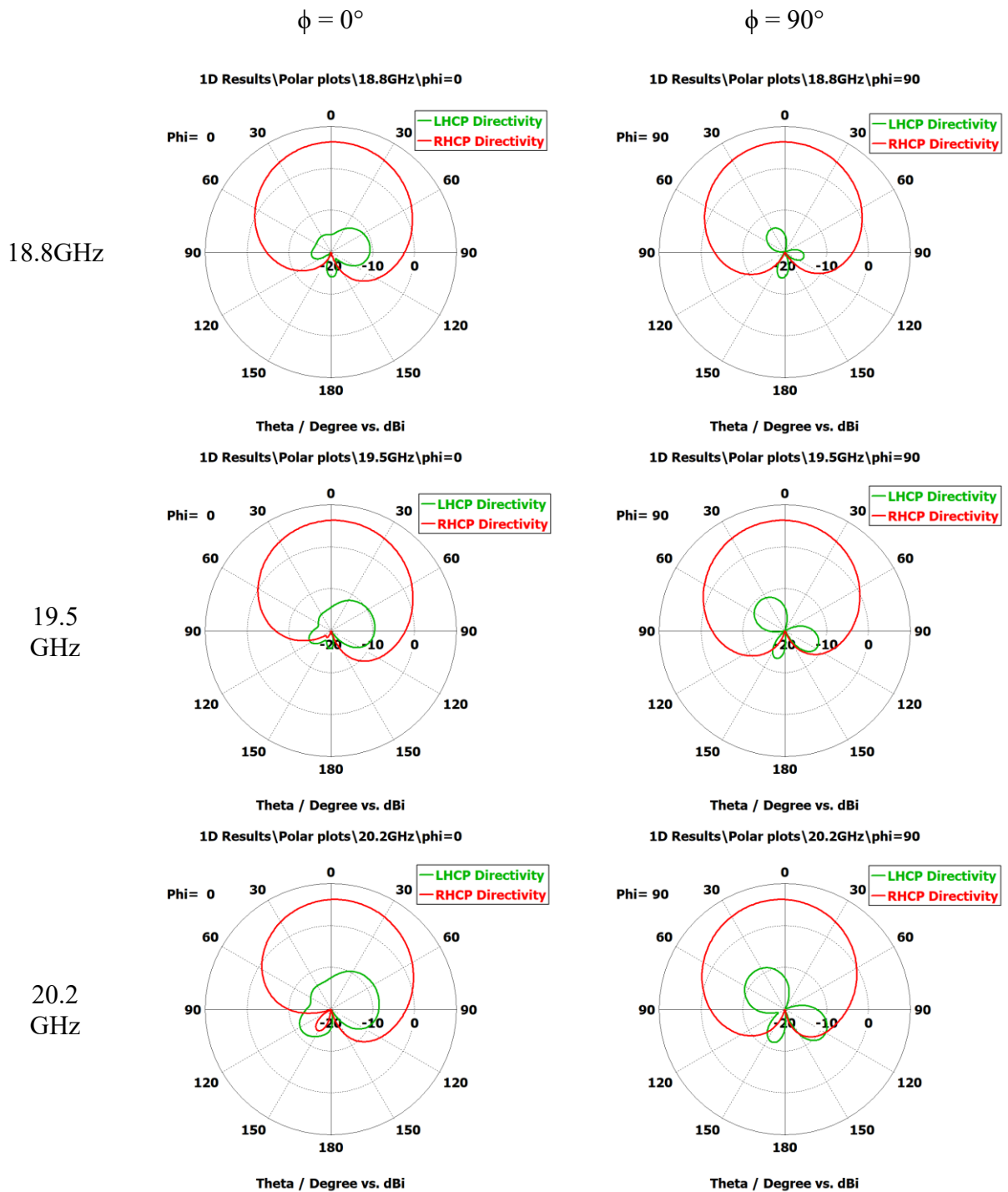


Figure 49. The radiation pattern of the Rx circular patch antenna element in RHCP mode where both ports are excited with a 90° phase difference.

Figure 49 displays the radiation pattern of the receive antenna element in RHCP mode. The co-polar (RHCP) beam remains suitable for the application across the bandwidth. The cross-polar pattern (LHCP) remains more the -10 dB below the main beam for the required beam steering region at all frequencies. Sequential rotation of the antenna element in the array is utilised to improve the resultant array axial ratio further.

4.3.3 Transmit Antenna Design and Results

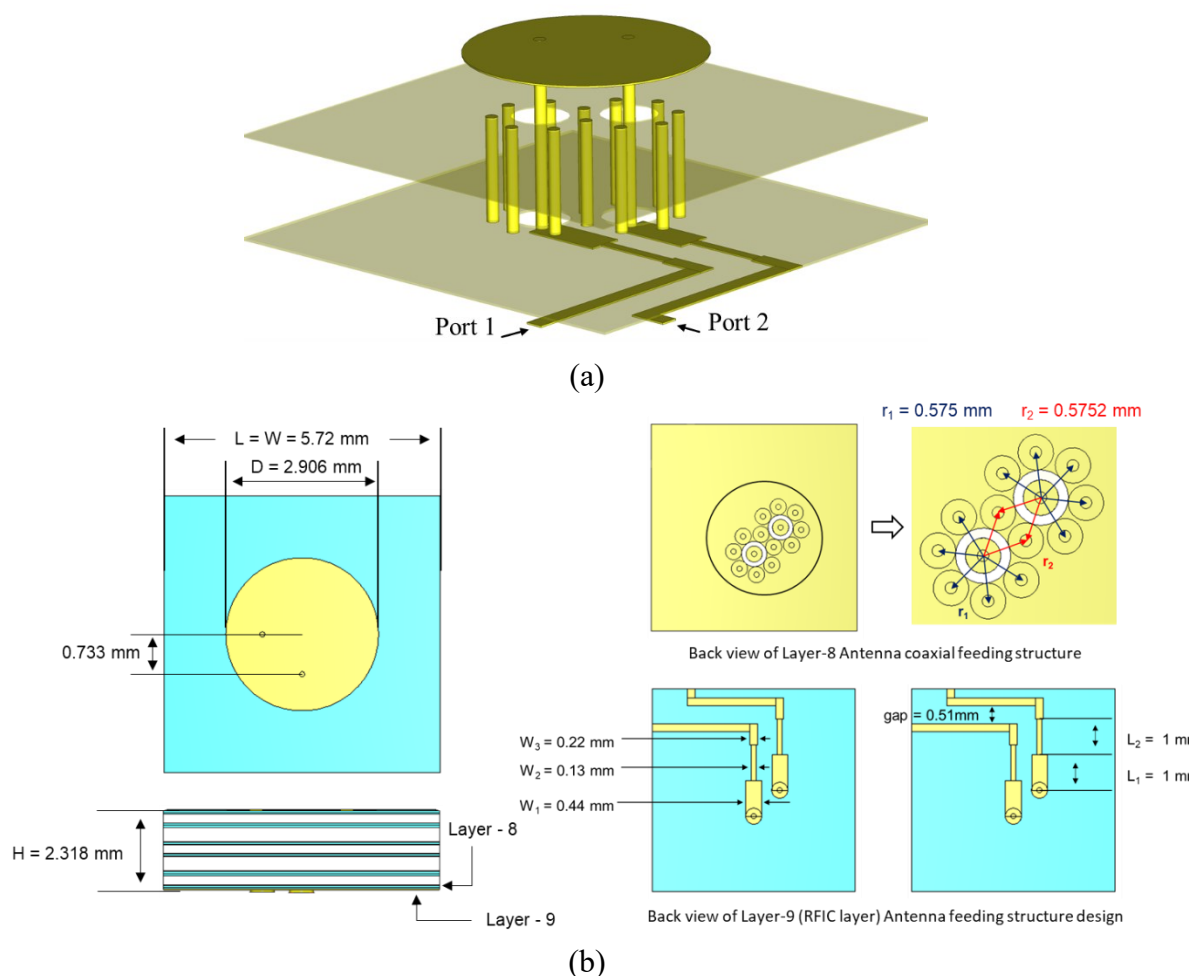


Figure 50. Transmit antenna design with coaxial feeding structure and transform microstrip waveguide with (a) perspective view of the antenna feeding structure including port allocation, (b) detailed top side and back views.

Figure 50 displays the design of the transmit antenna element. Here the antenna diameter has been reduced to 2.9 mm, but the substrate height remains 8.23 mm. The

techniques used for coaxial feeding in the receive antenna have also been implemented here to ensure efficient feeding of the antenna.

Figure 51 displays the reflection coefficient and isolation of the transmit antenna element. Due to the higher frequency of the antenna and constant substrate height between Rx and Tx elements, the bandwidth of the antenna is far greater than that of the receive antenna. Here, the transmit antenna provides a reflection coefficient of < -18 dB for the targeted bandwidth. The isolation between excitation feeds remains < -27.5 dB for the targeted bandwidth.

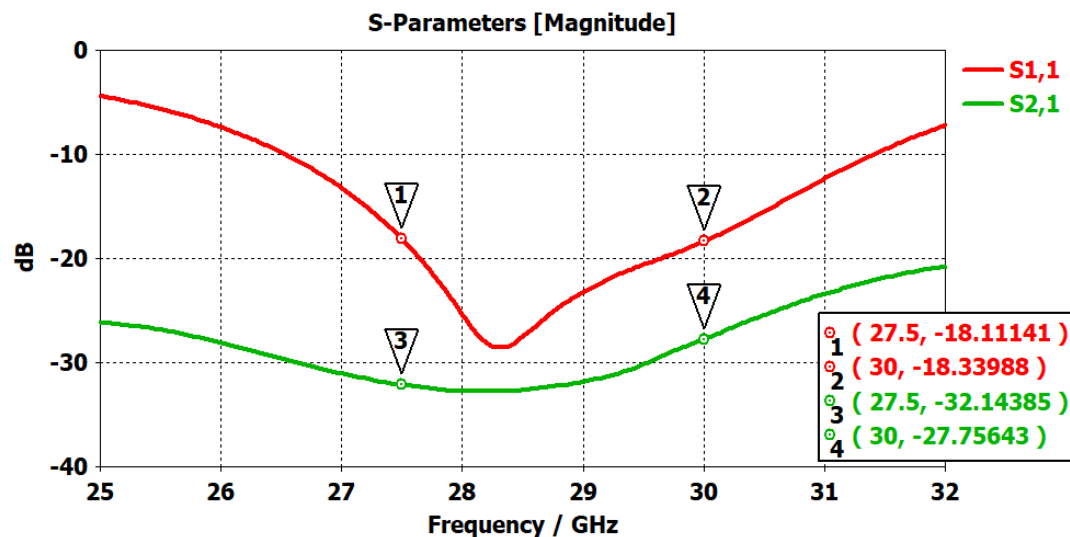


Figure 51. Reflection coefficient and isolation of the Tx circular patch antenna design

Figure 52 displays the radiation patterns of the transmit antenna element in RHCP mode across the Tx bandwidth. Similarly, to the receive antenna element, the co-polar (RHCP) patterns remain consistent with frequency and the cross polar isolation remains below -10 dB. Again, the sequential rotation of the array presented in the next section will further improve the overall axial ratio.

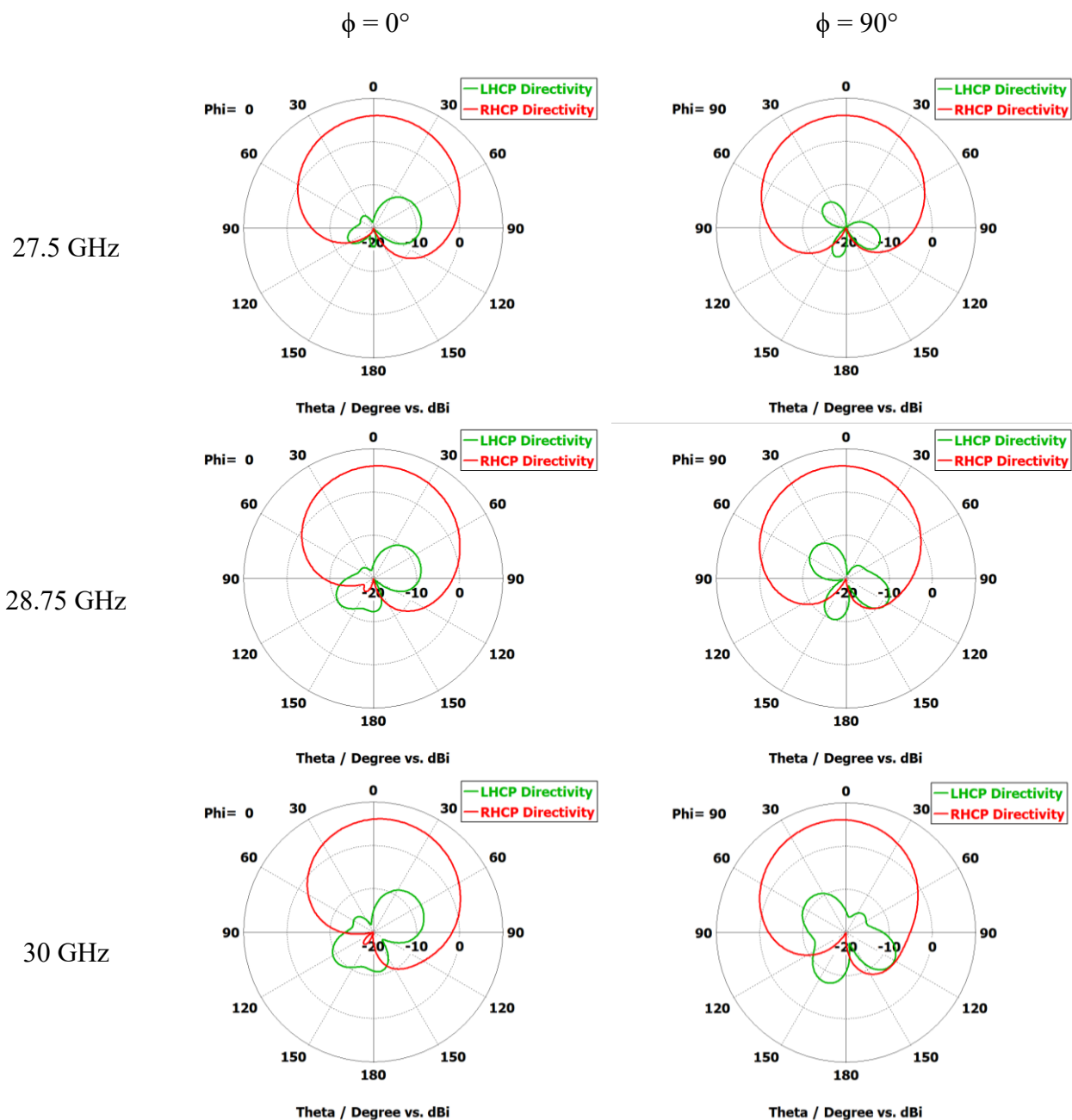


Figure 52. The radiation pattern of the Tx circular patch antenna element in RHCP mode where both ports are excited with a 90° phase difference.

4.4 Split Aperture Antenna Array

4.4.1 Antenna array topology optimisation

During the optimisation and design process, a number of topologies were analysed to find the optimal solution for beam steering while maintaining the required Axial Ratio (AR). Primarily, the rotation of elements was altered to reduce the effect of AR variation in unit pattern over the frequency bandwidth (particularly in the Tx elements). These topologies are presented in Figure 53.

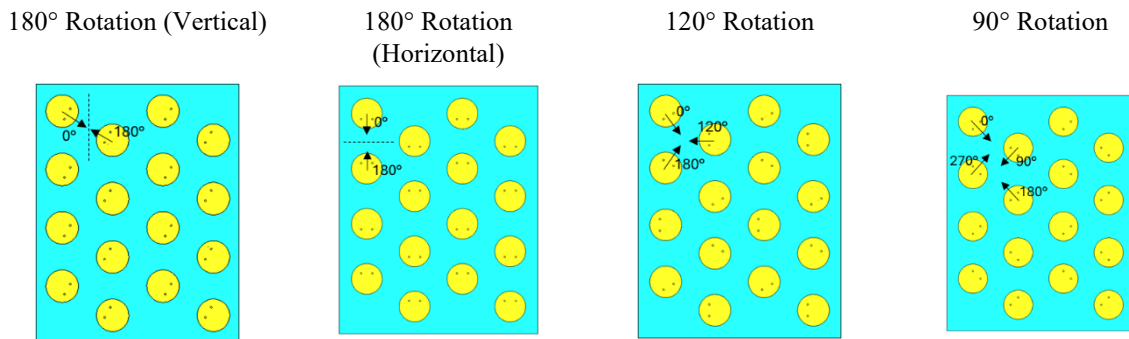


Figure 53. A series of antenna array topologies tested to provide optimal beamforming and axial ratio.

Table 3. Results of antenna array rotation topology for gain, grating lobes and axial ratio.

	180deg (Vertical)	180deg (Horizontal)	120deg	90deg
Gain at 0°	15.6	16.7	16.6	16.5
Gain at 50° (Min)	15.4	15.3	14.7	15
Grating Lobe at 0°	-8.28	-13.1	-12.7	-11.8
Grating Lobe at 50° (Max)	-9.5	-7.2	-7.5	-8.5
Axial Ratio at 0°	3.3	1.73	0.42	0.9
Axial Ratio at 50° (Max)	2.6	2.5	1.3	1.2

All of these topologies improve the AR performance drastically over a standard array with no rotation. The 90° element rotation has been selected as it provided the lowest axial

ratio at all steering angles. While 120° rotation is found to provide similar performance, this topology was difficult to feed optimally from the first generation RFIC. Table 3 shows the initial AR improvement in a 4×4 array.

An example of the phase shifting method for the selected 90° sequential rotation is displayed in Figure 54. Firstly, a phase related to the rotation of each antenna is assigned per element i.e. 0° , 90° , 180° or 270° . Depending on the desired polarisation, this value can be added or subtracted from the phase value of each element. Secondly, a phase shifting value for steering the beam is applied per element. Here a basic array factor calculation is used to determine the required value of α in the x and y direction. Finally, a 90° phase shift is applied to the quadrature feeding ports (in the same angular direction as the 90° rotated sub array). By changing the phase of the quadrature feeding and antenna rotation phase, the polarisation of the array can be reconfigured (i.e. LHCP or RHCP).

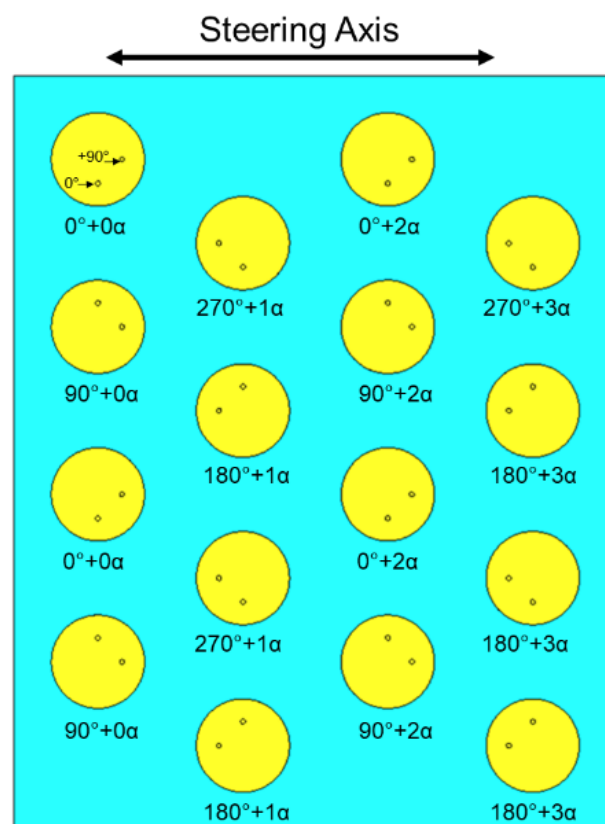


Figure 54. Phase shifting method when utilising 90° sequential rotation.

4.4.2 Receive antenna array design and simulation

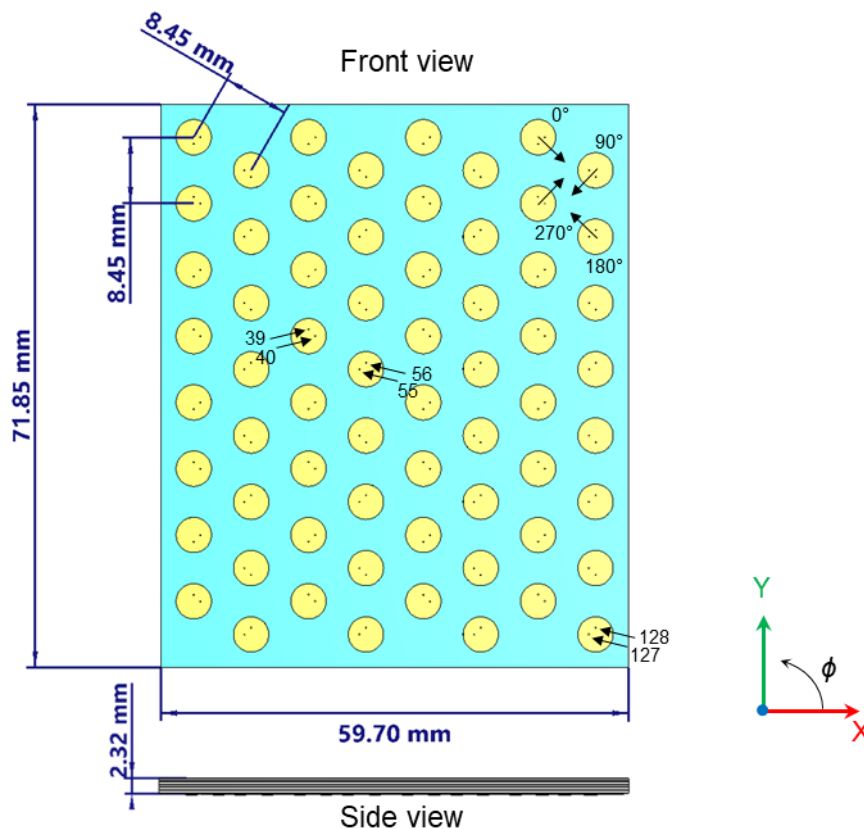


Figure 55. 8x8 receive antenna array design with 90° sequential element rotation and a triangular lattice.

Figure 55 displays the simulated 8 x 8 receive array model with 90° element rotation. An element spacing of approximately 0.5λ is often the optimal distance for phased arrays as this distance limits the level of mutual coupling between elements while also limiting the level of back lobes at high steering angles. It was found that this distance was too compact to develop an effective feeding network when the first revision RFICs are included. Hence, an element spacing of 0.55λ at the centre frequency has been selected for the simulations as it provides a good balance between grating lobe reduction and gain enhancement. A second revision of the RFICs has since been developed with a smaller footprint to allow for future array optimisation and the shared aperture topology developed in Section 4.7. It should be noted that the impedance feeding network is not included in the array simulation as it requires a microstrip

waveguide to coaxial feeding connector that could introduces inaccuracies and losses. Further, given the complexity of the simulation, the required increase in mesh cells to accommodate such as design is not feasible on even a high end workstations. Here, the antenna elements are excited by direct bottom feeding as in previous analysis. Hence, without the impedance transform to 50Ω , the s-parameters and efficiency of the array cannot be accurately simulated. However, as directivity is not reliant of the efficiency of the antenna, the beam steering capabilities of the array are still able to be analysed.

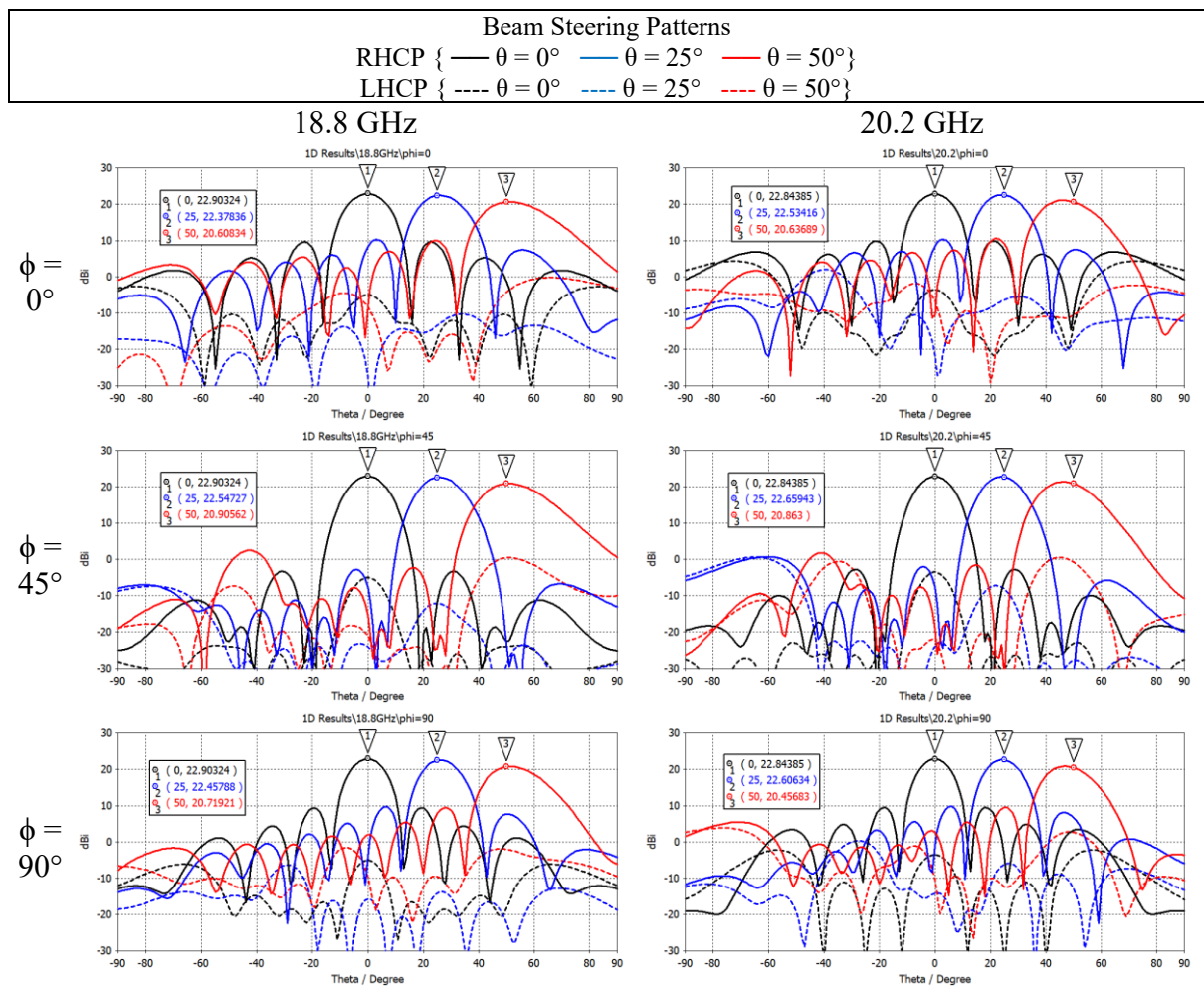


Figure 56. Beamforming of the Rx antenna array in RHCP mode across the operational bandwidth.

Figure 56 displays the simulated beam steering performance of the 8×8 receive antenna design at the maximum and minimum frequencies of the targeted bandwidth. Here it is demonstrated that the antenna array is capable of beamforming to 50° from the boresight direction with less than 3dB reduction in directivity at all frequencies. The grating lobes remain more than -10 dB from the main lobe at all frequencies. Finally, the co-polar and cross-polar isolation remains greater than 20 dB at all frequencies. The steering performance of this array is symmetric though not all angles are shown for length and clarity.

4.4.3 Transmit antenna array design and simulation

The design of a transmit antenna array is presented in Figure 57. Here, 90° sequential rotation and 0.55λ spacing has also been utilised. Again, the antenna elements are excited by direct feeding and the impedance matching network are not included in the simulation.

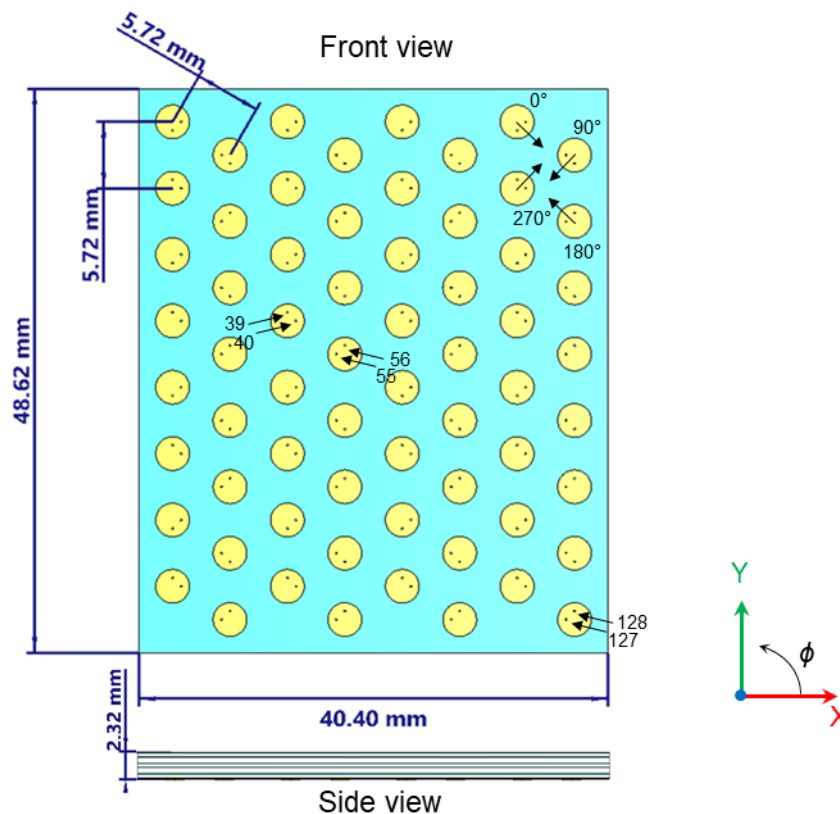


Figure 57. 8×8 receive antenna array design with 90° sequential element rotation and a triangular lattice.

Figure 58 presents the beam steering performance of the transmit antenna array. Here the steering loss remains below 3 dB at lower frequencies and increases slightly to 3.3 dB at 30GHz . The grating lobe remains less than -10 dB from the main lobe at lower frequencies and increases slightly to -9.9 dB at 30 GHz. Similarly, the axial ratio remains below 3 dB at all frequencies and angles except for 30 GHz at 50° where it increases to 3.3 dB.

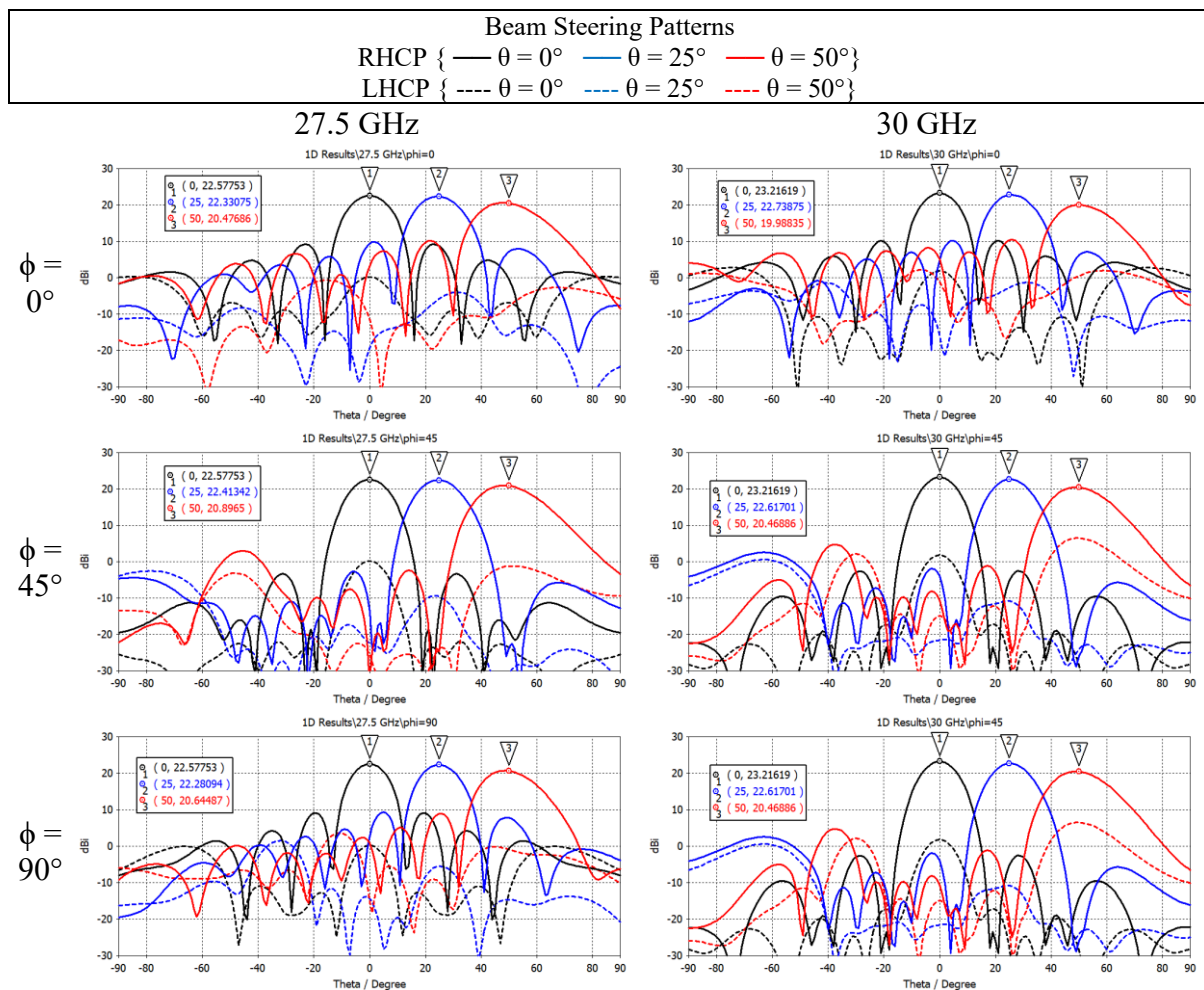


Figure 58. Beamforming of the Rx antenna array in RHCP mode across the operational bandwidth.

Overall, this design performs well, except at extreme angles and frequencies where it falls slightly below the target performance. Here the results have been found by applying only phase shifting. Were amplitude tapering also applied, it is likely that the grating lobe would reduce and there would be room to further optimise other aspects of performance.

4.5 Split Aperture Antenna Array Prototype Measurements and Results

In order to verify the performance of the antenna design and its fabrication, a prototype board has been developed in collaboration with Celestia UK. This board, shown in Figure 59, uses two “dummy” antenna arrays based on the receive and transmit arrays presented in the previous sections. Here only five of the excitation ports in each antenna array have been fed. The surrounding antenna elements are metal patches with no feeding attached. This has been done to reduce the impact of surface waves on each excited antenna element. To verify the accuracy of the design and fabrication, a simulation of a large portion of the prototype has been undertaken including feeding lines and plated through holes around the array.

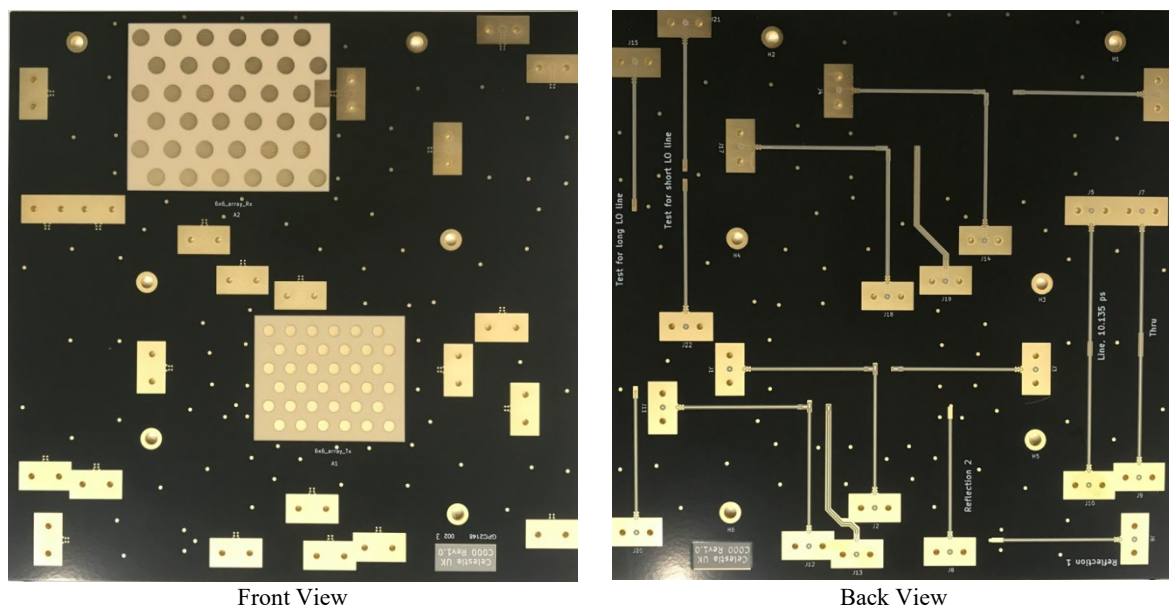


Figure 59. Prototype board developed by Celestia UK using the split aperture designs presented here.

4.5.1 Receive measured results

The structure of the receive prototype section is presented in Figure 60 including the labelled excited ports. In order to maintain a reasonable processing time and stay within memory restrictions of the EM software used, the receive and transmit sections of the board have been simulated separately. The model and simulated Rx section of the board is displayed in Figure 60 (b).

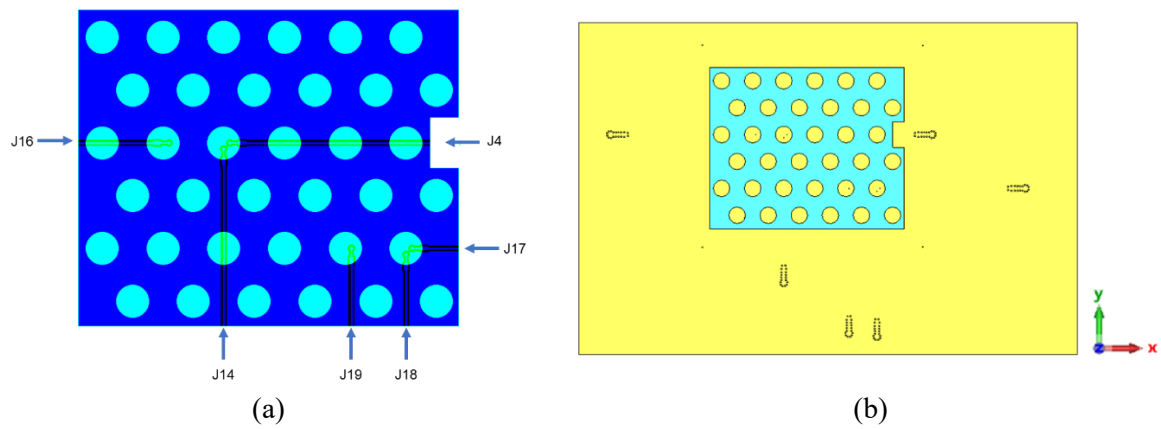


Figure 60. Structure of the simulated Rx section of the prototype board. (a) Excited ports and location. (b) Simulated design.

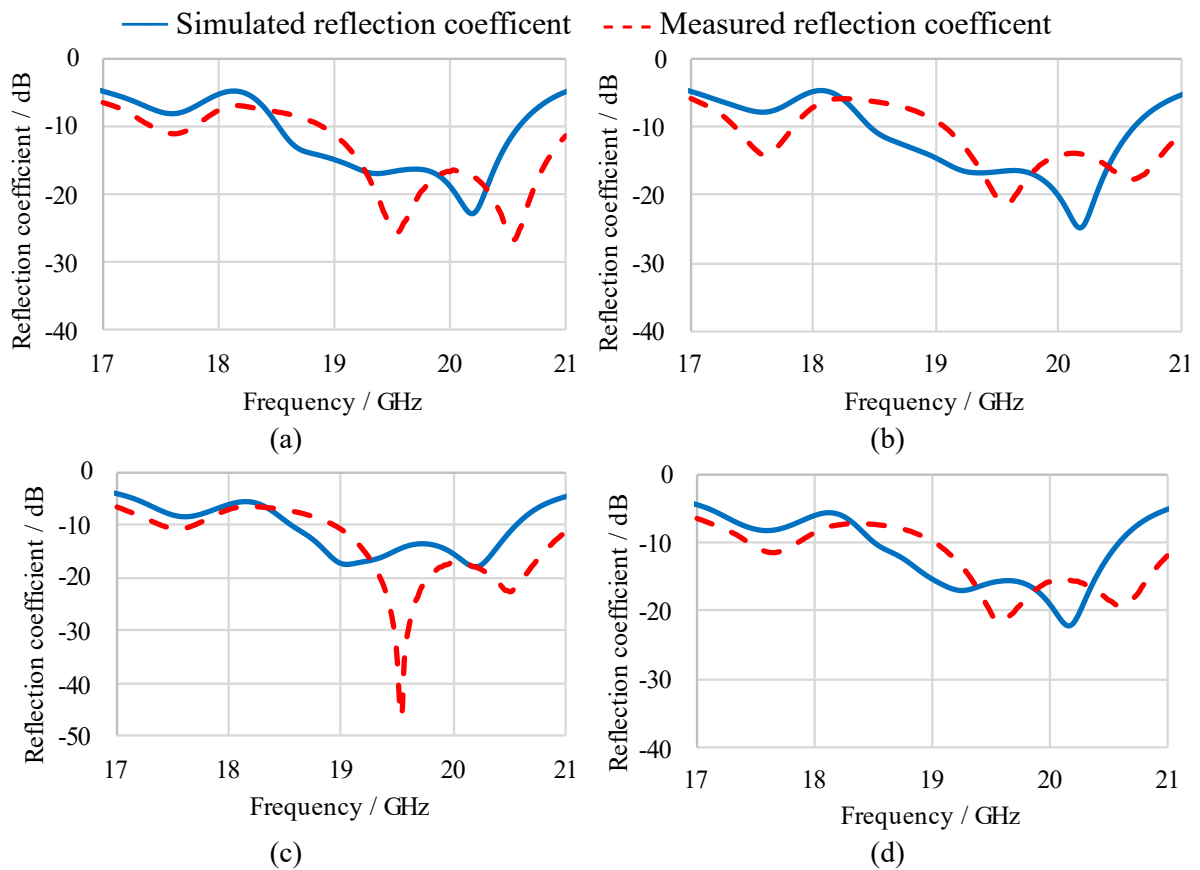


Figure 61. Measured and simulated reflection coefficient of the Rx prototype antenna excitation ports (a) J14, (b) J16, (c) J17 and (d) J19.

Figure 61 displays the measured and simulated reflection coefficient for port J14, J16, J17 and J19. The simulated reflection coefficient presented here is slightly different from the unit element result (potentially because only a section of the complete PCB has been simulated) but the simulated performance still provides coverage of the targeted bandwidth for all ports. The measured results displays a slight shift towards a higher frequency for all tested receive antenna. As a result, between 18.8 and 19 GHz the reflection coefficient of the excited ports increases slightly above -10 dB. From this data the antenna diameter can simply be reduced in diameter by a small amount to account for this error. Alternatively, by further optimising the feeding network to increase the reflection bandwidth of the antenna, an increased margin in bandwidth would allow for not only the variation presented here, but other slight variations caused by fabrication inconsistencies. The isolation of the prototype receive antenna elements are presented in Figure 62. Here, an isolation level below -20 dB is demonstrated between all excited ports. In these results, the impact of the feed lines have been removed by calibration with various test lines, as shown in Figure 59. Prototype board developed by Celestia UK using the split aperture designs presented here..

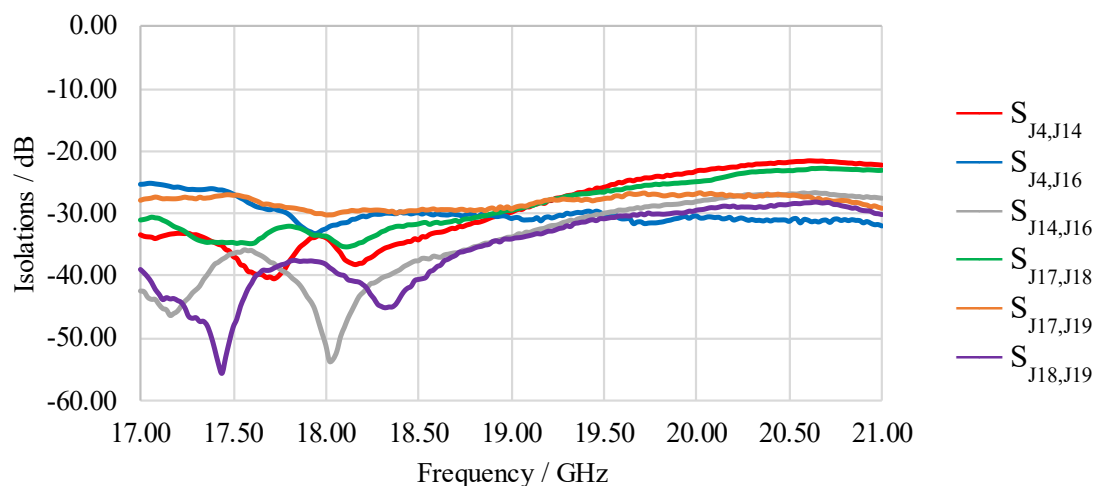


Figure 62. Measured isolation between ports of the Rx prototype antenna array.

The radiation patterns of the simulated and measured receive antenna array prototype are displayed in Figure 63. There is a clear match between the simulated patterns and measured patterns with only minimal variation over the targeted beam steering angles. Much like the reflection coefficient, variation between the radiation pattern of the simulation of the element in free space and the element in the prototype is expected. This close match between simulation demonstrates the suitability of the design and accuracy of the fabrication process at the receive frequencies for the radiation pattern of the antenna.

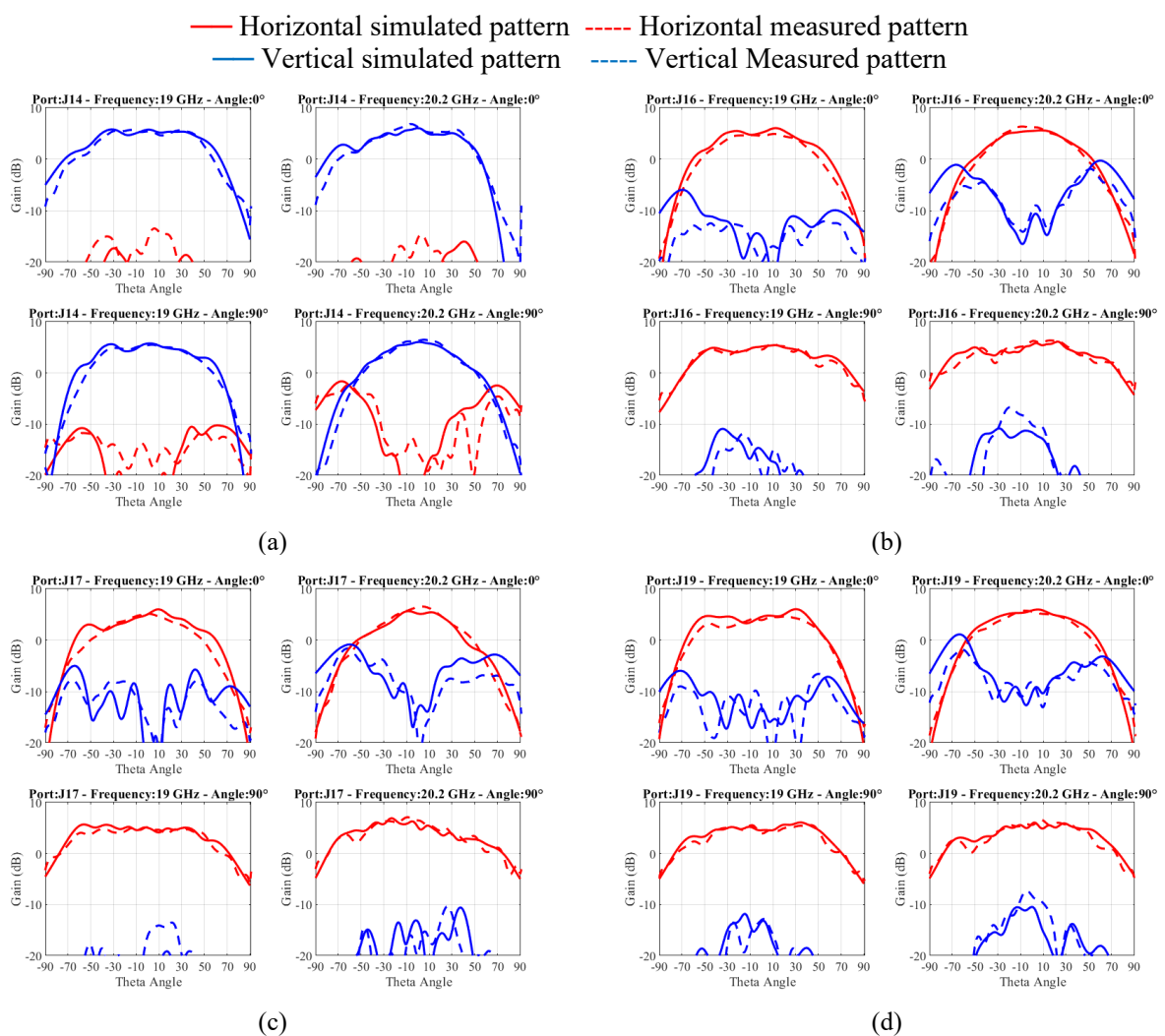


Figure 63. Simulated and measured pattern of the prototype receive antenna array excitation ports (a) J14, (b) J16, (c) J17 and (d) J19.

4.5.2 Transmit measured results

As with the receive prototype antenna array, only the section of the prototype directly surrounding the transmit antenna array has been simulated. This simulated section of the board and the selected excited ports are displayed in Figure 64.

The simulated and measured reflection coefficient of the prototype are presented in Figure 65. Again, there is some variation in simulated reflection coefficient from that presented in the element simulations. The measured reflection coefficient remains higher than the simulated results for all ports across the majority of the bandwidth. However, despite this increase, all measured results remain below -10 dB for the required bandwidth. The measured reflection coefficient of the transmit elements matches the simulated prototype results well and provide complete coverage of the targeted bandwidth. The measured isolation between ports in the transmit prototype is presented in Figure 66. Here, the isolation between ports remains below -20 dB for the targeted bandwidth.

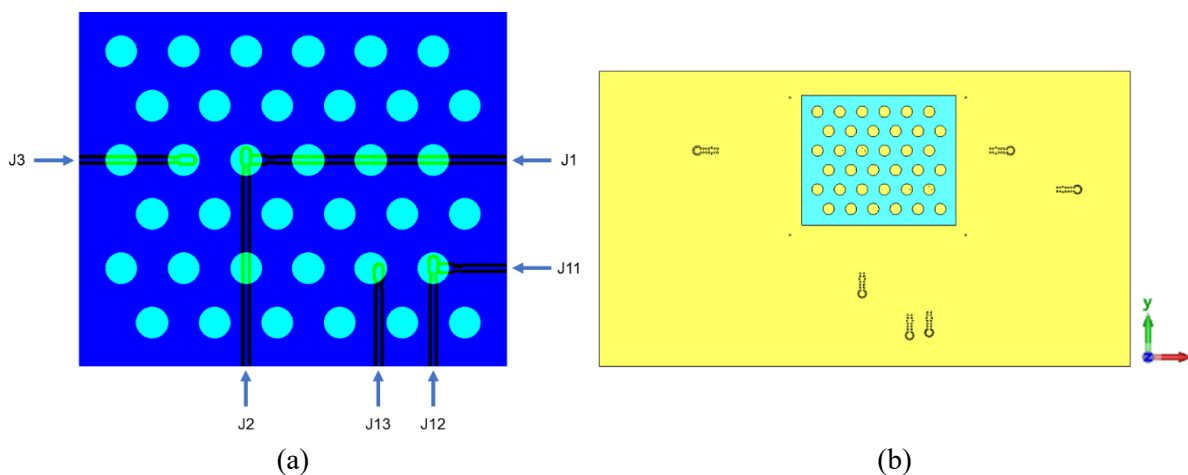


Figure 64. Structure of the simulated Tx section of the prototype board. (a) Excited ports and location. (b) Simulated design.

The simulated and measured radiation patterns are presented in Figure 67. As previously, the prototype's radiation pattern is not expected to match the simulated radiation pattern of the unit element in free space presented earlier. Here, the simulated prototype

elements and the measured prototype elements match well. There is slightly more variation shown here than in the receive antenna elements, but not to a significant degree. J2 shows the most variation at 27.5 GHz at $\phi = 90^\circ$ and $\theta = 10^\circ$. This variation in J2 is due to the limited size of the simulated prototype and the proximity of J2 to the edge of the simulated area. This caused some amount of radiation generated at the edge of the simulated prototype and, as a result, deconstructive interference can be seen in the simulation and not the measurement.

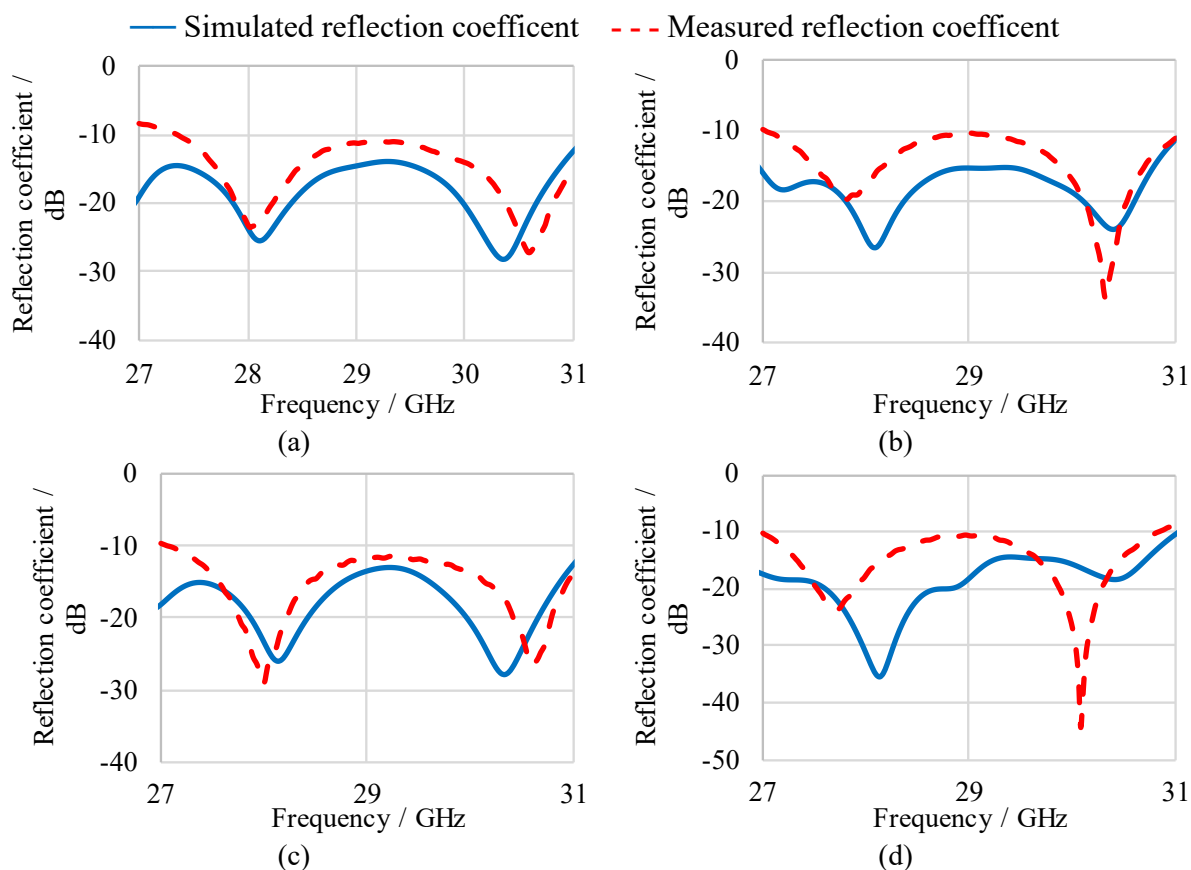


Figure 65. Measured and simulated reflection coefficient of the Tx prototype antenna elements (a) J1, (b), J2, (c) J11 and (d) J13.

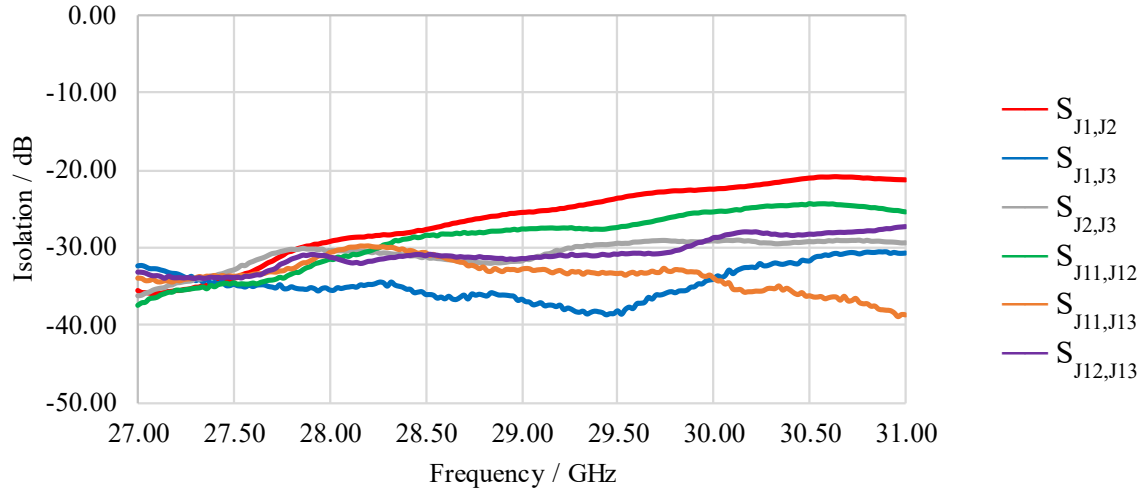


Figure 66. Isolation between ports of the Tx prototype antenna array.

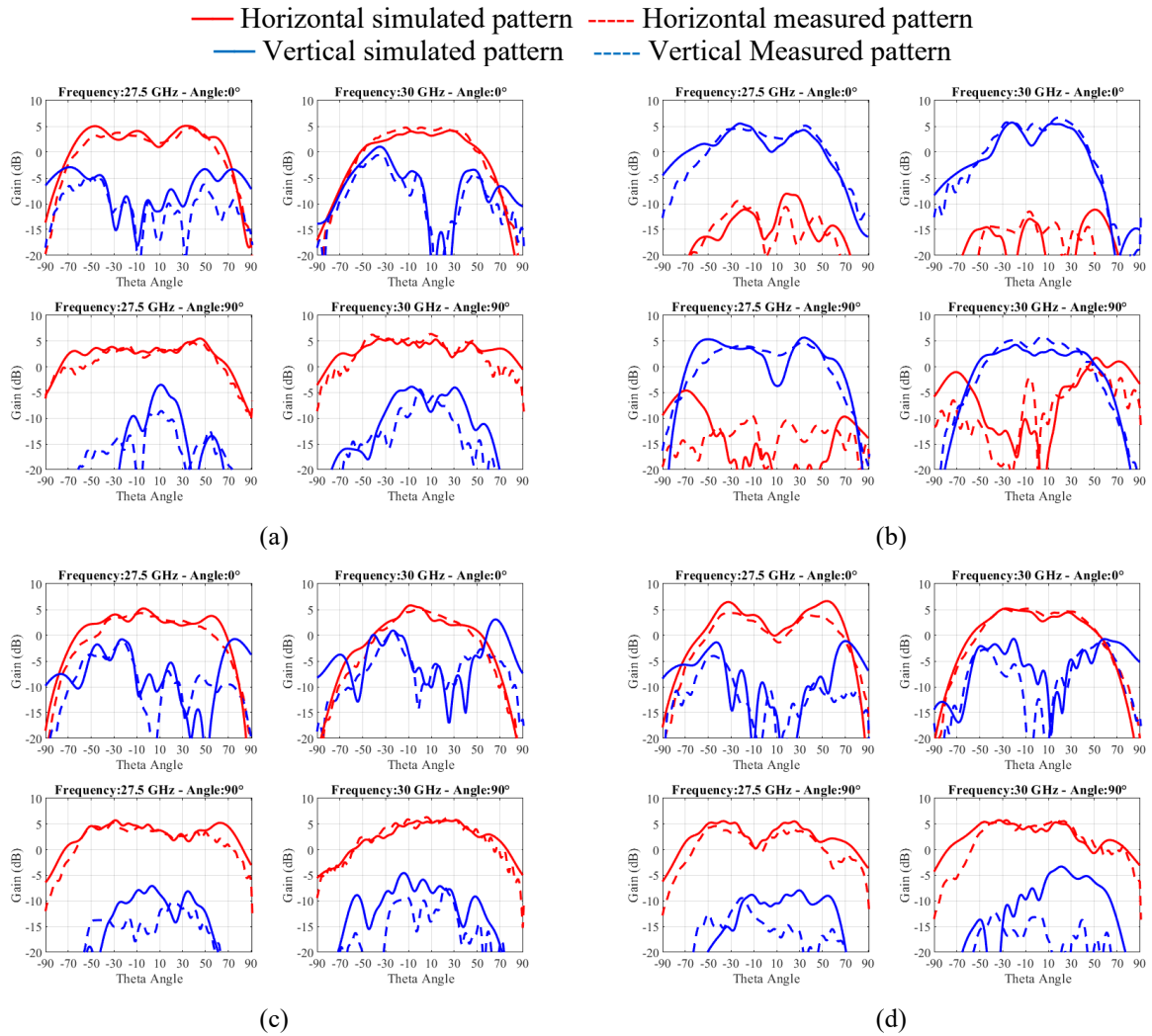


Figure 67. Simulated and measured pattern of the prototype transmit antenna array excitation ports (a) J1, (b) J2, (c) J11 and (d) J13.

4.6 Shared Aperture Antenna Array

Utilising the coaxial feeding method and matching co-planar waveguide techniques developed for the split aperture array, a shared aperture antenna array has been developed. As shown in previous work at the start of this chapter, some designs [50] use a 1:2 ratio of Rx to Tx antenna elements and others use a 1:1 ratio [54]. Here a 1:1 ratio of antenna elements has been utilised as this is not only better suited to the RFIC developed for this project but also increases the gain of the Tx sub array to mitigate the increased free space losses at higher frequencies.

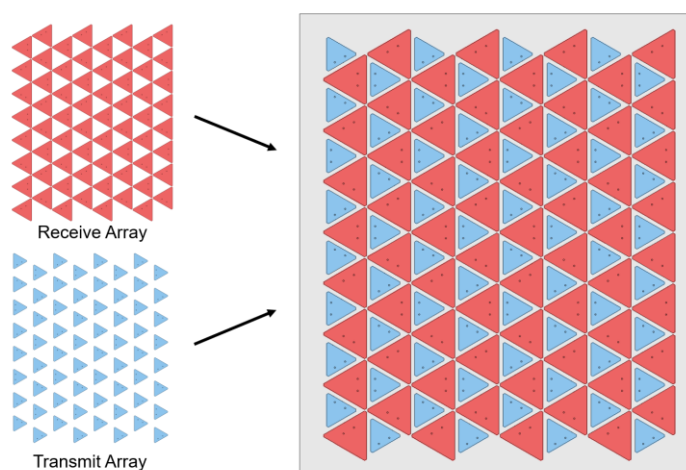


Figure 68. Interlaced Shared Aperture Topology. Rx elements shown in red. Tx elements shown in blue.

Initially, interlacing the existing split aperture circular antenna elements was attempted. However, it was found that the circular patches used for split aperture functionality did not provide optimal tessellation between elements and, as a result, the beam steering performance of the transmit antenna array was significantly reduced due to the increase in space between elements. To solve this challenge, triangular elements were developed that also allowed for dual circular polarisation functionality. The triangular elements presented here are similar to the dual circularly polarised design presented in [59]. Here the design has been improved by applying bevelling the corners of the patch to allow for closer tessellation.

When these triangular antenna elements are placed in the shared aperture antenna array (Figure 68), the inter-element distance can be reduced and, as a result, the beam steering performance of the array is greatly improved.

4.6.1 Receive Element Design

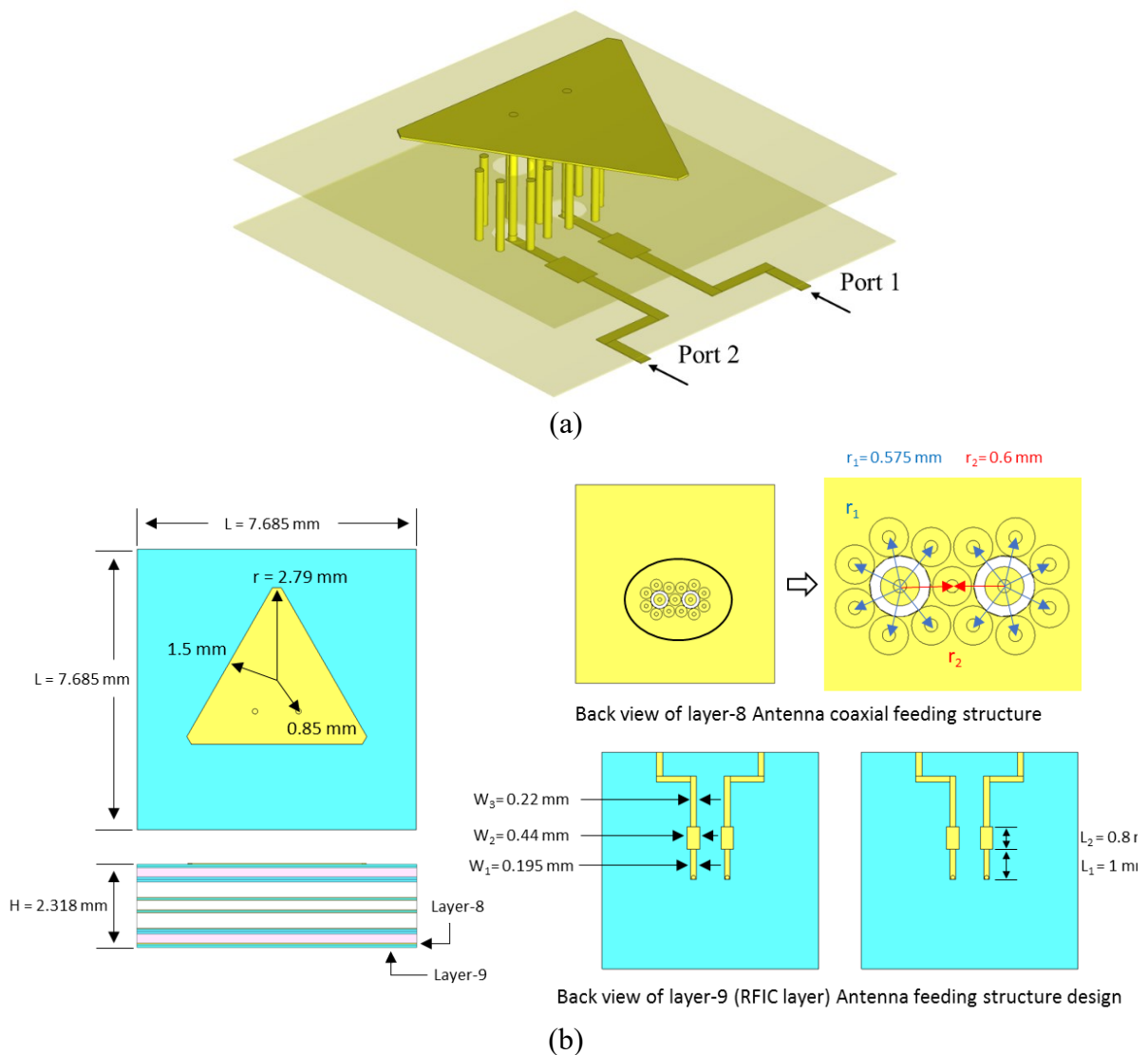


Figure 69. Bevelled triangular receive patch antenna element and coaxial feeding design. Shows (a) perspective view with port allocation and (b) detailed top, side and back views.

The triangular receive element design is displayed in Figure 69. Here the same PCB stack structure and design parameters used for the split aperture antenna (Figure 46) is utilised to ensure feasibility of fabrication. The antenna presented here utilises triangle design with a

minimum distance from the centre of 1.5 mm. A bevel of radius 2.79 mm is then applied to reduce coupling with other receive antenna elements at the corner of the design. A quadrature feed is utilised to enable reconfigurable circular polarisation. A similar feeding structure to the split aperture antennas has been utilised here where a coaxial structure from conductive layer 9 to the antenna ground plan is designed with impedance greater than 50Ω and an impedance matching structure is then added on the underside of the PCB.

Figure 70 displays the simulated reflection coefficient of the receive triangular antenna design. Here, the reflection coefficient remains below -10 dB and the isolation remains below -20 dB for the targeted bandwidth.

The radiation pattern of the triangular receive antenna element is presented in Figure 71. Here the antenna is in its RHCP polarisation mode though, given the symmetrical design, LHCP mode will be identical with the alternate co and cross-polarisations. The radiation pattern remains consistent over the targeted bandwidth, and the cross and co polar isolation remains greater than 10 dB across the required beamwidth. Much like the split aperture design, sequential rotation is utilised in the antenna array to further improve the axial ratio of the array as a whole.

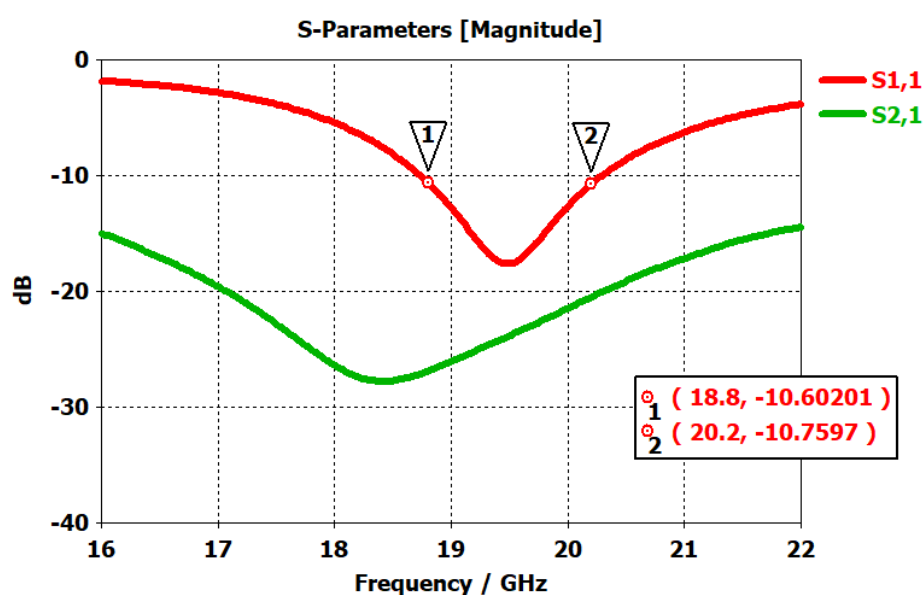


Figure 70. Reflection coefficient and isolation of the Rx bevelled triangular patch antenna element.

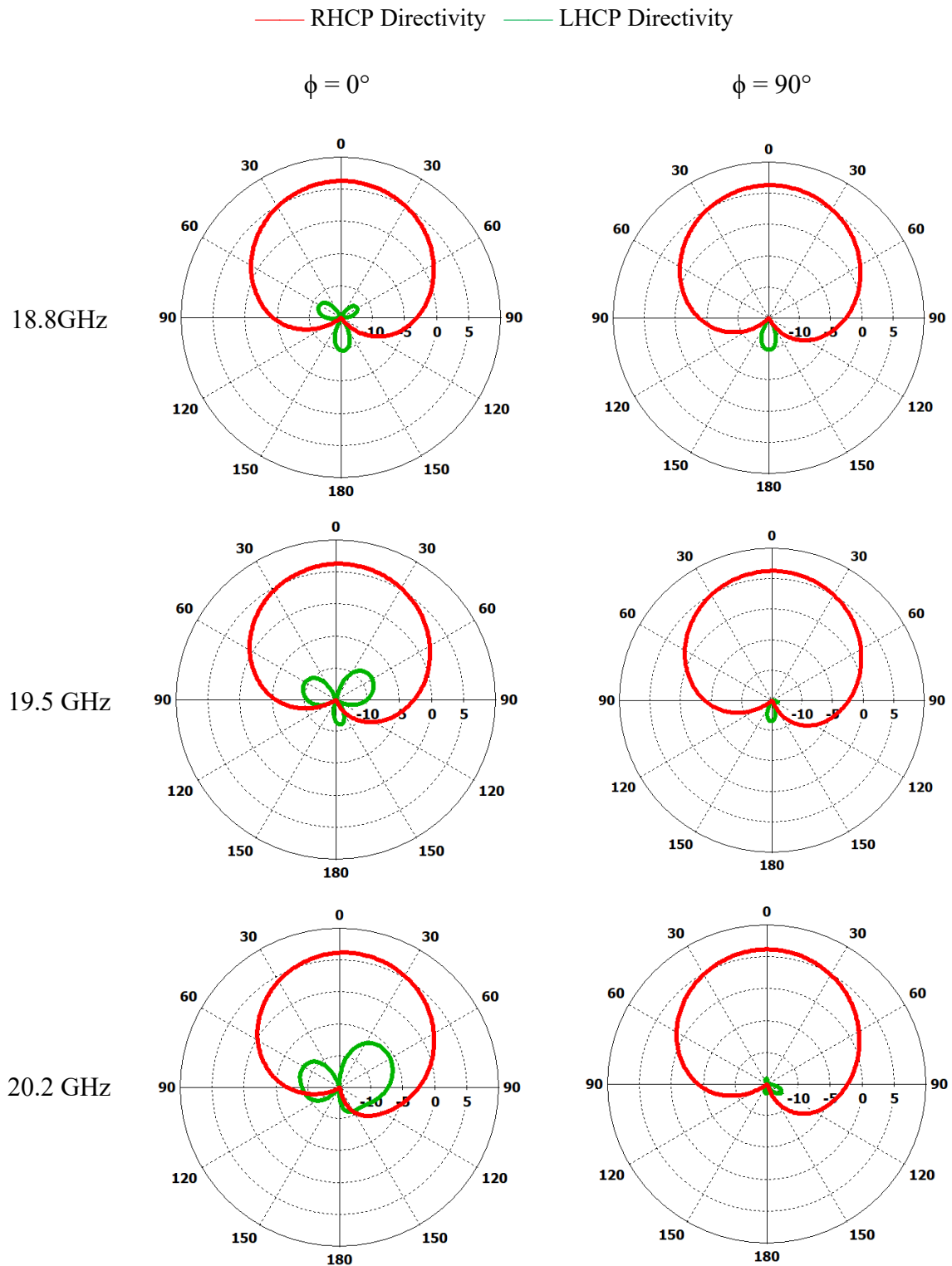


Figure 71. The radiation pattern of the Rx bevelled triangular patch antenna element in RHCP mode where both ports are excited with a 90° phase difference.

4.6.2 Transmit Element

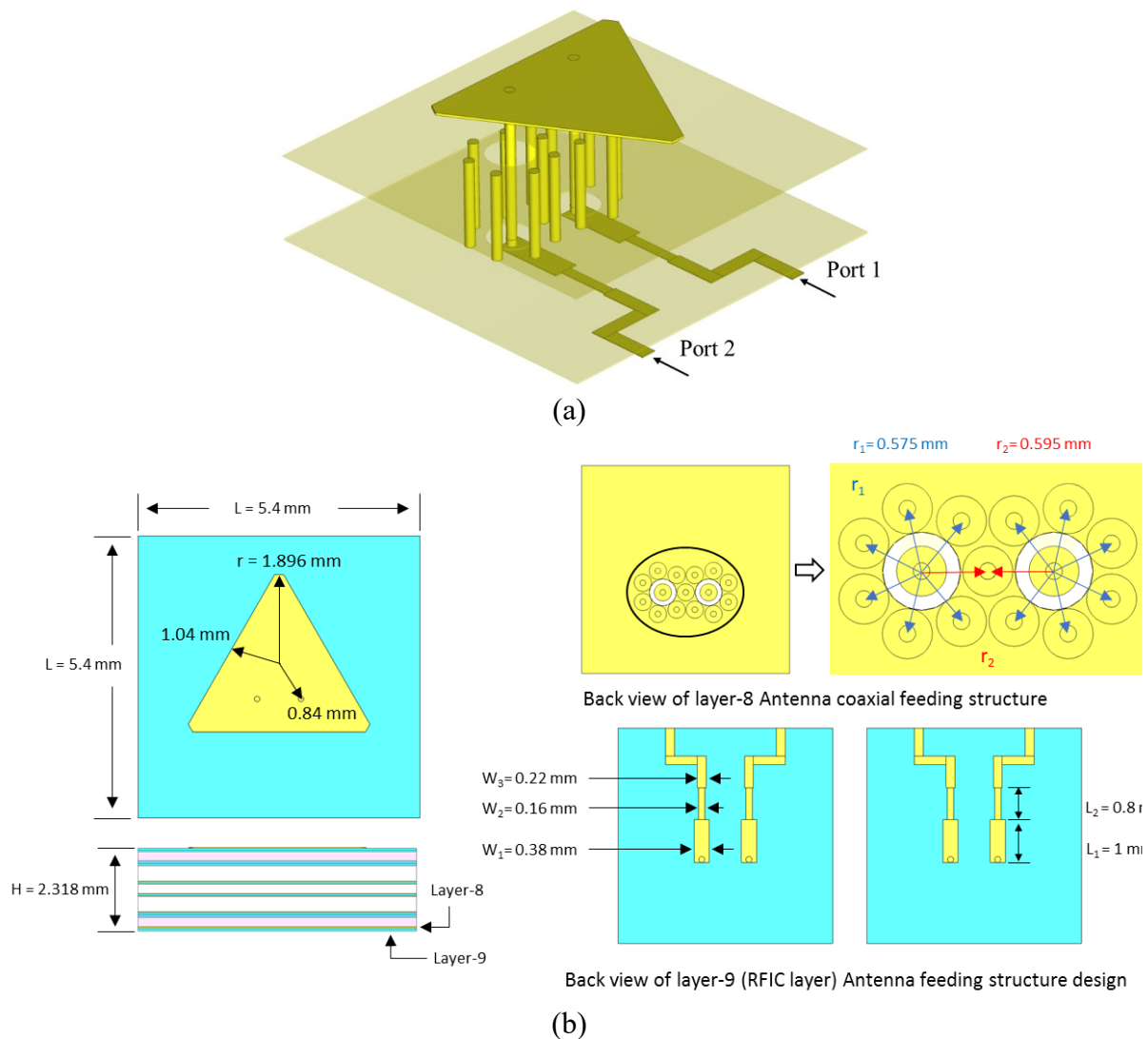


Figure 72. Transmit bevelled triangular patch antenna element and coaxial feeding design. Shows (a) perspective view with port allocation and (b) detailed top, side and back views.

The design of the transmit antenna element and its feeding network is presented in Figure 72. Again, the same PCB layer stack presented in Figure 46 is utilised here so as to match the receive antenna design. The triangular antenna design here has a minimal distance from the centre of 1.04 mm and a bevelled radius of 1.9 mm. A shared coaxial feeding structure and transform network is also utilised here.

The reflection coefficient and isolation of this design is presented in Figure 73. Here the reflection coefficient remains below -13 dB, and the isolation remains below -20 dB for the required bandwidth. Much like the split aperture antenna design, the transmit element has a far greater bandwidth due to the increased electrical substrate height. Figure 74 displays the radiation pattern of the transmit triangular antenna in RHCP mode. Here the antenna element pattern remains largely consistent over the bandwidth. There is a small amount of tilt in the antenna due to the large substrate height and the cross and co-polar isolation increase to 8 dB at the highest frequency and angles. However, the sequential rotation implemented in the array will counteract the tilt of the element beam and improve the overall axial ratio of the array.

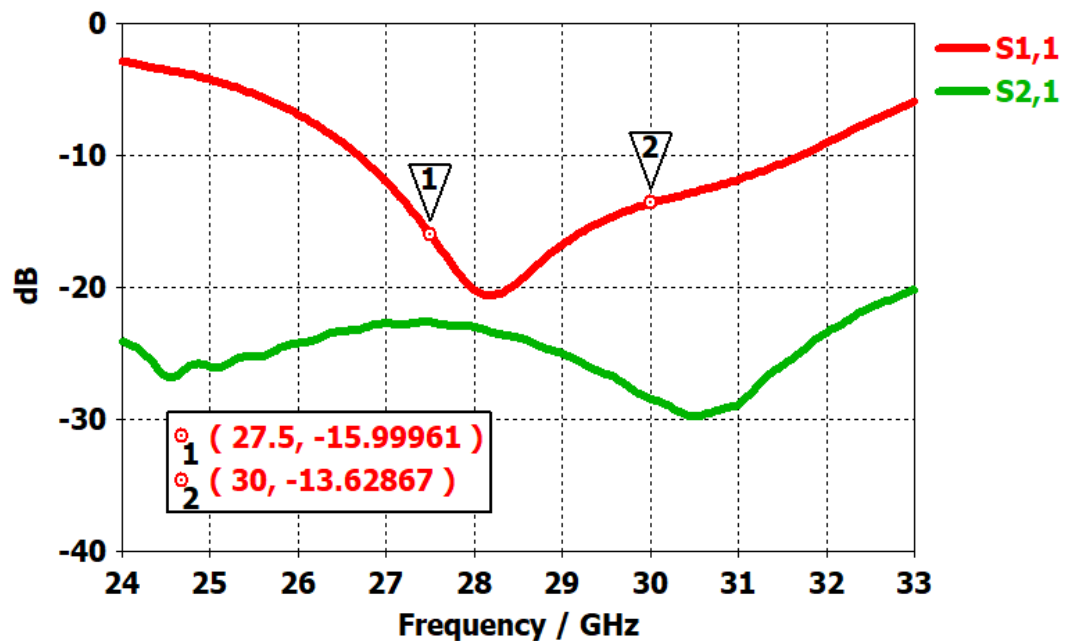


Figure 73. Reflection coefficient and isolation of the Rx bevelled triangular patch antenna element.

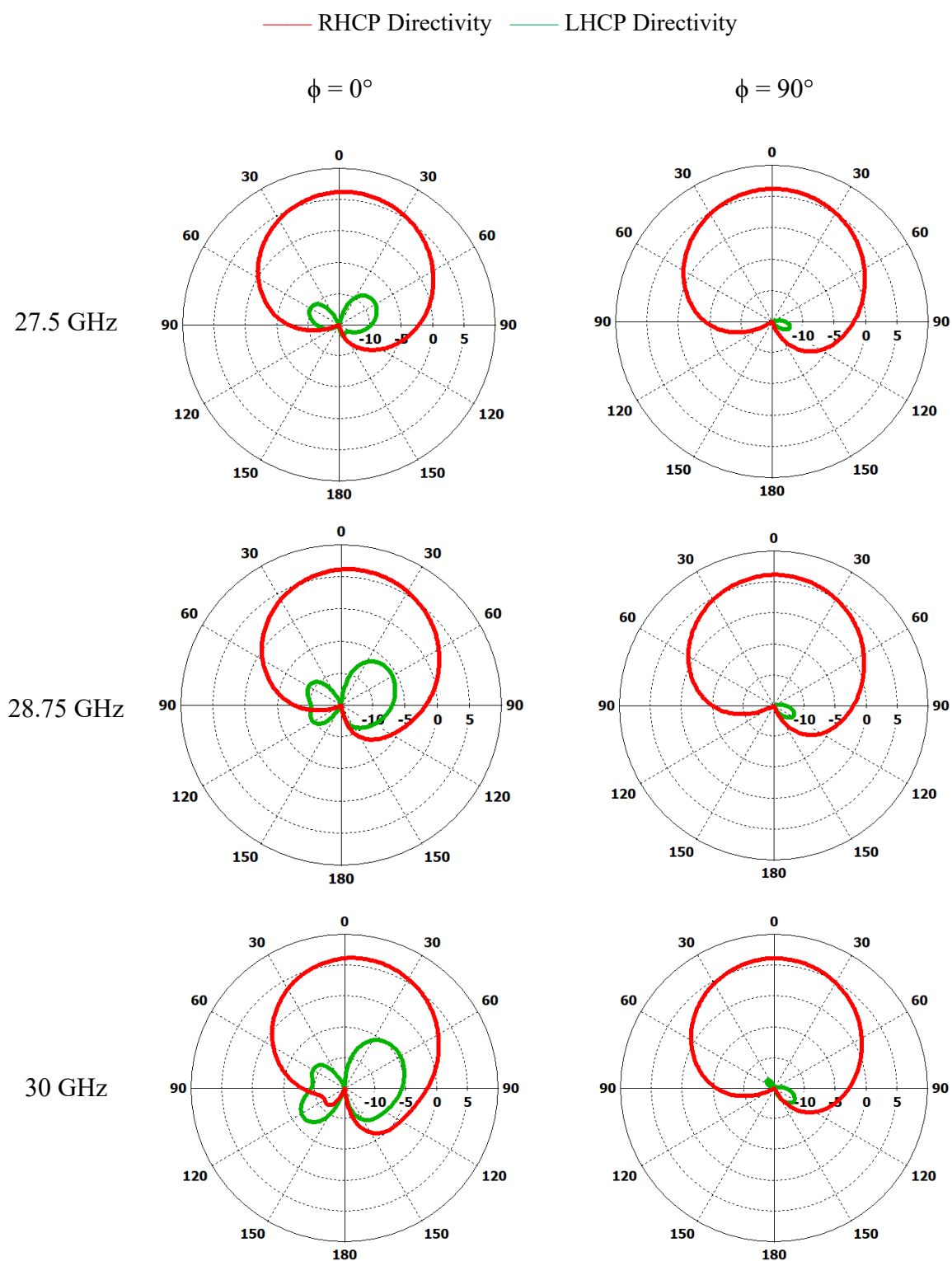


Figure 74. The radiation pattern of the Rx bevelled triangular patch antenna element in RHCP mode where both ports are excited with a 90° phase difference.

4.6.3 Shared Aperture Antenna Array Design

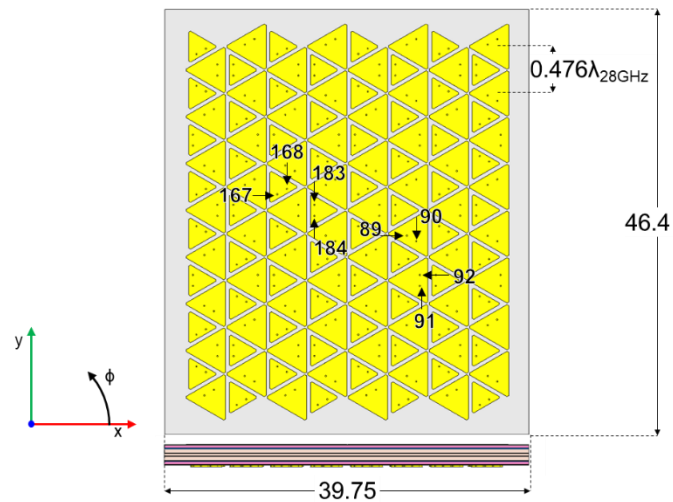


Figure 75. Shared aperture antenna array design. Units in mm.

A shared aperture antenna array utilising the triangular elements presented in the previous sections for optimal tessellation has been designed and is presented in Figure 75. This design uses interpolation of a receive and transmit sub-array to provide a single shared aperture with an Rx to Tx ratio of 1:1. Here, by simulating a series of 6x6 arrays at different interelement distances, the optimal interelement distance for the array (and hence, both sub-arrays) was found to be 5.10 mm. This results in a relative distance of $0.33\lambda_{19.5\text{GHz}}$ and $0.476\lambda_{28\text{GHz}}$. Such a distance is far closer that would normally be considered optimal for the Rx sub-array. As a result, the Rx sub-array has a lower gain than that of the Tx sub-array. The key reason for selecting this distance was to reduce grating lobes specifically in the Tx sub-array as maintaining low grating lobes is vital to meet the required radiation masks for satellite communication. This variation in gain is not inherently an issue for this application however as, at high frequencies, higher gain is required in order to counter increased free-space loss.

4.7 Shared Aperture Antenna Array Simulated Results

4.7.1 Receive Sub-Array

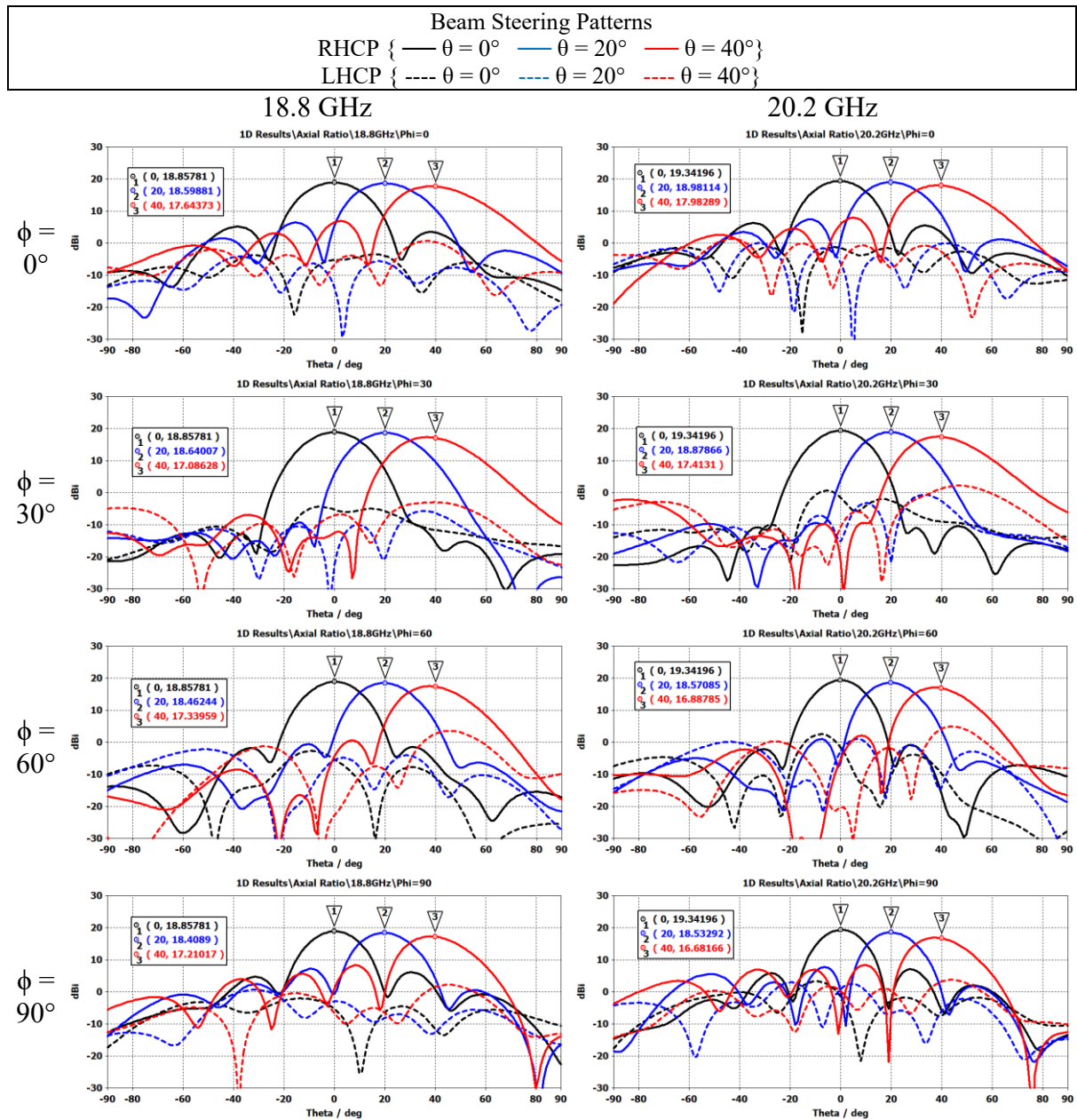


Figure 76. Beamforming of the Rx antenna array in RHCP mode across the operational bandwidth.

Much like the split aperture antenna array simulation, the s-parameters cannot be calculated as the matching network cannot be included in the large-scale simulation. However, accurate directivity can be calculated. The beam steering performance of the receive sub-array is demonstrated in Figure 76. Here beam steering across the targeted bandwidth to $\theta = \pm 40^\circ$

from the boresight direction is demonstrated. Grating lobes remain below -10 dB except at extreme steering angles and frequencies. Here, the grating lobe increase to -7 dB at 20.2 GHz in the plane of $\phi = 90^\circ$ when steering to $\theta = \pm 40^\circ$. The axial ratio remains below 3 dB at all scanning angles.

4.7.2 Transmit Sub-Array

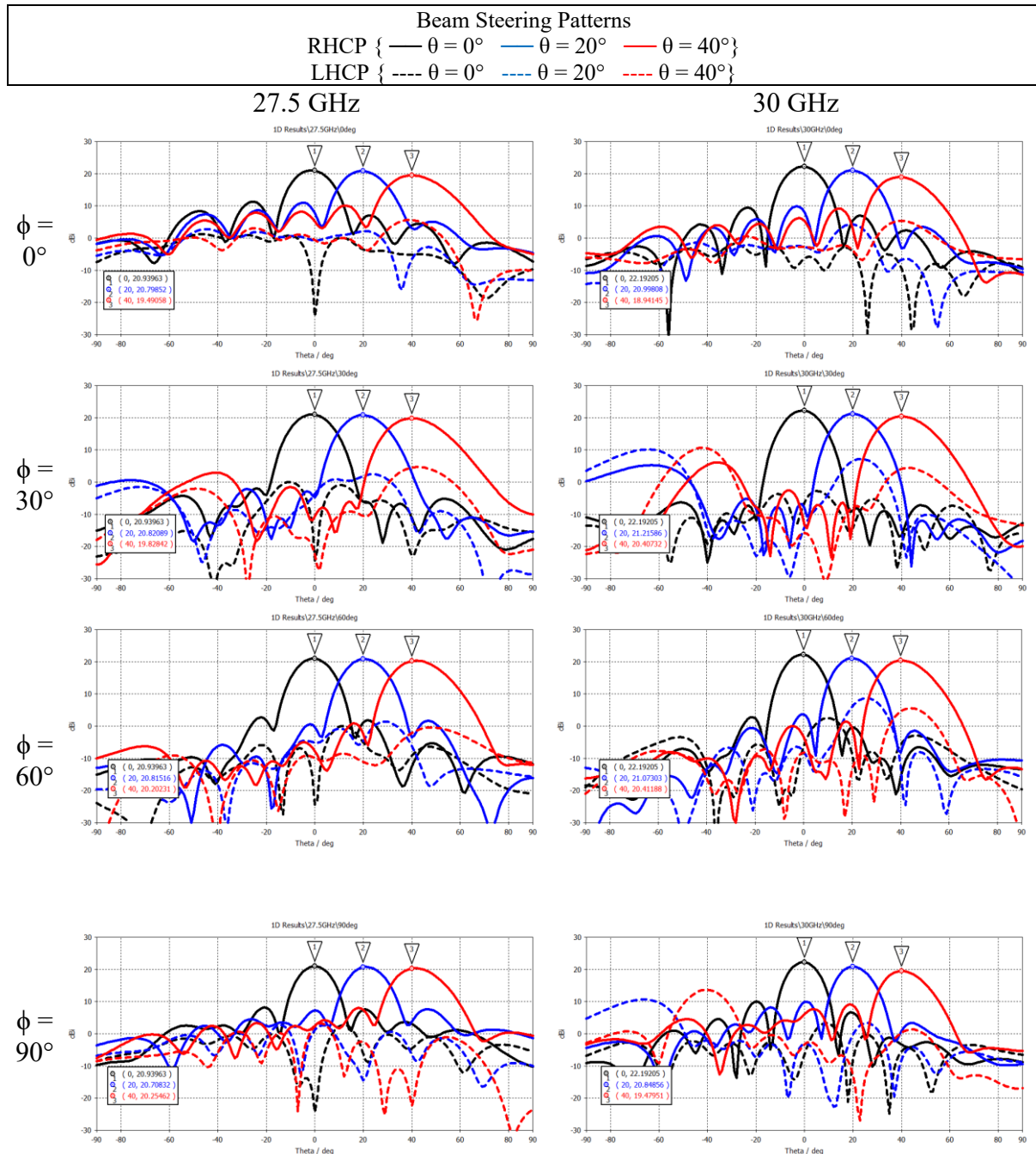


Figure 77. Beamforming of the Tx antenna array in RHCP mode across the operational bandwidth.

Figure 77 presents the beamforming capability of the transmit sub-array. It is demonstrated that the antenna array is able to provide beam steering to $\theta = \pm 40^\circ$. Much like the receive sub-array, grating lobes are generally good except for at 30GHz where the LHCP grating lobe level increases to -7 dB at $\theta = \pm 40^\circ$. However, here only phase shifting is applied to steer the beam. If amplitude tapering were applied across the array, it is very likely that this grating lobe could be reduced further.

4.8 Discussion

Table 4. Comparison between the split aperture antenna array and shared aperture antenna array.

	Split Aperture		Shared Aperture	
	Rx	Tx	Rx	Tx
Percentage Bandwidth	8.9%	16.9%	8.2%	17.1%
Size (8x8)	Rx [60mm x 72mm] + Tx [41mm x 49mm]		Combined [40mm x 46mm]	
Axial Ratio	< 3.3 dB		< 3 dB	
Gain in broadside direction (centre frequency)	22.8 dBi	22.8 dBi	19.1 dBi	21.6 dBi
Minimum Gain (at maximum steering)	20.4 dBi	20.4 dBi	16.7 dBi	18.9 dBi
Scanning Range	$-50^\circ < \theta < 50^\circ$		$-40^\circ < \theta < 40^\circ$	

In this chapter, two split aperture antenna arrays have been developed to cover a receive frequency of 18.8 GHz to 20.2 GHz and a transmit frequency of 27.5 GHz to 30 GHz. In simulation it was demonstrated that both these arrays provide beam steering of $-50^\circ < \theta < 50^\circ$ from the boresight direction across the operational bandwidth with grating lobe levels of less than -10 dB and an axial ratio of less than 3 dB. A prototype of a receive and transmit array with selected excitation ports was then developed and fabricated to validate the accuracy of the simulation and manufacture. It was demonstrated that the beam patterns of each antenna element port were accurate to the simulations. The reflection coefficient of the measured transmit elements also closely matched the simulated results. A small shift in frequency was

noticed in the measured reflection coefficient, however this can be corrected using further optimisation of the antenna design or calibration of the system.

A novel shared aperture antenna array has then been developed using triangular elements in a triangular lattice with sequential rotation. The size of the shared aperture array is far smaller (2.5 times smaller) than that of the split aperture array design. However, the scanning range of the array is slightly limited due to the increased grating lobes caused by mutual coupling between closely packed elements. Further, in order to improve steering performance and maintain a 1:1 Rx to Tx ratio, the element spacing of the shared aperture topology has been reduced. As a result, the gain of the array is also reduced. This has a greater impact on the Rx sub-array than the Tx sub-array given the change in electrical distance over frequency. However, this variation in gain between the receive and transmit sub-array, can be beneficial to countering the impact of free space path loss.

Table 5 presents a direct comparison between the split aperture antenna array design and the shared aperture antenna array design. While there are some limitations relative to the split aperture array also presented here, there are still clear benefits in the shared aperture design. Firstly, as the structure is highly compact compared to the split aperture structure, it is ideal for integration in vehicles, UAVs and other space limited applications. Secondly, as this design uses a repeatable tile structure with a 1:1 ratio of receive and transmit elements, it is ideal for optimal integration with RFICs with an equal number of Rx and Tx channels. Both of these advantages also translate to a significant cost benefit primarily related to the number of components required for the system

The primary focus of the current work is on the development of the array topology concept, and incorporation with the PCB and bandwidth requirements. However, there are some methods that could be implemented to further improve the performance such as via structures and multi-layer antennas to improve gain and steering performance; and amplitude

tapering for grating lobe reduction. These methods could be investigated in future work for which this work provides a clear baseline of optimisation and performance.

Compared to the existing cutting-edge systems reviewed at the start of this section, this work provides some clear benefits and novelties. Firstly, this system is built on a single PCB that allows for an overall very low profile of less than 3 mm in height. This is far lower than ALL.SPACE's lens base approach [56] and still lower than slot fed approach presented by Starlink [48]. A terminal with a large height will increase air resistance, a serious issue especially for modern electric vehicles. Large terminals can also be difficult to certify from a safety perspective as it could have an impact to passenger safety in the case of a vehicle rolling. It also becomes very difficult to seamlessly integrate such designs into vehicles without an unsightly hump on the roof. While this may not be a technical issue, vehicle manufacturers need to ensure their vehicles are attractive to the consumer. The system presented here matches Amazon's project Kuiper system [54] in frequency but innovates to two key aspects. Firstly, this system places antenna elements on a single top layer, greatly reducing the complexity of the system and reducing inefficiencies caused dielectric losses above the antennas. Secondly, the system presented here provides reconfigurable circular polarisation, unlike the single polarisation mode used in [54]. Reconfigurable polarisation allows for greater compatibility with LEO systems and allows for optimal use of spectrum by using polarisation to reduce interference.

Chapter 5.

Wideband 5G Antenna Array for Air-to-Ground Communication

So far, this work has been focused on developing arrays for user terminals on or integrated into ground vehicles for satellite communication. Many of the challenges faced ground-to-space LEO communication (such as beam steering and aerodynamics) are common with those of ground-to-air 5G systems. However, unlike LEO communication, the 5G spectrum is fragmented globally and therefore requires a very wideband system capable of adapting to all regions in a single system. While 5G mobile phones are now common, many only provide access for the region of sale. However, for aircraft such as planes and UAVs which move across regions regularly, communication cannot be region locked. As will be detailed here, no existing system is able to achieve the required wideband functionality and beamforming capability while maintaining a low profile suitable for easy integration in such aircraft.

This chapter will review these challenges and investigate existing solutions. Then, a proposed solution is presented alongside simulation and measurements that provides complete coverage of the mid-band 5G spectrum with $\theta = \pm 40^\circ$ beamforming in a low profile design. This is then compared to existing work and found to provide significant benefits.

5.1 Ground-to-Air Requirements and Challenges

Internet access is currently delivered to aircraft via air-to-ground and satellite hybrid networks such as the European Aviation Network [5]. However, such networks provide limited data rates of up to 50 Mbps, which needs to be shared between all passengers and essential aircraft communication. By implementing 5G in place of these LTE networks, data rates and latency can be improved by an order of magnitude [60]. Not only does this enable faster streaming and communication for passengers, but it also allows for live data transfer between the aircraft systems and ground services. Such data will enable live remote analysis on the cloud to improve the efficiency, safety, and cost of air travel [61], [62], [63]. Furthermore, this data can be sold to third parties for activities such as climate and meteorological research. Unmanned Aerial Vehicles (UAVs) and drones can similarly benefit from wideband 5G coverage, as it will enable autonomous drones that can operate cross-border in any region of the world [64].

There are several technical requirements in relation to the antenna performance and design that need to be addressed to ensure optimal integration and necessary performance:

Size and complexity are a priority in antenna design targeting commercial rollout in aircraft. A large design will increase drag and thus an aircraft's fuel costs or make it impossible integrate the antenna all together (especially in the cases of UAVs). Hence, attention must be paid to the SWaP-C (Size, Weight, Power and Cost) factor of the design in order ensure it is suitable for productization. The complexity of the antenna design can also impact the cost of manufacture and the cost of the RF network.

Wideband capability is also a key technical requirement. While 5G has been predominantly standardized, the frequencies licensed in each region differ (e.g., 3.4 - 3.8 GHz in the EU and 3.7 - 5 GHz in the USA) [4]. As such, in order to cover 5G globally with a single system, a bandwidth from 3.3 GHz to 5 GHz [65] at a minimum is required for mid-band 5G,

even though only approximately 0.4 GHz bandwidth is necessary in any one location and its corresponding band.

Like all 5G systems, high gain beamforming is also necessary in order to effectively receive and transmit high speed communication over long distances. It is therefore required for air-to-ground communication that beamforming of $\theta = \pm 40^\circ$ is possible for all azimuth angles.

5.2 Existing Work

5.2.1 Antenna Elements

Existing single element designs such as slotted patches [66], [67], [68], can provide reasonable bandwidth (<35%), and more complex topologies such as spiral antennas [69], [37] & [70], using a traveling wave model, can offer even greater bandwidth coverage (>50%). The designs of these slotted patches and spiral antennas are presented in Figure 78 to Figure 82.

Table 5 displays the key performance characteristics of these antennas for this application.

Table 5. Existing wideband patch antennas and spiral antennas, including information about the bandwidth and pattern of each antenna.

	[66]	[67]	[68]	[37]	[71]
Bandwidth	30%	25%	145%	27%	100%
Mono-Directional?	Yes	Yes	No	Yes	Yes
Consistent Pattern Over Freq'?	Yes	N/A	Yes	N/A	No
Height	$0.09\lambda_{\max}$	$0.01\lambda_{\max}$	$0.06\lambda_{\max}$	$0.07\lambda_{\max}$	$0.21\lambda_{\max}$
Antenna Size	$0.4 \times 0.56\lambda_{\max}$	$0.34 \times 0.44\lambda_{\max}$	$D = 0.55\lambda_{\max}$	$0.51 \times 0.448\lambda_{\max}$	$D = 2.4\lambda_{\max}$

The E-shaped antenna in Figure 78 provides a good bandwidth of 30% and maintains an axial beam that remains mostly consistent across the bandwidth of the antenna. Further, this antenna maintains a height of less than $0.1\lambda_{\max}$. However, this antenna relies on an airgap between the antenna and substrate, and so lacks the mechanical rigidity of a solid dielectric

material. However, by moving to a higher dielectric material, the overall bandwidth of this antenna would be reduced significantly. Further, the low permittivity of air has also resulted in a larger antenna with a length of $0.56\lambda_{\max}$. This size is clearly unsuitable for antenna array where the optimal distance between elements is typically around 0.5λ . Even if the antenna elements were brought close to the optimal distance, the mutual coupling between elements would be significant.

Variations of E-shaped antennas such as half E-shaped antennas [67] (Figure 37) have been able to reduce the length of these antennas by 20-30%, but not sufficiently to be suitable for a useful array geometry for this application. For both these cases the size could be reduced further by increased the permittivity of the substrate, but at the cost of a greatly reduced antenna bandwidth.

The slotted patch antenna [47] provides a very wide bandwidth of 145%, achieved by placing a slot in the antenna patch and removing the reflector plane under the antenna, as shown in Figure 80. However, once the reflector plane is removed, the antenna will radiate with an omnidirectional pattern. Such a pattern is unsuitable for beamforming, as a back lobe in the array pattern will always be present.

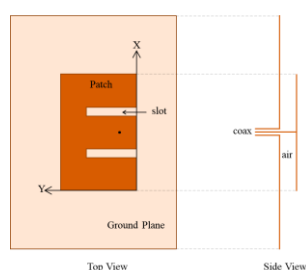


Figure 78. E-Shaped Antenna Presented in [66].

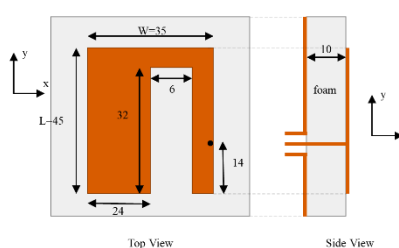


Figure 79. Half E-Shaped Antenna Presented in [67]

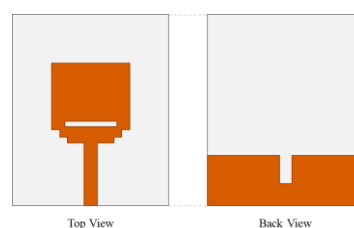


Figure 80. Slotted Patch Antenna presented in [68].

Spiral antennas are an alternative to slotted patch antennas that can provide directional wideband performance. Patch antennas utilise a resonance mechanism for resonance, meaning that the bandwidth of patch antennas is usually quite limited. Conversely, spiral antennas utilise

a traveling wave mechanism for radiation, where the excitation travels along the length of the microstrip instead of simply resonating. As a result, there will be an active region of the spiral antenna that will change radius with frequency and allows for wideband performance.

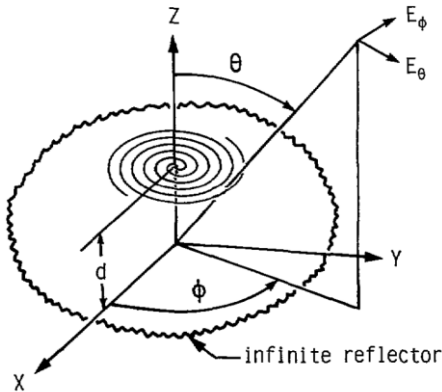


Figure 81. A reflector plane backed spiral antenna presented in [69].

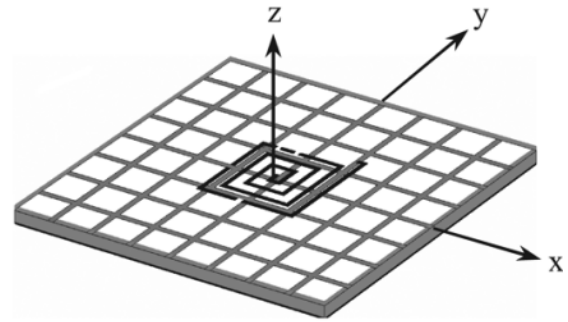


Figure 82. HIS-Based Spiral Antenna presented in [37].

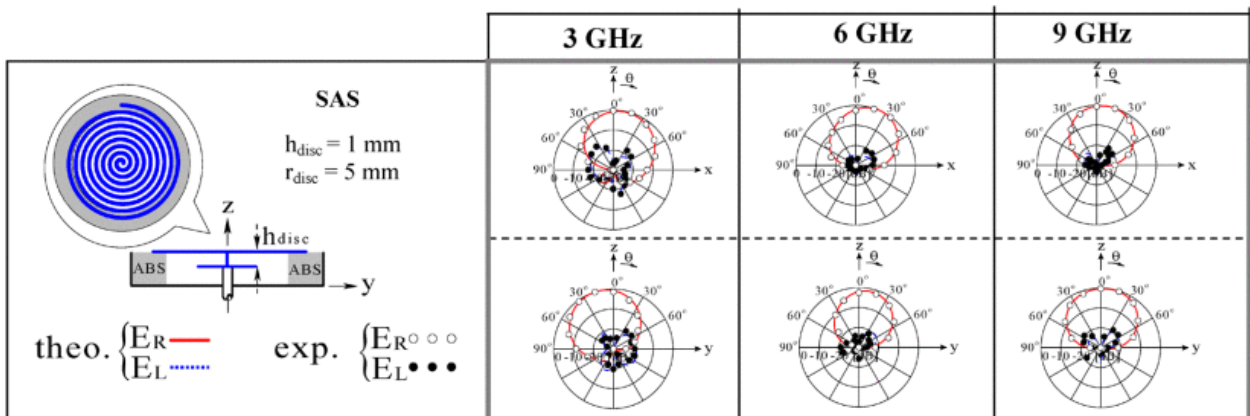


Figure 83. A low profile single arm spiral antenna presented in [71] and the variation in radiation pattern over its bandwidth.

The first spiral antenna backed by a reflector plane [69] is presented in Figure 40. This design demonstrated the wideband capability of such antennas, as well as the use of techniques to design such antennas. This initial design used an airgap and a high value of d . Since this first reflector backed spiral antenna design, numerous spiral antenna designs have been devised to improve performance such as [37]. In [37] a High Impedance Surface (HIS) has been added

within the dielectric substrate. This allows the spiral to be far lower profile, although with some sacrifice in bandwidth. It is not clear how the pattern changes over frequency, however this is a minor issue as open circuit switches were also used to enable pattern reconfigurability in spite of any pattern change.

In [71] a spiral antenna has been developed that, considering its low profile, has a very large percentage bandwidth of 100%. Its design is shown in Figure 83, alongside the resulting radiation patterns of the antenna over the frequency range. It is clear how the change in frequency can impact the tilt of the antenna pattern, particularly at 3 GHz and 6 GHz where the beam is tilted by between 10° to 30° from the boresight direction. This occurs because the phase distribution across the antenna itself can cause interference in free space such that the beam tilts. As a result, such an antenna design is unsuitable for antenna array implementation.

As shown, the radiation pattern direction can vary drastically across the operational bandwidth. This is acceptable for many applications and has been successfully exploited for many switch beam steering topologies [72] [73] [74]. Alas, for applications such as 5G and LEO satellite communication where array beam steering is required, such variation in unit element beam pattern will heavily restrict the beam steering capabilities of the array. Additionally, wideband beamforming performance will always be impacted by the physical geometry of the array structure, as the optimal element distance will change with frequency. Careful optimization of the array geometry is therefore required to ensure consistent gain and steering performance across the bandwidth. It is for these reasons that there are currently no documented planar spiral antenna arrays capable of providing the wideband beam steering performance presented in this work, while maintaining a low-profile design that the author is aware of.

5.2.2 Wideband Antenna Arrays



Figure 84. A 1x4 Array of Wideband Dual-Circularly Polarised Antennas as presented in [75].

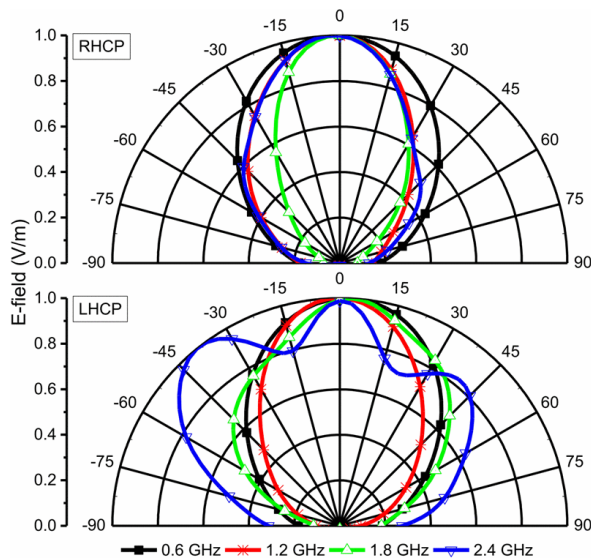


Figure 85. Radiation patterns of the antenna element presented in [75] over the bandwidth of the antenna.

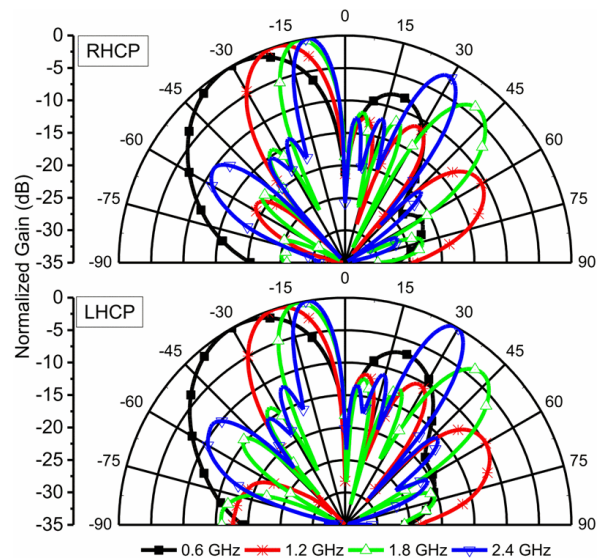


Figure 86. Radiation patterns of the antenna array presented in [75] over the bandwidth of the antenna when a phase shift of $\Delta\beta = 90^\circ$ is applied.

Some topologies of spiral antenna arrays have been developed that are capable of providing a wide operating bandwidth [75], [76]. However, they lack suitable beam steering due to the large element size and variation of unit element radiation pattern over frequency. A wideband spiral antenna phased array designed by H.R. Fang [75] demonstrates the challenges mentioned previously and emphasizes that beam steering performance is affected by the variation in unit beam pattern over the operational bandwidth. The design of the array presented

in [75] is shown in Figure 84. The radiation performance of this unit element design in Figure 85 shows significant variation in the LHCP performance over the operational bandwidth.

As mentioned earlier, the array pattern is also impacted by the distance between array elements. As the unit element in the Fang's work [75] is far larger than $\lambda/2$ for most of the operational band, the electrical antenna array distance will be inherently very large at higher frequencies. It is seen in Figure 86 that this arrays beamforming performance is at its best at 1.2 GHz. At this frequency the array can steer to -18° with a grating lobe level of -10 dB. At a lower frequency of 0.6 GHz, the performance appears to be similar. As the inter-element phase remains at $\Delta\beta = 90^\circ$ across the bandwidth, at this frequency the beam steers to a lower angle of $\theta = -30^\circ$ and hence the grating lobe level increases to about -7 dB. Given the increase in beam angle, it is expected that the grating lobe level would reduce to under -10 dB when the beam is steered to $\theta = -18^\circ$. However, at frequencies above 1.2 GHz the performance of the array diminishes significantly. At 1.8 GHz and 2.4 GHz the grating lobe increases to -4 dB and 0 dB respectively. This increase is despite the natural decrease in steering angle. No data is presented for a $\Delta\beta = -90^\circ$ pattern, so the symmetry of the beam steering performance cannot be fully verified, a concern given the a-symmetry of the LHCP unit element pattern. Overall, this design is fundamentally limited by the size of the antenna elements, and its narrow steering range is therefore unsuitable for most beamforming applications.

The design in [76] provides similar performance to that of [75]. Here 69% bandwidth is achieved with a dual arm curl element of width $0.5\lambda_{\max}$. Unfortunately, beam steering performance of the array with grating lobe levels is presented only at a single, undisclosed frequency. The radiation patterns, shown here in Figure 89, displays the radiation pattern targeting $\pm 30^\circ$ with a grating lobe of approximately -6.5 dB. Again, much like [75], this performance is unsuitable for most beam steering applications. Further, in both Fang's design

[75] and Hovsepian's design [76] the antenna requires a complex feeding structure/network that increases the cost of the system.

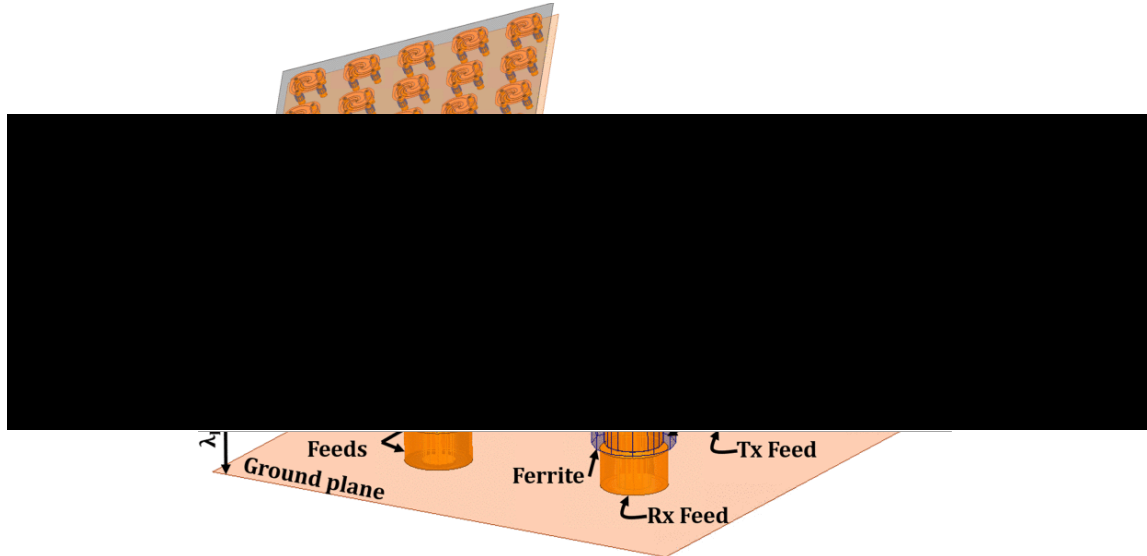


Figure 87. The array and antenna element design of the wideband four arm spiral antenna array presented in [76].

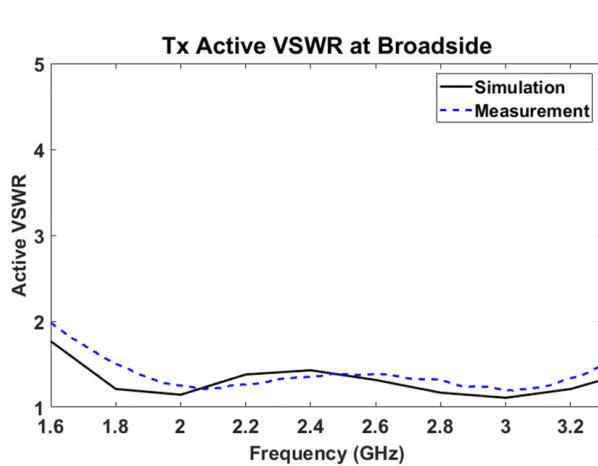


Figure 88. Active VSWR of the Tx antenna array presented in [76].

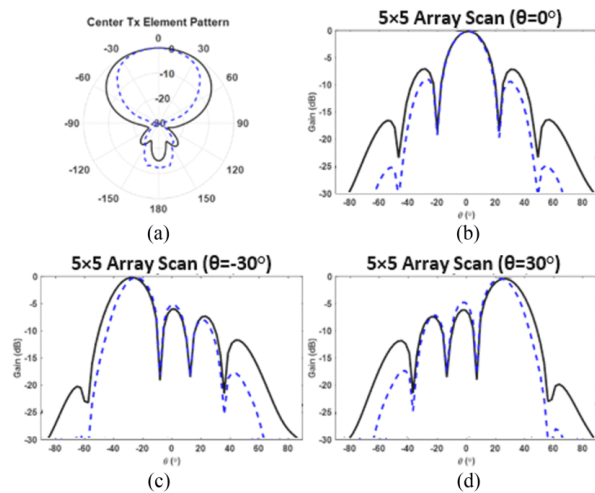


Figure 89. Transmit Element pattern and antenna array scanning performance of the array presented in [76].

Another wideband antenna array presented by Hinojosa Sáenz, I. D. [77] uses a simpler 2-arm spiral design (Figure 90) that is more compact than that of other existing designs [75] [76] and is therefore able to reduce the element spacing to less than 0.5λ . This antenna element

design provides 76% bandwidth, as displayed in Figure 91. Here, no beam steering has been demonstrated though the Relative Side Lobe Level (RSSL) for the boresight beam has been shown to be less than -10 dB across the bandwidth of the array (Figure 92). Here, to maintain the small antenna diameter and large bandwidth, a thick cavity structure ($0.35\lambda_{\max}$) has been required. Hence, the high drag area of the antenna structure means that even with the reasonable performance demonstrated in Hinostrza Sáenz's work [77], the design would be unsuitable for applications such as aerospace and UAVs. Such restrictions, similarly, pose system integration challenges in other new terrestrial high throughput applications such as high throughput Low Probability of Interception (LPI), which is presented as an application at the end of this chapter.

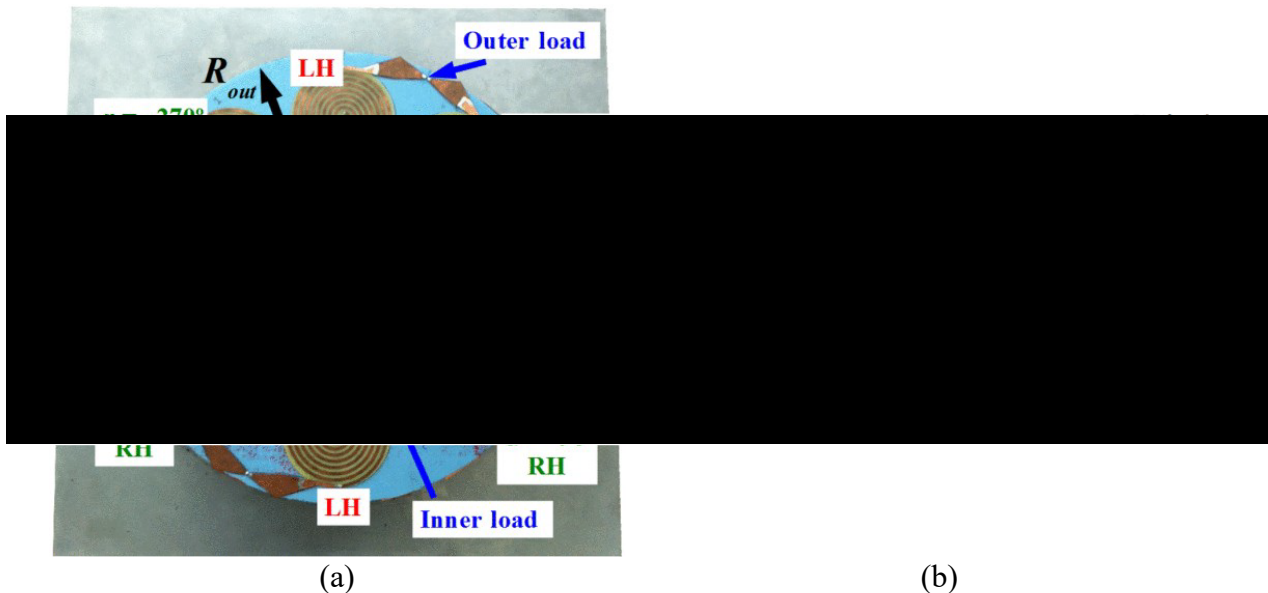


Figure 90. Ring antenna array prototype as presented in [77]. (a) Top view. (b) Side View.

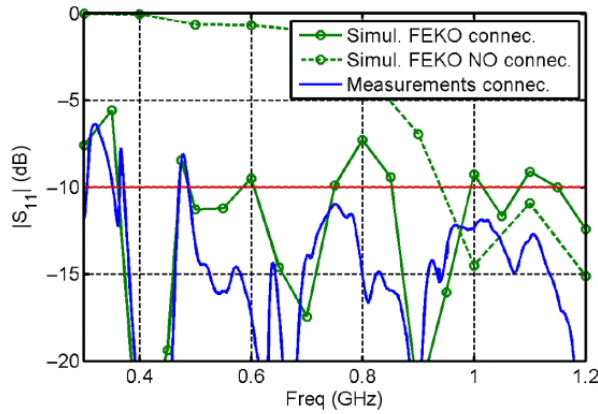


Figure 91. Simulated and measured reflection coefficient of the spiral antenna array presented in [77].

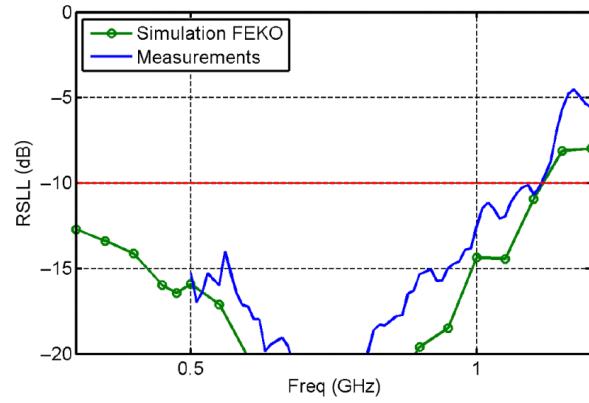
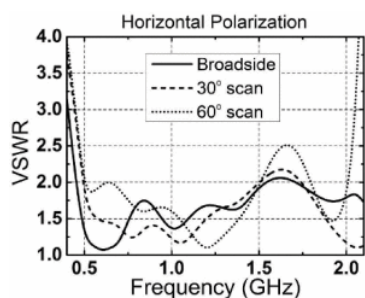


Figure 92. Simulated and measured Relative Side Lobe Level (RSL) of the antenna array when steering to presented in [77]

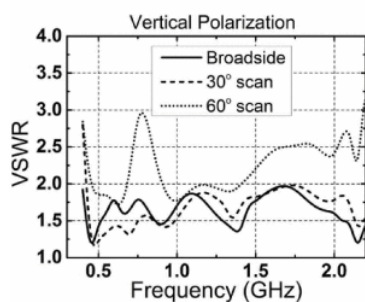
Dipole designs such as those presented by Hangyu Zhang [78] and Jian Xu Sun [79] prove very capable at delivering bandwidths greater than 120% with suitable beamforming capability for 5G applications. In Zhang's work [78] (Figure 93), a closely coupled vertical and horizontal dipole antenna with a parasitic superstrate layer is utilised to provide a bandwidth of 120%. The VSWR for the vertical and horizontal dipoles are displayed in Figure 94. Impressively, the beam steering performance of this antenna array remains consistent from 1 GHz – 2 GHz, as shown in Figure 95. Grating lobes and side lobes remain below -10 dB from the main lobe even down to beam steering angles of 60° . So far this design has only been demonstrated in a linear array so cannot perform azimuth beam steering. Were a 2D array implemented with even reduced scanning performance, then this array would be ideal for 5G systems. However, due to the large air gap below the dipoles and the large superstrate layer above them, the overall thickness of the antenna array has become $0.65\lambda_{\max}$. Much like previous antenna designs investigated here, these mechanical dimensions of the array unfortunately make it impractical for mobile and aviation use.



Figure 93. The (a) antenna element and (b) antenna array, presented in [78]

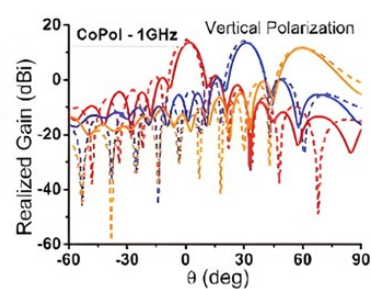
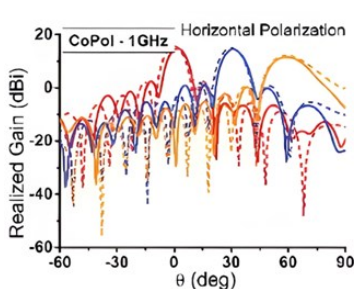


(a)

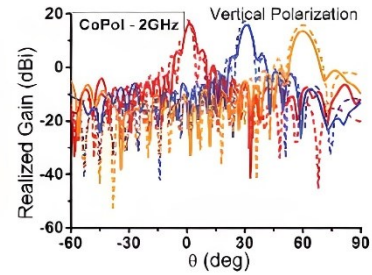
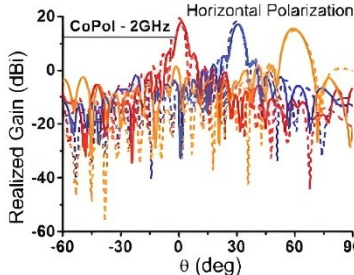


(b)

Figure 94. Simulated active VSWR in 0°, 30° and 60° scanning angles of the antenna presented in [78]. (a) Horizontal polarisation. (b) Vertical polarisation.



(a)



(b)

Figure 95. Measured Co-polarisation scanning performance of the antenna array presented in [78] at (a) 1 GHz and (b) 2 GHz.

Other dipole antenna array designs such as that presented in [79] have similar limitations. Here, the antenna design presented in Figure 96 uses tightly coupled dipoles and a meta-surface superstrate to provide a wide bandwidth antenna array. This antenna element design succeeds in providing a bandwidth of 127% (Figure 97). The authors of [79] presents only the realised gain of the central embedded element across a single phi cut (Figure 98). Here,

the authors assert that, as the cross-polarisation isolation, realised gain and active VSWR is suitable for beam angles of $\pm 60^\circ$ in the E-plane and $\pm 56^\circ$ in the H-plane, the beam steering performance of an array at these angles must also be suitable. However, this does not fully account for grating lobes that may occur as a result of mutual coupling between elements, particularly at the edge of the array. Assuming that the grating lobes do remain -10 dB from the main lobe for the stated beam steering angles then this array will provide suitable RF performance to that targeted in this chapter. Similarly, to [78] however, the air gap and superstrate in this design requires a large amount of spacing resulting in an overall height of $0.51\lambda_{\max}$. Again, this makes the design unsuitable for aviation integration

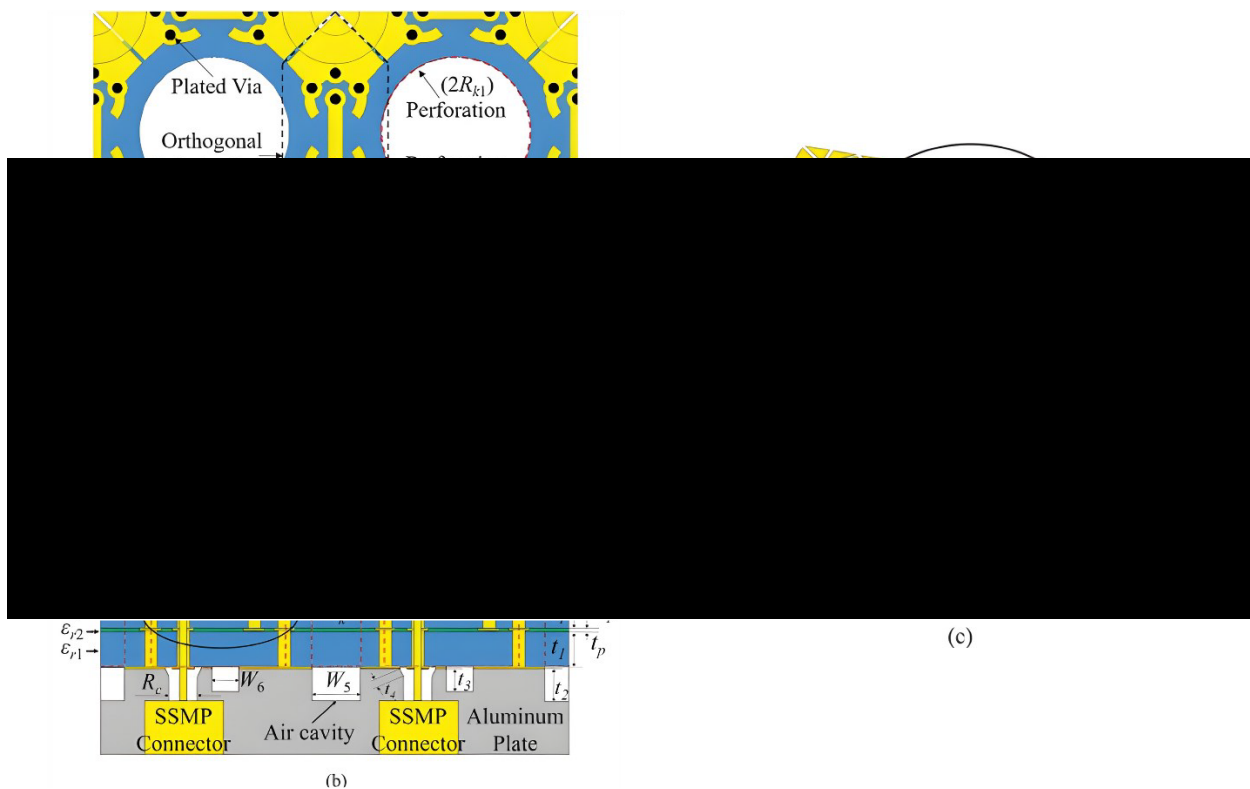


Figure 96. The configuration of the tightly coupled dipole array presented in [79]. (a) Top view of the dipole layer. (b) Array cross section. (c) Perspective view of the array excluding dielectric materials.

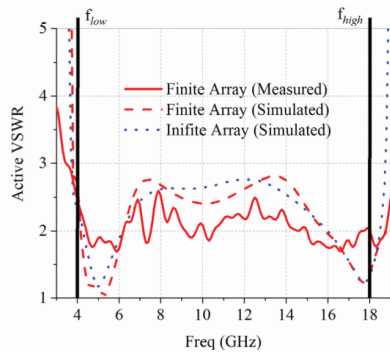


Figure 97. The active VSWR of the array presented in [79].

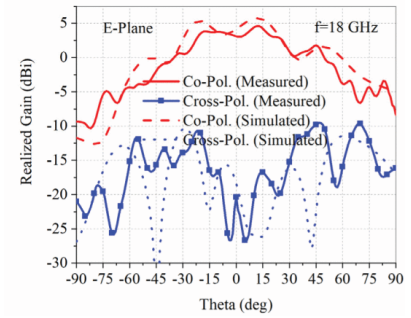
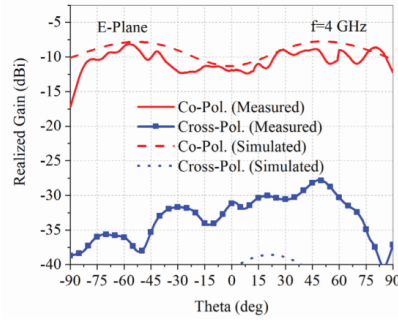


Figure 98. Realised gain pattern of the central element of the array at (a) 4GHz, and (b) 18 GHz. As presented in [79]. (No phi value is given but assumed to be $\phi = 0^\circ$).

In summary, of the state-of-the-art wideband antenna arrays reviewed here, there are key limiting factors that restrict their utility for aerospace 5G antennas. All of the antenna arrays presented are capable of providing wideband performance, often in excess of what is required for full mid-band 5G coverage. However, many struggle to achieve the required beam scanning performance over the full operational bandwidth. Of those that do, none are able to achieve it within a compact and low-profile design.

5.2.3 Proposed Solution

To solve these challenges, in the following section a low-profile ($<0.13\lambda_{\max}$), compressed spiral antenna array is presented with wideband functionality covering 3.3 – 5 GHz. Here, the optimisation process of this antenna is fully detailed, and the resultant element is placed in a 4x4 array prototype that is optimised with a triangular topology that provides exceptional scanning capability across the operational bandwidth. Here, measurements of this prototype are presented, analysed, and compared against existing works. With this further optimisation, this work is the first fully documented low profile wideband single-arm spiral antenna array with this level of beam steering performance. Crucial to this work, the spiral antenna element is compressed (spiral diameter $< 0.35\lambda_{\max}$), such that it provides an axial beam across all operational frequency bands. In summary, this design enables global mid-band

5G with a single, low profile antenna array. The antenna element design and optimization are detailed in section 5.3. In section 5.4 this proposed spiral antenna element is placed in a 4x4 triangular lattice array, enabling beam steering functionality. The array provides elevation steering of $-40^\circ \leq \theta \leq +40^\circ$ at all azimuth angles. The array has then been fabricated and its performance has been measured and analysed with a bespoke beamforming network.

5.3 Antenna Element Design

5.3.1 Antenna Element Structure

A wideband compressed spiral antenna element has been designed and fabricated, providing an axial beam at all target operating frequencies. These properties have been achieved in a low-cost low-profile ($<0.13\lambda_{5\text{GHz}}$) design. Figure 99 shows the geometry of the design. The antenna is constructed using a stratified structure of three layers. The antenna spiral pattern is milled onto a 1.5mm thick Rogers RO4350b substrate ($\epsilon_r = 3.48$ and $\delta = 0.0037$) at the top of the structure. Added below this is a thicker 4.59mm layer of Delrin plastic ($\epsilon_r = 2.6$ and $\delta = 0.005$). This layer is used as it is low-cost and easy to manufacture into a single thick layer, and its permittivity of $\epsilon_r = 2.6$ allows the antenna to be of a lower profile compared to an equivalent effective layer of air. Finally, a 1.6mm layer of FR-4 ($\epsilon_r = 4.8$ and $\delta = 0.025$) with a copper plating on its underside is used as a light-weight ground plane. The net height of the spiral antenna is $h = 7.69$ mm. An SMA connector is used to feed the spiral arm from the bottom of the antenna.

This Archimedean spiral antenna element has a radius of 10.2 mm and a strip width of 1.83 mm. The spiral element has been constructed using the Archimedean spiral equation:

$$r = a\phi$$

$$\text{where } \frac{\pi}{2} < \phi < T \times 2\pi$$

In this design, the spiral amplitude a has been set to 0.41 mm/rad and the number of turns T has been set to $T = 4.13$. This optimized geometry was achieved after several iterations to generate a stable pattern across a wide frequency band. These optimization iterations are presented in the following section.

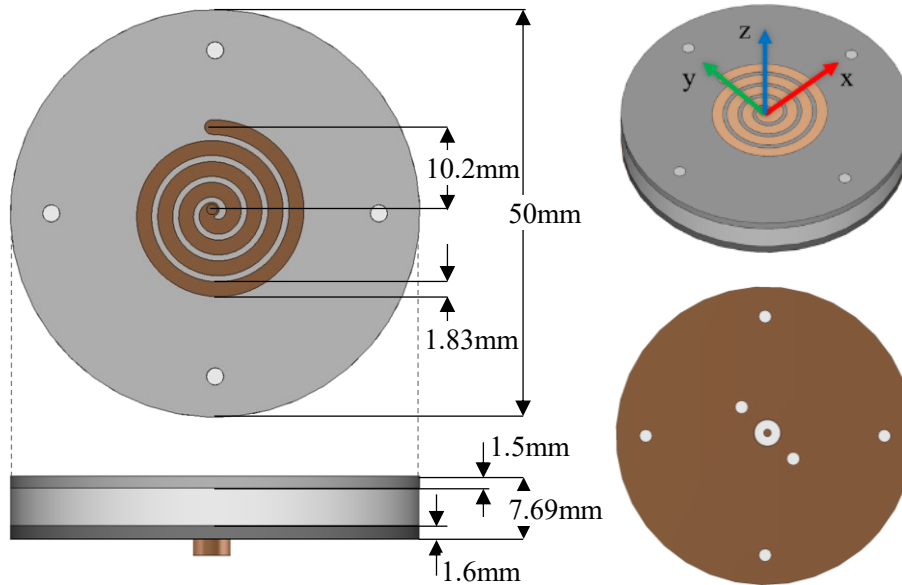


Figure 99. Compressed spiral antenna, its dimensions and top view and side view (left) alongside the perspective and bottom view (right).

5.3.2 Spiral Compression and Height Optimization

Compressing the spiral element is a key design feature that has enabled wideband coverage ($> 40\%$ bandwidth) whilst maintaining an axial beam. Figure 100 displays an orthographic radiation patterns of an optimized antenna design with a spiral amplitude of $a = 0.41$ mm/rad, a reduced amplitude of $a = 0.32$ mm/rad and an uncompressed amplitude of $a = 0.65$ mm/rad. For all of these variations, a constant ground plane diameter of 50 mm has been used. For a clear comparison, adjustments in the number of turns in the spiral and their orientation have been done to maintain a consistent central frequency of 4 GHz and a broadly close spiral arm end point. Specifically, for the case when $a = 0.32$ mm/rad, the number of turns

is increased to $T = 4.6$ and conversely, when the amplitude of the spiral is increased to $a = 0.65$ mm/rad, the number of turns is reduced to $T = 3.75$.

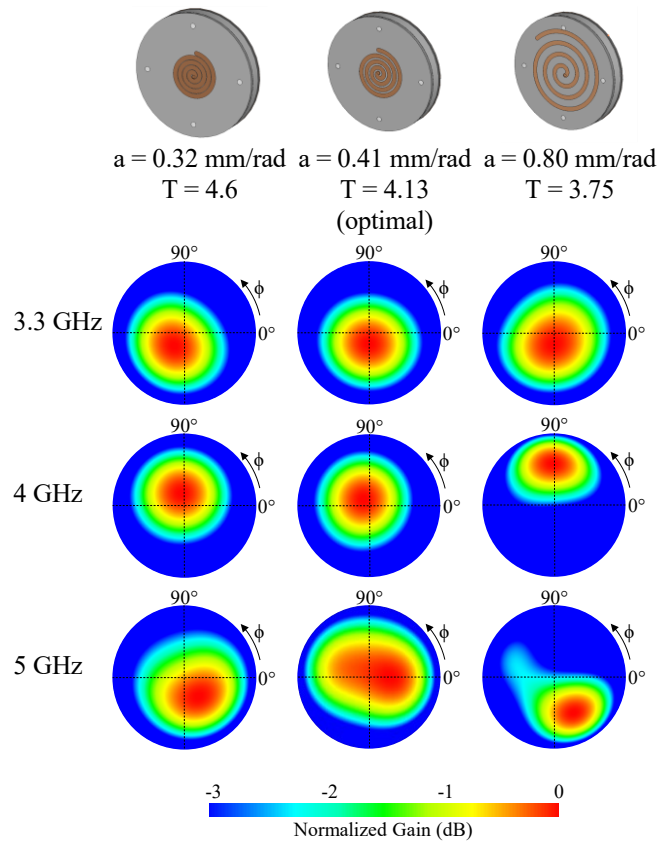


Figure 100. Orthographic radiation patterns of the compressed spiral antenna with a spiral amplitude of $a = 0.32$ mm/rad, $a = 0.41$ mm/rad, and $a = 0.6$ mm/rad across the frequency bandwidth. The optimal design ($a = 0.41$ mm/rad) shows minimal deviation from the broadside direction.

As can be seen in Figure 100, the selected optimal spiral configuration of $a = 0.41$ mm/rad produce a nearly constant axial beam across the band of interest. Both pre-optimal ($a = 0.32$ mm/rad) and post-optimal ($a = 0.65$ mm/rad) antenna designs have pattern deviation from the centre. This stable axial beam produced over the required bandwidth will significantly improve the steering performance in an array.

Further, it was found that the spiral amplitude and turn variations impacted the resultant reflection coefficient bandwidth. The reflection coefficients of these spiral amplitude variations are presented in Figure 101. Here it is shown that it is only the optimal design that is able to provide a bandwidth of 3.3 – 5.25 GHz, which exceeds our targeted applications. The most

compressed model ($a = 0.32$) has a limited bandwidth of 3.5 GHz to 4.8 GHz, and the uncompressed model provides a single bandwidth from 3.6 GHz to 4.8 GHz. Aside from the compression of the antenna, the thickness of the substrate is another central factor for the radiation pattern stability and is investigated next.

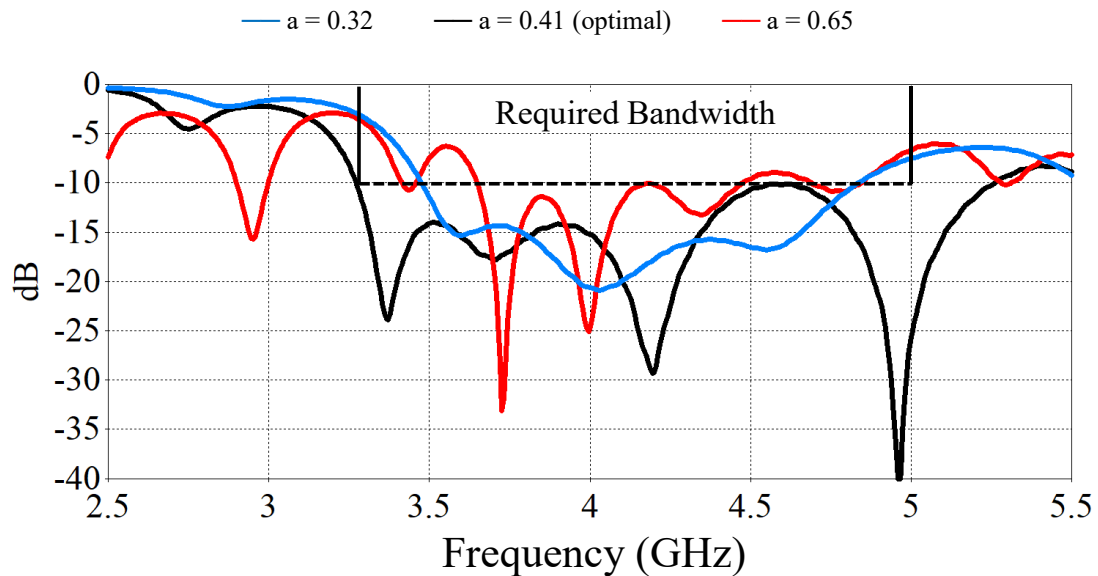


Figure 101. Reflection coefficients of the three-spiral antenna with spiral amplitudes of $a = 0.32$ mm/rad, $a = 0.41$ mm/rad and $a = 0.65$ mm/rad. Only the optimized model with amplitude $a = 0.41$ mm/rad provides the required bandwidth for the targeted application.

Figure 102 displays the change in radiation pattern of the optimal spiral as its substrate height is changed from 3.7 mm to 11.7 mm across the target frequency band. The unit pattern remains constant when the substrate is thin ($< 0.11\lambda_{\text{centre}}$), but it tilts away from the boresight at higher frequencies when the substrate thickness increases beyond $0.11\lambda_{\text{centre}}$. However, as with any planar antenna, the substrate thickness plays an important role in the antenna impedance bandwidth. This can be seen in Figure 103. Indeed, considering Figure 103, the height 7.7 mm provides the largest bandwidth and a stable axial radiation across the targeted band. Therefore, it was selected for the test design.

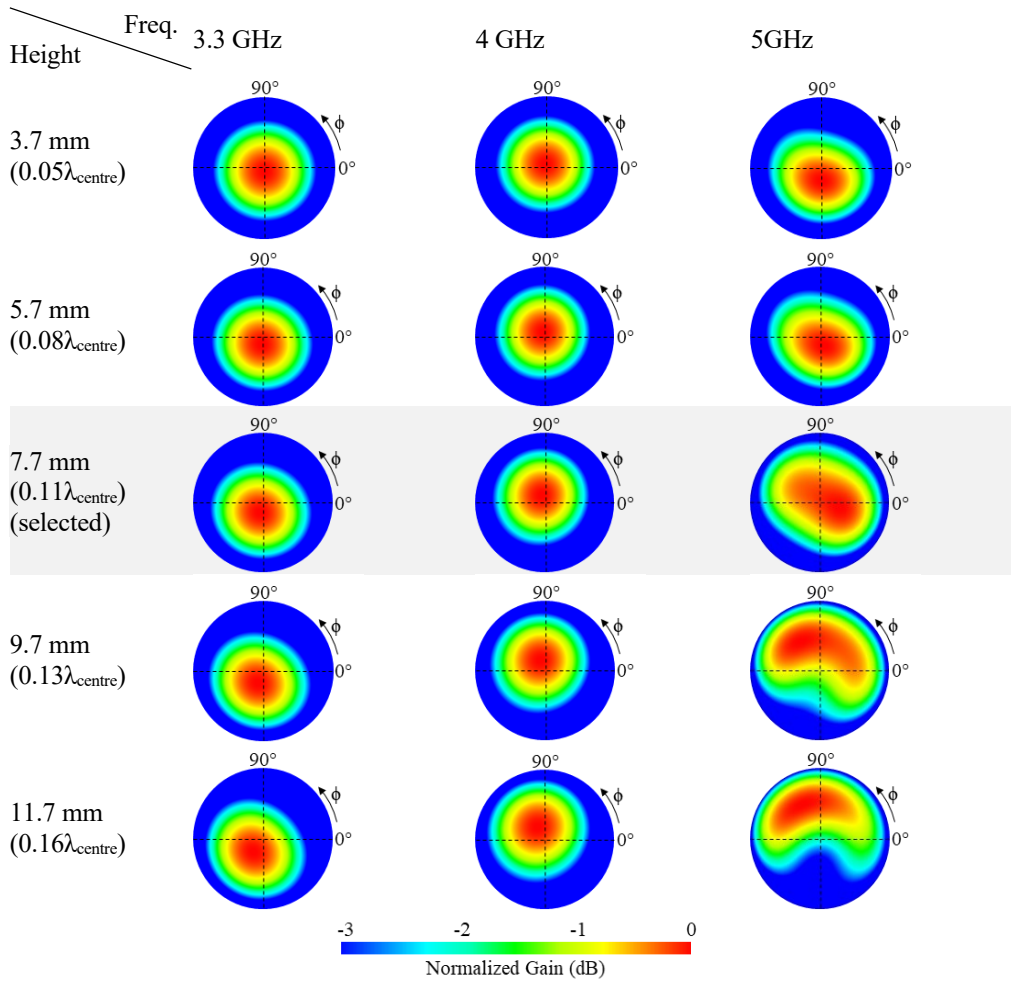


Figure 102. Orthographic radiation patterns of the optimal spiral antenna where the height of the substrate has been varied from 3.7 mm to 11.7 mm with a constant amplitude of $a = 0.41$ mm/rad and a number of turns of $T = 4.13$

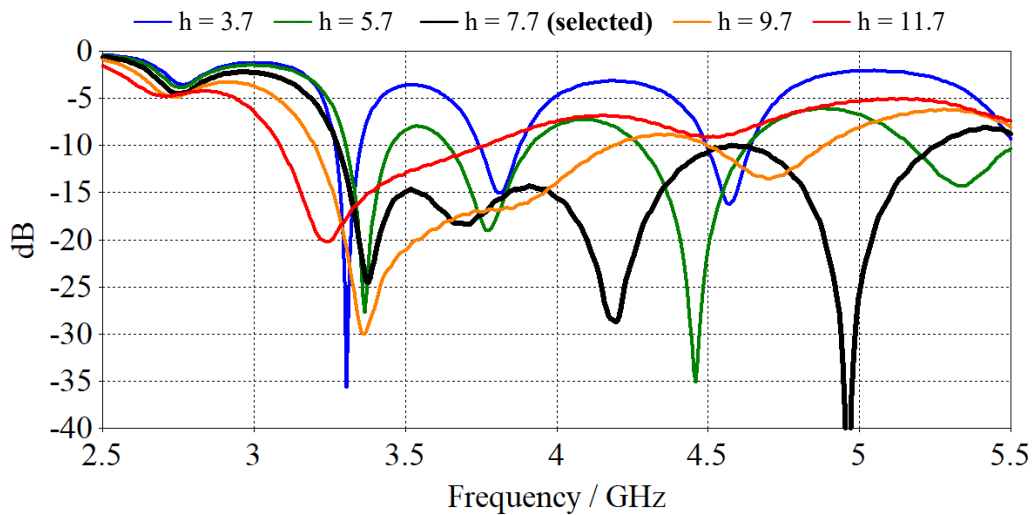


Figure 103. Reflection coefficients of the optimised spiral design with substrate height variation from $h = 3.7$ mm to $h = 11.7$ mm

5.3.3 Single-arm spiral simulation & experimental validation

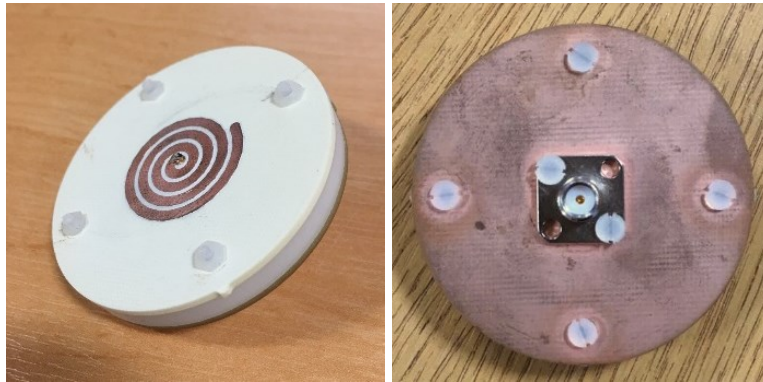


Figure 104. Prototype of compressed spiral antenna; left: front and right: back view.

A prototype of the optimal antenna element has been fabricated and measured (Figure 104). The simulated and measured reflection coefficients of the optimal antenna element are shown in Figure 105, which are in good agreement. The antenna has a reflection coefficient (S_{11}) bandwidth of 3.3 GHz to 5.25 GHz. The simulated S_{11} remains below -10 dB across the entire bandwidth. The measured results match this well, though increase slightly to -8.7 dB at 4.6 GHz. This could be due to fabrication errors and material tolerances, particularly in regard to the Delrin substrate which will have a higher level of variation in RF characteristics over specialist RF materials. This could be verified in future prototypes by specifically testing the materials and using high accuracy measurement devices to ensure the fabricated prototype matches the simulated model. The antenna prototypes have been measured using a Rhode and Schwartz ZVA 40 [40].

The simulated and measured results which are in good agreement as shown in Figure 106 verify that the radiation pattern of this antenna element remains axial across the bandwidth 3.3 to 5 GHz. The gain is 6.22 dBi at 3.3 GHz and increases slightly to 6.42 dBi at 4 GHz, and finally drops to 4.31 dBi at 5 GHz. This gain drop at 5 GHz is negated in the array presented in the next section by a natural increase in array gain with frequency due to the longer electrical

distance between elements in the array. In other words, a reduction in the unit element gain at high frequencies will lead to a more consistent array gain over the bandwidth.

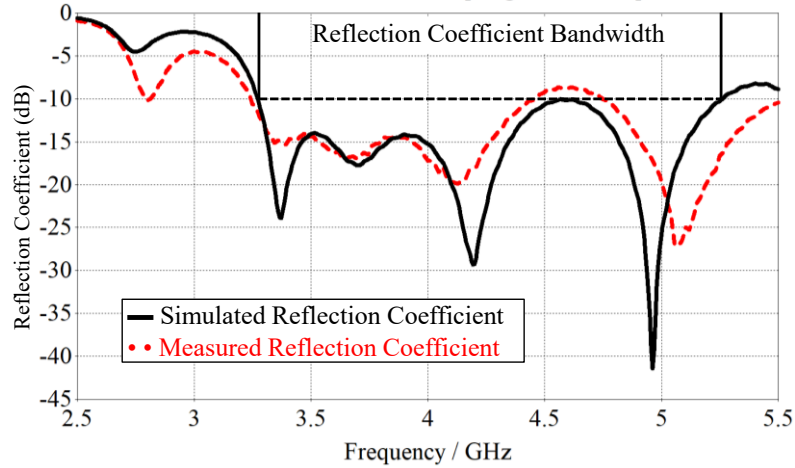


Figure 105. Reflection coefficients for the simulated model and measured prototype of the antenna.

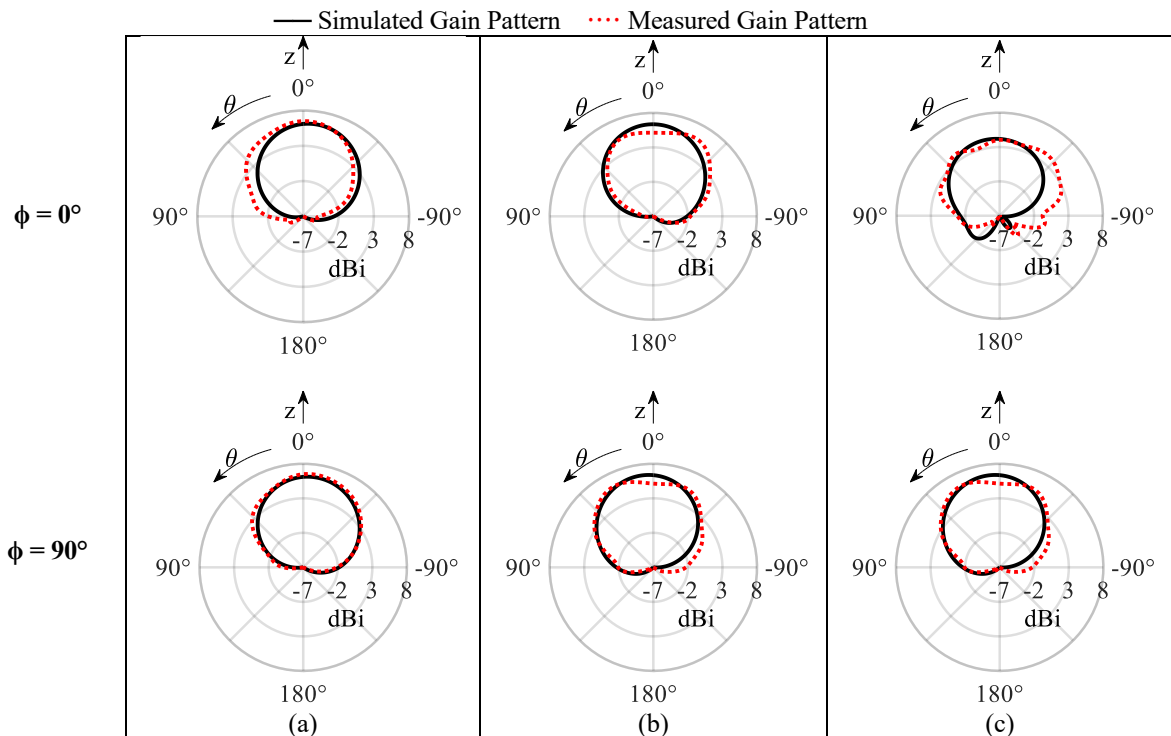


Figure 106. Radiation pattern polar plot cuts of the antenna element at $\phi = 0^\circ$ and $\phi = 90^\circ$ at (a) 3.3 GHz, (b) 4 GHz, (c) 5 GHz. The beam remains axial across all required frequencies.

The polarization of the compressed spiral antenna was found to remain elliptical across its operating bandwidth due to its compact design. Figure 107 displays the horizontal and vertical polarisation components of the antenna over the operating frequency band. From 3.3GHz to 4GHz, these component values remain close (difference $< 1.5\text{dB}$), as it does from 4.8 GHz to 5GHz. Between 4 GHz and 4.8 GHz, the horizontal component becomes the primary component and the difference between these reaches 3.2 dB at 4.5 GHz. This polarization profile is suitable for terrestrial communication. While there is some change in the polarisation over the frequency band, this can be resolved by choosing a circularly polarized antenna or a spiral element of the same design at both the base station and the user terminal.

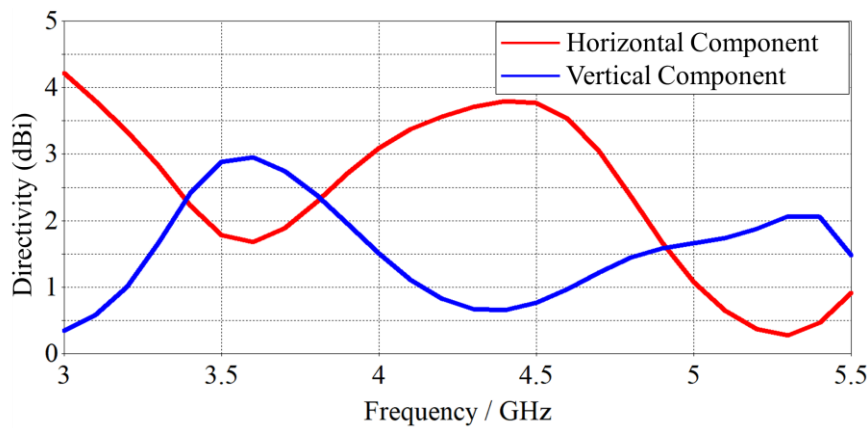


Figure 107. Polarisation components (in the Ludwig 3 coordinate system) of the antenna directivity in the broadside direction.

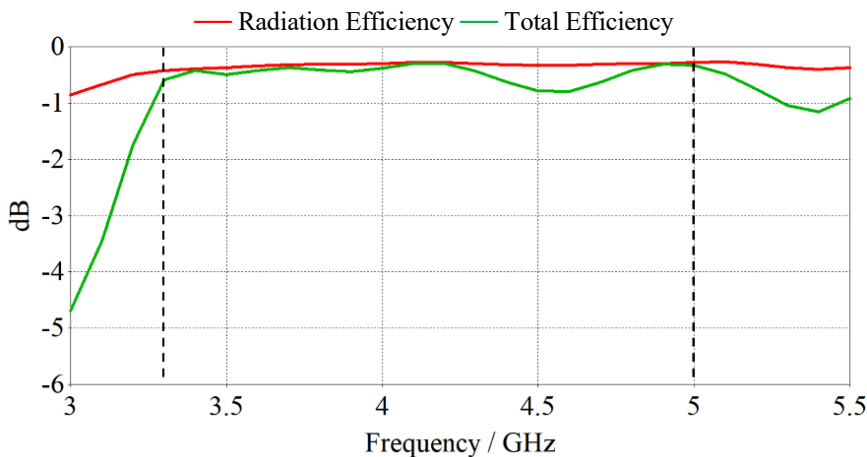


Figure 108. Simulated efficiencies of the optimised spiral design

Figure 108 displays the simulated radiation efficiency and total efficiency of the optimal spiral antenna element. The radiation efficiency is approximately 0.35 dB across the whole bandwidth. The total efficiency remains above 0.8 dB for the entire operational bandwidth. This is suitable for most modern applications.

5.4 Compressed Single-arm Spiral Antenna Array in a Triangular Lattice Design

5.4.1 4×4 Array Design

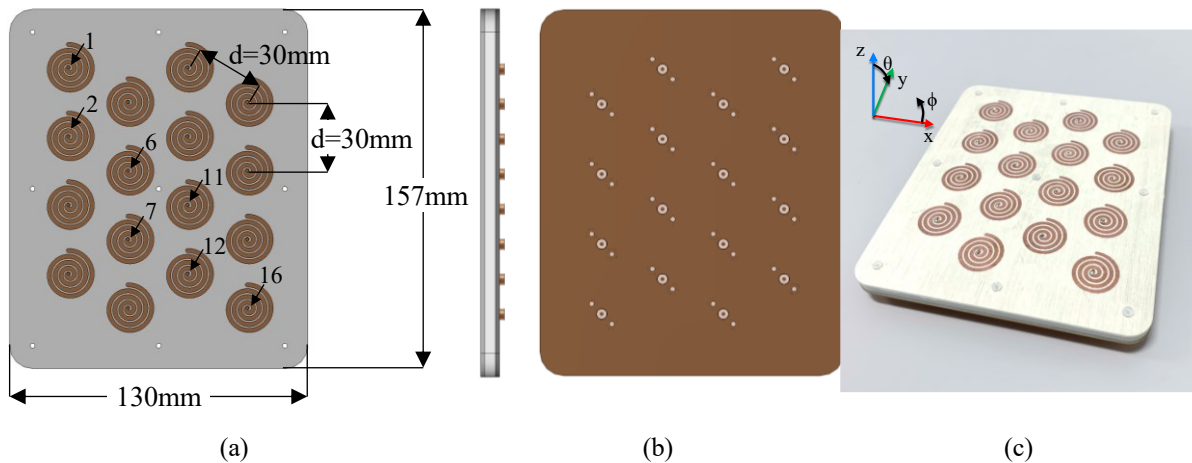


Figure 109. Compressed spiral antennas in a triangular lattice array. (a) Design diagram with dimensions and some port locations. (b) Side and back view of the antenna array design. (c) Fabricated prototype.

The compressed spiral antenna has been placed in a 16-element array configuration in a triangular lattice structure (Figure 109). This array topology ensures that all neighbouring elements have equal distance in all directions, thus reducing the grating lobes when the beam is steered (compared to a square lattice design) [80], [81]. Figure 109 shows the array design and the fabricated prototype. The inter-element distance is selected to be 30mm (varying from $0.33\lambda_{3.3\text{GHz}}$ to $0.5\lambda_{5\text{GHz}}$). As the compressed spiral element provides an axial beam, this array configuration was found to be able to provide a scanning range of $-40^\circ \leq \theta \leq +40^\circ$ from the

broadside. Indeed, it was found that the average grating lobe levels were better than -12 dB for $\theta = \pm 20^\circ$ scanning, better than -11 dB for $\pm 30^\circ$ scanning and better than -9.5 dB for $\pm 40^\circ$.

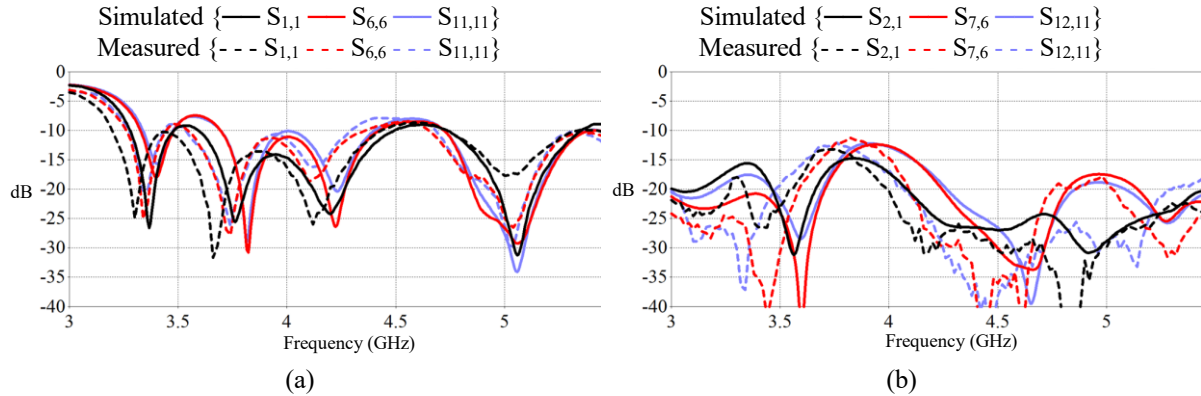


Figure 110. *S*-parameters of the triangular lattice array. (a) Reflection coefficients of ports 1, 6 and 11. (b) Isolation between selected ports and neighbouring elements 2, 7 and 12.

Figure 110 (a) displays the simulated and measured reflection coefficients of the array when port 1, 6 and 11 are excited. The results are in good agreement and show an adequate reflection coefficient bandwidth ranging over 3.3 GHz to 5 GHz. At a few ports the reflection coefficient was close to -7 dB.

Figure 110 (b) presents the isolation between three pairs of neighbouring elements, i.e.: 1 and 2, 6 and 7, and 11 and 12. It was found that the isolation remains below -15 dB for most of the operational bandwidth, increasing to -12.2 dB at 3.9 GHz for $S_{7,6}$ and $S_{12,11}$. Again the simulated and measured mutual coupling results were found to be better than -10 dB cut off criteria. Isolation could be further improved at lower frequencies by the use of a via structure, slotted ground plane [82] or the addition of a meta surface substrate or superstrate, [83], [84].

5.4.2 Antenna Feeding Network and Beam Steering Measurement

To experimentally examine the beam steering capability of the fabricated array, a feeding network was developed. This feeding network splits the main RF power into four feeding arms. Four phase shifters [P1-P4] are added to these four arms to produce four different

phases (β_1 - β_4) in the four columns of the array as shown in Figure 111 (a). This allows for elevation beam steering along the x-axis only. In the final operation, individual phase shifters per element using RFICs [85] can be implemented to enable full azimuth coverage. In this work we used two sets of phase shifters. One set of MACOM MAPS-010164 digital phase shifters were used up to 3.8 GHz and then MACOM MAPS-010165 phase shifters were used at higher frequencies from 3.8 – 5 GHz. These phase shifters were controlled with a Raspberry Pi as it can easily control the evaluation boards over a Serial Peripheral Interface (SPI). Figure 111 (b) shows the bespoke 1-4 Wilkinson's power divider design, and its fabricated prototype is shown in Figure 111 (c).

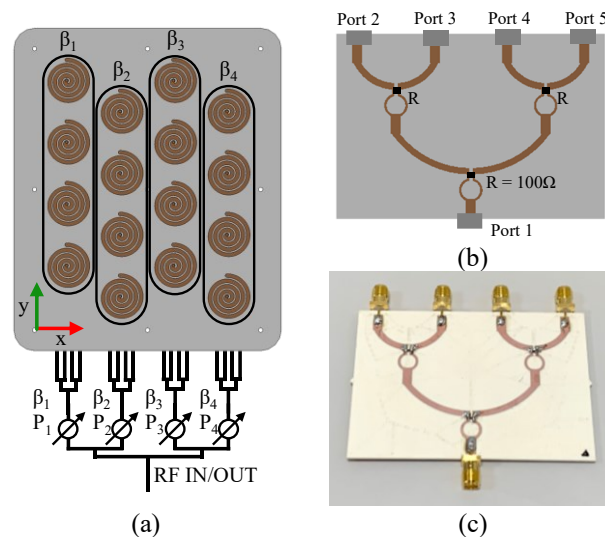


Figure 111. The prototype feeding network, (a) feeding network topology, (b) 1-4 Wilkinson power divider design, (c) 1-4 power divider prototype.

Antenna array beam steering results

The set-up for the array radiation pattern measurement is shown in Figure 112. The main RF is split to 16 feeding arms in group of four, each feeding one column. The 1-4 power divider s-parameters are presented in Figure 113. As expected, the simulated results are close to -6 dB across the operational bandwidth. The measured results match the simulated results.

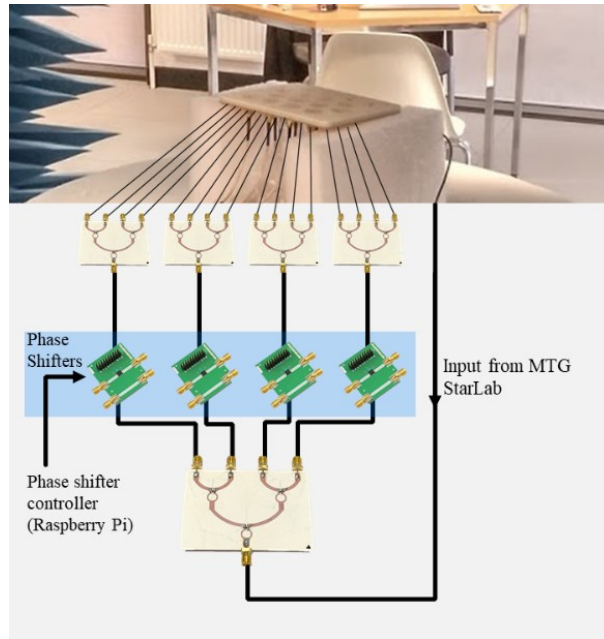


Figure 112. Radiation pattern measurement set-up for the prototype compressed spiral antenna array including the feeding network. Each antenna path is of equal length.

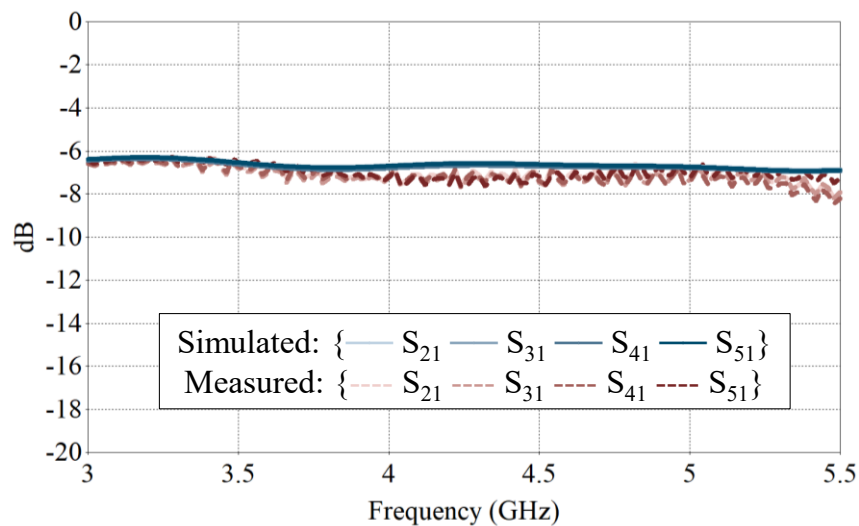


Figure 113. Simulated and measured s -parameters of the 1-4 power divider.

The simulated beamforming performance of the array in Figure 114 demonstrates the steering capability of the antenna array for 3.3 GHz, 4 GHz and 5 GHz across the azimuth planes $\phi = 0^\circ$, $\phi = 45^\circ$ and $\phi = 90^\circ$. The phase shift values used to achieve the results are shown in Table 6. The simulated gain in the broadside direction of the array varies from 13.9 dB at

3.3 GHz to 16.1 dB at 5 GHz. The array has a radiation efficiency of greater than 88% in all beam steering directions across all operational frequencies.

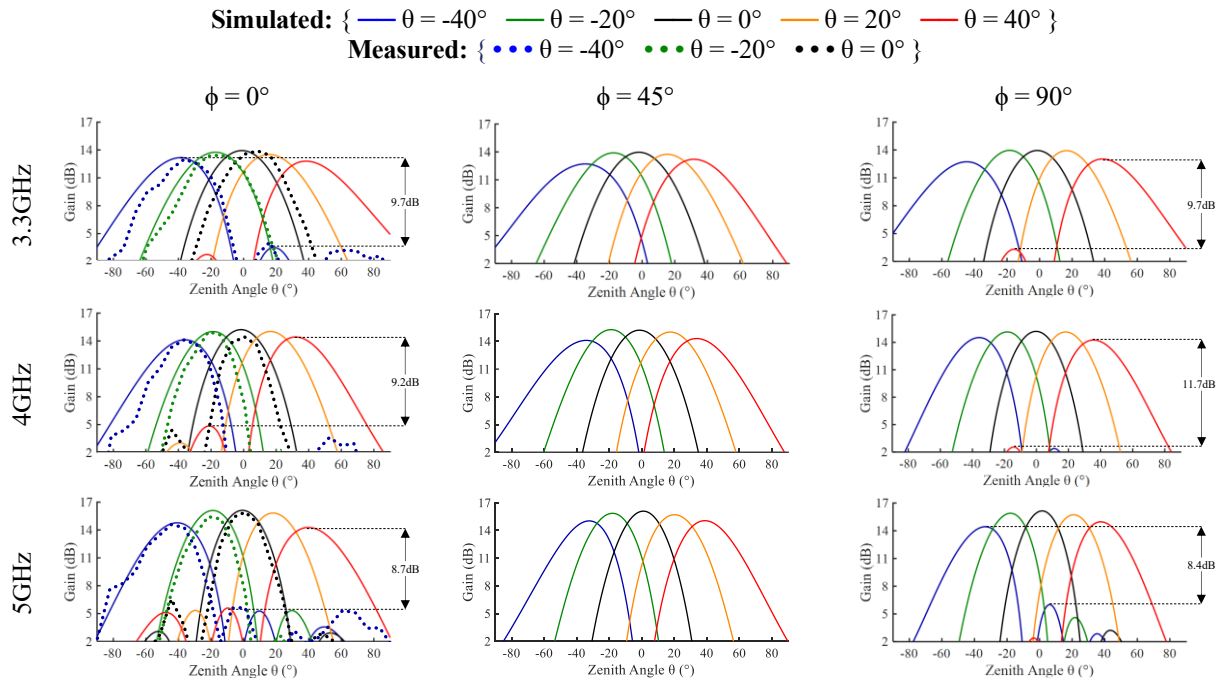


Figure 114. Steering performance as evaluated through simulation and measurement for the 16-element antenna array at $\phi = 0^\circ$ and $\phi = 90^\circ$. Measured data has been normalized in order to remove the impact of feeding network losses

Table 6. Phase shifting values used for beam steering results shown in Figure 14.

frequency	3.3 GHz			5 GHz		
θ_{max}	0°	20°	40°	0°	20°	40°
$\angle\beta_0$	0°	0°	0°	0°	0°	0°
$\angle\beta_1$	0°	35°	79°	0°	53°	110°
$\angle\beta_2$	0°	70°	158°	0°	106°	220°
$\angle\beta_3$	0°	105°	237°	0°	159°	330°

The measured radiation patterns of the array including the bespoke beamforming network are also displayed in Figure 114 for elevation steering. They are in good agreement with the simulated results and are normalized to avoid the impact of losses in the feeding network. An important aspect to note is that the spiral array provides wide bandwidth steering

where the gain varies by less than 3 dB from $\theta = 0^\circ$ to $\theta = 40^\circ$, across all frequencies. The grating lobes vary between 11.7 - 8.7 dB (average grating lobe level of -9.5 dB), which is better than the required value for terrestrial communications. It should be noted that no amplitude tapering has been applied to the array, so it is possible that grating lobe nulling could improve this performance further. There is an anomalous presence of one specific side lobe at $\theta = -45^\circ$ when steering to the boresight direction in the measured results beyond 4 GHz, which is not present in the simulation results. The 1-4 power dividers are placed close to the array in this azimuth direction and this could potentially be cause this anomaly. However, testing of the array with the power dividers placed far from the array or with an integrated feeding network would be necessary to verify this speculation.

5.5 Discussion

Table 7. A comparison between this work and relevant and state-of-the-art wideband beamforming solutions.

	This work	[69]	[75]	[76]	[74]	[78]	[79]
Antenna element type	Single arm spiral	Single arm spiral	4-arm spiral	Spiral	4-arm curl	Dipole	Coupled Dipole
Element size	$0.5\lambda_{\max}$	$0.88\lambda_{\max}$	$1.5\lambda_{\max}$	$0.5\lambda_{\max}$	$0.92\lambda_{\max}$	$0.48\lambda_{\max}$	$0.5\lambda_{\max}$
Element height	$0.12\lambda_{\max}$	$0.27\lambda_{\max}$	$>0.12\lambda_{\max}$	$0.12\lambda_{\max}$	$0.1\lambda_{\max}$	$0.65\lambda_{\max}$	$0.51\lambda_{\max}$
Bandwidth (%)	41	20	120	69	9.8	120	127
Azimuth steering	Yes	No	No	Yes	Yes	Yes	Yes
3dB variation steering angle	$\pm 40^\circ$	Not presented	Not presented	Not presented	$\pm 70^\circ$	$\pm 60^\circ$	$\pm 45^\circ$
Grating lobe level at 30° (dB)	-9	Not presented	0	-6	-9	-15	Not presented
Max Isolation (dB)	-11	Not presented	Not presented	-35	-21	Not presented	-47
Max Unit Element Gain	6.42	8.2	Not Presented	2*	8	5	5

*Approximation calculated from array gain

This work in this chapter presents a wideband phased array consisting of compressed spiral radiating elements arranged in a triangular lattice. The spiral element uses an optimized compressed design to provide 41% bandwidth for coverage of licensed 5G mid-bands from 3.3 GHz to 5 GHz. The unit antenna element generates an axial beam across the bandwidth while having a low profile ($0.128\lambda_{5\text{GHz}}$) and small size ($0.5\lambda_{5\text{GHz}}$). When placed in a triangular lattice, a less than 3 dB gain variation in beam steering in range of $-40^\circ \leq \theta \leq +40^\circ$ is achieved with an average sidelobe level of only -9.5 dB.

Table 7 displays a comparison between this work and other relevant array works. The design presented here provides a number of key advantages simultaneously. It provides a bandwidth greater than 40% while allowing for complete azimuth beamforming and steering to $\pm 40^\circ$ across the entire antenna bandwidth. This has been achieved in a highly compact structure far smaller than most existing spiral array designs. Furthermore, the spiral presented here is a single arm design and is therefore simpler to integrate with a feeding network.

The method presented here provides a low profile, low-cost and effective wideband beam steering solution ideal for seamless global 5G applications. While this has been developed primarily for terrestrial aviation scenarios, the final work is a light weight and compact design that will also enable usage in small UAVs and ground vehicles for both terrestrial 5G and LEO satellite communication.

Chapter 6.

Conclusion & Discussions

This work provides key innovations in three distinct areas of vehicular beamforming antenna arrays. In each area, beamforming arrays have been developed that utilise novel antenna designs to fulfil or exceed the application requirements in a compact and low-profile form factor. It is vital that any communication system for vehicular applications are as compact as possible as it can both significantly impact the aerodynamics of the vehicle and the ability to integrate the system effectively. This is true of both ground vehicles but aircraft and UAVs.

6.1 Low-Profile L-Band Switch Beam Phased Array

The first area of innovation in this work is the development of a flat panel antenna array for GEO satellite communication to be integrated in emergency vehicle lightbars. This system is, as far as we are aware, the first linear antenna array capable of providing full azimuth steering coverage down to $\theta = 70^\circ$ with circular polarisation. The system achieves this by using wideband quad-arm curl antenna elements with a switchable beam in a rotated linear phased array. This hybrid switch beam phased array requires only 4 phase shifters, 3 LNAs and 3 HPAs for both the receive and transmit channels. This is more than a five times reduction in components when compared to a standard 4×4 phased arrays. Furthermore, in each element a high impedance meta-surface has been implemented to reduce the height of the quad arm curl antenna element by 50%. As a result of these innovations, this system is far more compact than existing mechanical systems and does not suffer from high power requirements and reduced reliability. Vitally, the low-cost beamforming network required provides a key commercial

advantage over current systems. At this point in time, there is little uptake of satellite internet access in emergency vehicles due to the high cost and integration issues. This work will allow emergency vehicles to cost effectively access reliable and consistent communication, even in areas where cellular networks fail to provide coverage.

This work can be expanded upon in a number of ways to improve both RF and mechanical performance of the antenna array. Firstly, while the existing array design is ideal for the application selected, the topology is limited in its overall gain. To expand the method to other applications, it would be worthwhile exploring other array geometries with a higher number of elements in the array in order to improve the array performance. Alternatively, increasing the number of curl arms in the antenna element could also enable greater array performance. While both these methods could increase the size of the array, for higher frequency applications this would not be an issue. Secondly, the current Delrin plastic utilised for the substrate, while allowing of the low profile of the antenna, does add weight to the array. Additive manufacturing of the antenna element substrate could be introduced to reduce the antenna weight by approximately 40% by using a high permittivity 3D printing material such as PrePerm [86].

6.2 Ka-Band Shared Aperture Array with Reconfigurable Circular Polarisation

In Chapter 4, a Ka-band shared aperture antenna array is presented for direct integration into ground vehicles. This shared aperture antenna array provides coverage for 18.8 – 20.2 GHz for receive and 27.5 – 30 GHz for transmit and reconfigurable circular polarisation. This is achieved in a single antenna plane and can be easily fabricated with existing PCB manufacturing methods. Here a triangular antenna element has been designed for both received and transmit antenna elements such that, when placed in an interlaced triangular lattice, optimal tessellation of elements is realised. As a result, mutual coupling is significantly reduced, and

ideal beam steering performance is realised. Furthermore, reconfigurable circular polarisation is realised via two complementary techniques. Firstly, antenna elements are fed with a quadrature feeding technique such that the element circular polarisation can be selected with phase control. Second, sequential 120° rotation of both receive and transmit antenna elements is utilised so that the excitation phase of each element will select the circular polarisation mode. These two techniques combined lead to an optimal axial ratio at all beam steering angles. Finally, this design has been built and simulated on a complete PCB layer stack including a coaxial feeding structure and matching network that allows for fabrication within the limits of existing PCB manufacturing techniques. The PCB layer design and feeding structure has then been verified for suitability via a prototype antenna array board. This innovative design results in high performance from a single antenna layer, unlike existing shared aperture designs that require receive and transmit arrays to occupy separate layers of the PCB. Furthermore, it also enables reconfigurable circular polarisation in a single PCB structure. Overall, this design enables low-cost fabrication an integration for future vehicles to enable high speed internet access from anywhere in the world.

The shared aperture antenna array configuration allows for a number of avenues of future work. The obvious next step is the development of a final prototype including RFIC integration. While the PCB structure has been verified via a split aperture prototype, a full array fabrication is the natural next step. Secondly, the current design utilises single resonance unit element however, where the patches slotted such that a second resonance was produced, then the bandwidth requirements could be reached with a lower PCB height. The same outcome could also be produced with the integration of a meta surface in the substrate (as developed in Chapter 3) and may also reduce mutual coupling and grating lobes of the array. Finally, to fully unlock the steering capability of the shared aperture array, amplitude tapering can be introduced to further improve the arrays beam steering capability.

6.3 Wideband Compressed Spiral Array for Global Mid-Band 5G

Finally, a wideband compressed spiral array has been developed to enable ground-to-air 5G internet access for aircraft. Here, a compressed spiral antenna has been designed and optimised to provide wideband coverage from 3.3 GHz to 5 GHz while maintaining a consistent axial radiation pattern. This compressed spiral antenna has been designed such that it has a low profile (0.1λ) compared to other spiral antennas. When placed in a triangular antenna array, this design provides beam steering to $\theta = \pm 40^\circ$. As each country and region has licensed different parts of the mid-band 5G spectrum, this design is the only antenna array, to our knowledge, that provides the bandwidth and beam steering performance to meet this requirement while maintaining a low-profile design suitable for aircraft integration. Due to the compact design, this would also be suitable for small aircraft such as UAVs.

This work can be expanded in a number of directions in the future. Firstly, the antenna element and array could be further optimised to provide circular polarisation. This could be achieved by altering the spiral antenna design or by utilising the sequential rotation presented in Chapter 4. Where sequential rotation used, the polarisation may also be configurable. Secondly, there is room to further expand the bandwidth of the spiral antenna axial beam by altering the structure of the antenna. By utilising a spiral with non-uniform amplitude, the phase across the spiral could be managed such that the beam remains axial over an even wider bandwidth.

6.3.1 Summary

In summary, this work presents three novel antenna and antenna array designs that provide solutions for key challenges currently faced by the communications industry that have yet to be fully resolved by existing work. All of the antenna arrays presented here achieve the required beam steering for the application in a low-profile and compact design. Further, each design takes into account limitations of manufacture to ensure the cost of each design is suitable

for commercial usage. This work presents a clear direction of travel for antenna design in each of the chosen application that minimises size and cost while maximising performance.

List of Figures

Figure 1. Three type of standard antennas: (a) monopole antenna, (b) dipole antenna, (c) horn antenna and (d) microstrip antenna.....	11
Figure 2. The equivalent circuit of a microstrip antenna with alternative feeding methods....	12
Figure 3. A Smith Chart displaying normalised impedance of the antennas shown in Figure 2 for the frequency range of 2.9 – 3.1 GHz. The reference circle for the -10 dB reflection coefficient is also shown.	13
Figure 4. Antenna Pattern and Coordinates (a) in 3D and (b) via a 2D cut of the antenna pattern.	17
Figure 5. The three broad categories of radiation patterns	18
Figure 6. Anatomy of a radiation pattern.	19
Figure 7. Three categories of polarisation. Diagram taken from [15].	22
Figure 8. Common patch antenna design.	24
Figure 9. Three beamforming solutions for vehicular antennas. (a) Fully mechanical reflector antenna [23] (b) Hybrid mechanical and electronic reflector antenna [24] (c) Hybrid mechanical and electronic phased array antenna [25].	28
Figure 10. An electronic beam steering antenna array [26]	29
Figure 11. Sequential element rotation utilised to improve axial ratio at low steering angles [26]	29
Figure 12. Beam steering capability of the antenna array presented in [19] (a) Fairfield of array beam at $\pm 40^\circ$ (b) Axial ratio of the array across elevation steering angles.....	30
Figure 13. Geometry of the unit cell presented in [29].....	31
Figure 14. Fabricated phased array as presented in [29].	31
Figure 15. Active VSWR of the antenna array at various steering angles in the E and H-plane as presented in [29].	31

Figure 16. Measured and simulated co and cross polar performance of the antenna array presented in [29].	31
Figure 17. A linear 1x11 antenna array presented in [30] (a) side view, (b) top view, and (c) substrate meta-surface.	33
Figure 18. Simulated and measured reflection coefficient of the antenna presented in [30].	33
Figure 19. Beam steering capabilities of the antenna array presented in [30]. This displays the H-plane pattern of the antenna array when steered using (a) phase control only and (b) amplitude and phase control.	33
Figure 20. A multiband, wideband phased array design, presented in [31] showing (a) the antenna element geometry and components and (b) the antenna array geometry.	34
Figure 21. Reflection coefficient of the antenna element presented in [31]. By changing the state of the RF switches, shown in Figure 20 (a), multiple bandwidths can be targeted.	35
Figure 22. The beamforming performance of the antenna array presented in [31] at (a) 1.35 GHz and (b) 2.95 GHz.	35
Figure 23. The 4-arm curl antenna design utilised in [32] showing port assignments, P1 to P4: (a) top view, (b) side view.	36
Figure 24. The s-parameters of the antenna element presented in [32]: (a) reflection coefficient, (b) isolation.	37
Figure 25. The tilted beam provided by the 4- arm curl in [32] at (a) 1500 MHz, (b) 1575MHz and (c) 1670 MHz.	37
Figure 26. QACH element: (a) Antenna geometry top and side view, (b) HIS configuration. All units are in mm.	38
Figure 27. Isometric view of the antenna design (with ports and coordinates).	39
Figure 28. Fabricated QACH element prototype.	39

Figure 29. (a) Initial HIS unit model. (b) The resultant reflection phase diagram. The initial theoretical design where $x = 5.82$ mm showing good phase matching for radiation normal to the surface. Optimization within QACH element done to provide better performance for the tilted beam application, resulting in x becoming 9.66 mm.....	41
Figure 30. The average surface currents over the QACH antenna element at the centre frequency of 1.597 GHz.....	41
Figure 31. Simulated and measured S-parameters of QACH antenna element shown in Figure 26.....	43
Figure 32. Simulated and measured RHCP and LHCP radiation patterns of QACH antenna element at (a) 1.518 GHz, (b)1.559 GHz, (c)1.627 GHz and (d) 1.675 GHz over the operating frequency band.....	44
Figure 33. QACH array: (a) 1×3 linear array design (units in mm); (b) array prototype.....	44
Figure 34. Diagram of the simple, low-cost feeding network for the 1×3 QACH array.	45
Figure 35. Example diagram of the hybrid beam-steering method.	46
Figure 36. QACH array performance test setup.	47
Figure 37. Beam steering performance (predicted & measured) of the 1×3 QACH array: (a) & (b) gain and (c) & (d) axial ratio at 1.538 GHz & 1.651 GHz.....	47
Figure 38. Simulated and measured RHCP and LHCP polar patterns showing the array steering performance for Tx and Rx beam maximum. (a) Tx beam targeting $(\theta, \phi) = (70^\circ, 45^\circ)$; (b) Tx beam targeting $(\theta, \phi) = (45^\circ, 90^\circ)$ & (c) Rx beam targeting $(\theta, \phi) = (45^\circ, 90^\circ)$	48
Figure 39. Array reflection coefficients and isolation between the 12 ports.	49
Figure 40. Third Generation Starlink Terminal [48].....	52
Figure 41. A teardown of a Starlink third generation phased array antenna showing (a) back view [50], (b) close up of slot feeding outline [51] and (c) a view of the antenna layers and hexagonal spacer [52].	53

Figure 42. A stylised diagram of the shared aperture antenna array currently in development by Amazon project Kuiper [54].	55
Figure 43. A side view of the Amazon Kuiper terminal antenna [54].	55
Figure 44. Design and function of the lens antenna systems: (a) isometric view of the lens antenna system [57], (b) the method of switch beam steering for the lens [56] and (c) switch beam steering network [56].	57
Figure 45. Parameters and limitations of PCB manufacturing. Image courtesy of Celestia UK.	59
Figure 46. PCB structure and material information. Thickness is displayed in μm .	59
Figure 47. Receive PCB antenna design with coaxial feeding structure and transform microstrip waveguide with (a) perspective view of the antenna feeding structure including port allocation, (b) detailed top side and back views.	61
Figure 48. Reflection coefficient and isolation of the Rx circular patch antenna design	62
Figure 49. The radiation pattern of the Rx circular patch antenna element in RHCP mode where both ports are excited with a 90° phase difference.	63
Figure 50. Transmit antenna design with coaxial feeding structure and transform microstrip waveguide with (a) perspective view of the antenna feeding structure including port allocation, (b) detailed top side and back views.	64
Figure 51. Reflection coefficient and isolation of the Tx circular patch antenna design	65
Figure 52. The radiation pattern of the Tx circular patch antenna element in RHCP mode where both ports are excited with a 90° phase difference.	66
Figure 53. A series of antenna array topologies tested to provide optimal beamforming and axial ratio.	67
Figure 54. Phase shifting method when utilising 90° sequential rotation.	68

Figure 55. 8x8 receive antenna array design with 90° sequential element rotation and a triangular lattice.	69
Figure 56. Beamforming of the Rx antenna array in RHCP mode across the operational bandwidth.....	70
Figure 57. 8x8 receive antenna array design with 90° sequential element rotation and a triangular lattice.	71
Figure 58. Beamforming of the Rx antenna array in RHCP mode across the operational bandwidth.....	72
Figure 59. Prototype board developed by Celestia UK using the split aperture designs presented here.....	73
Figure 60. Structure of the simulated Rx section of the prototype board. (a) Excited ports and location. (b) Simulated design.	74
Figure 61. Measured and simulated reflection coefficient of the Rx prototype antenna excitation ports (a) J14, (b), J16, (c) J17 and (d) J19.	74
Figure 62. Measured isolation between ports of the Rx prototype antenna array.....	75
Figure 63. Simulated and measured pattern of the prototype receive antenna array excitation ports (a) J14, (b) J16, (c) J17 and (d) J19.	76
Figure 64. Structure of the simulated Tx section of the prototype board. (a) Excited ports and location. (b) Simulated design.	77
Figure 65. Measured and simulated reflection coefficient of the Tx prototype antenna elements (a) J1, (b), J2, (c) J11 and (d) J13.	78
Figure 66. Isolation between ports of the Tx prototype antenna array.	79
Figure 67. Simulated and measured pattern of the prototype transmit antenna array excitation ports (a) J1, (b) J2, (c) J11 and (d) J13.	79

Figure 68. Interlaced Shared Aperture Topology. Rx elements shown in red. Tx elements shown in blue.....	80
Figure 69. Bevelled triangular receive patch antenna element and coaxial feeding design. Shows (a) perspective view with port allocation and (b) detailed top, side and back views...81	81
Figure 70. Reflection coefficient and isolation of the Rx bevelled triangular patch antenna element.....	82
Figure 71. The radiation pattern of the Rx bevelled triangular patch antenna element in RHCP mode where both ports are excited with a 90° phase difference.....	83
Figure 72. Transmit bevelled triangular patch antenna element and coaxial feeding design. Shows (a) perspective view with port allocation and (b) detailed top, side and back views...84	84
Figure 73. Reflection coefficient and isolation of the Rx bevelled triangular patch antenna element.....	85
Figure 74. The radiation pattern of the Rx bevelled triangular patch antenna element in RHCP mode where both ports are excited with a 90° phase difference.....	86
Figure 75. Shared aperture antenna array design. Units in mm.....	87
Figure 76. Beamforming of the Rx antenna array in RHCP mode across the operational bandwidth.....	88
Figure 77. Beamforming of the Tx antenna array in RHCP mode across the operational bandwidth.....	89
Figure 78. E-Shaped Antenna Presented in [66].....	96
Figure 79. Half E-Shaped Antenna Presented in [67].....	96
Figure 80. Slotted Patch Antenna presented in [68].	96
Figure 81. A reflector plane backed spiral antenna presented in [69].....	97
Figure 82. HIS-Based Spiral Antenna presented in [37].	97

Figure 83. A low profile single arm spiral antenna presented in [71] and the variation in radiation pattern over its bandwidth.	97
Figure 84. A 1x4 Array of Wideband Dual-Circularly Polarised Antennas as presented in [75].	99
Figure 85. Radiation patterns of the antenna element presented in [75] over the bandwidth of the antenna.	99
Figure 86. Radiation patterns of the antenna array presented in [75] over the bandwidth of the antenna when a phase shift of $\Delta\beta = 90^\circ$ is applied.	99
Figure 87. The array and antenna element design of the wideband four arm spiral antenna array presented in [76].	101
Figure 88. Active VSWR of the Tx antenna array presented in [76].	101
Figure 89. Transmit Element pattern and antenna array scanning performance of the array presented in [76].	101
Figure 90. Ring antenna array prototype as presented in [77]. (a) Top view. (b) Side View.	102
Figure 91. Simulated and measured reflection coefficient of the spiral antenna array presented in [77].	103
Figure 92. Simulated and measured Relative Side Lobe Level (RSLL) of the antenna array when steering to presented in [77].	103
Figure 93. The (a) antenna element and (b) antenna array, presented in [78]	104
Figure 94. Simulated active VSWR in 0° , 30° and 60° scanning angles of the antenna presented in [78]. (a) Horizontal polarisation. (b) Vertical polarisation.	104
Figure 95. Measured Co-polarisation scanning performance of the antenna array presented in [78] at (a) 1 GHz and (b) 2 GHz.	104

Figure 96. The configuration of the tightly coupled dipole array presented in [79]. (a) Top view of the dipole layer. (b) Array cross section. (c) Perspective view of the array excluding dielectric materials.....	105
Figure 97. The active VSWR of the array presented in [79].	106
Figure 98. Realised gain pattern of the central element of the array at (a) 4GHz, and (b) 18 GHz. As presented in [79]. (No phi value is given but assumed to be $\phi = 0^\circ$).....	106
Figure 99. Compressed spiral antenna, its dimensions and top view and side view (left) alongside the perspective and bottom view (right).....	108
Figure 100. Orthographic radiation patterns of the compressed spiral antenna with a spiral amplitude of $a = 0.32$ mm/rad, $a = 0.41$ mm/rad, and $a = 0.6$ mm/rad across the frequency bandwidth. The optimal design ($a = 0.41$ mm/rad) shows minimal deviation from the broadside direction.	109
Figure 101. Reflection coefficients of the three-spiral antenna with spiral amplitudes of $a = 0.32$ mm/rad, $a = 0.41$ mm/rad and $a = 0.65$ mm/rad. Only the optimized model with amplitude $a = 0.41$ mm/rad provides the required bandwidth for the targeted application.	110
Figure 102. Orthographic radiation patterns of the optimal spiral antenna where the height of the substrate has been varied from 3.7 mm to 11.7 mm with a constant amplitude of $a = 0.41$ mm/rad and a number of turns of $T = 4.13$	111
Figure 103. Reflection coefficients of the optimised spiral design with substrate height variation from $h = 3.7$ mm to $h = 11.7$ mm.....	111
Figure 104. Prototype of compressed spiral antenna; left: front and right: back view.	112
Figure 105. Reflection coefficients for the simulated model and measured prototype of the antenna.	113
Figure 106. Radiation pattern polar plot cuts of the antenna element at $\phi = 0^\circ$ and $\phi = 90^\circ$ at (a) 3.3 GHz, (b) 4 GHz, (c) 5 GHz. The beam remains axial across all required frequencies....	113

Figure 107. Polarisation components (in the Ludwig 3 coordinate system) of the antenna directivity in the broadside direction.	114
Figure 108. Simulated efficiencies of the optimised spiral design	114
Figure 109. Compressed spiral antennas in a triangular lattice array. (a) Design diagram with dimensions and some port locations. (b) Side and back view of the antenna array design. (c) Fabricated prototype.	115
Figure 110. S-parameters of the triangular lattice array. (a) Reflection coefficients of ports 1, 6 and 11. (b) Isolation between selected ports and neighbouring elements 2, 7 and 12.	116
Figure 111. The prototype feeding network, (a) feeding network topology, (b) 1-4 Wilkinson power divider design, (c) 1-4 power divider prototype.	117
Figure 112. Radiation pattern measurement set-up for the prototype compressed spiral antenna array including the feeding network. Each antenna path is of equal length.	118
Figure 113. Simulated and measured s-parameters of the 1-4 power divider.	118
Figure 114. Steering performance as evaluated through simulation and measurement for the 16-element antenna array at $\phi = 0^\circ$ and $\phi = 90^\circ$. Measured data has been normalized in order to remove the impact of feeding network losses.	119

List of Tables

Table 1. A comparison between this work and existing works.	49
Table 2. Selected requirements for a Ka band LEO phased array antenna.	58
Table 3. Results of antenna array rotation topology for gain, grating lobes and axial ratio. ...	67
Table 4. Comparison between the split aperture antenna array and shared aperture antenna array.	90
Table 5. Existing wideband patch antennas and spiral antennas, including information about the bandwidth and pattern of each antenna.	95
Table 6. Phase shifting values used for beam steering results shown in Figure 14.	119
Table 7. A comparison between this work and relevant and state-of-the-art wideband beamforming solutions.	120

References

- [1] Roland Berger, “Computer on wheels: disruption in automotive electronics and semiconductors,” Roland Berger, Munich, Germany, 2020.
- [2] International Telecommunication Union, “Attenuation by atmospheric gasses,” International Telecommunication Union, 2016.
- [3] Ofcom, “Connected nations 2021: UK report,” 2021. [Online]. Available: https://www.ofcom.org.uk/__data/assets/pdf_file/0035/229688/connected-nations-2021-uk.pdf. [Accessed 05 09 2022].
- [4] Qualcomm, “Global update on spectrum for 4G & 5G,” 2020. [Online]. Available: <https://www.qualcomm.com/media/documents/files/spectrum-for-4g-and-5g.pdf>. [Accessed 09 08 2022].
- [5] Inmarsat Global, “The European aviation network,” 2015. [Online]. Available: www.telekom.com/resource/blob/390304/973659827c8e68d7db8141a5ed3a3596/dl-150929-datenblatt-data.pdf . [Accessed 09 08 2022].
- [6] J. Ramsay, “Highlights of antenna history,” *IEEE Antennas and Propag. Society Newsletter*, pp. 7-20, December 1981.
- [7] T. Edison, “A Means for Transmitting Signals Electrically”. U.S Patent 456,917, 29 December 1891.
- [8] J. A. Fleming, *The Principles of Electric Wave Telegraphy and Telephony*, New York: Longmans, Green, and Co., 1916.
- [9] International Telecommunication Union, “Measuring digital development: Facts and Figures,” ITU Publications, Geneva, Switzerland, 2021.

- [10] J. D. Kraus and R. J. Marhefka, *Antennas For All Applications: Thrid Edition*, New York: McGraw-Hill, 2002.
- [11] N. K. Nikolova, *Notes on Antenna Engineering 2018*, Hamilton: McMaster University, 2018.
- [12] C. A. Balanis, *Antenna Theory: Third Edition*, Hoboken: John Wiley & Sons, 2005.
- [13] D. M. Pozar, "Transmisiion line theory," in *Microwave Engineering: Fouth Edition*, Danvers, John Wiley & Sons, 2012, p. 48.
- [14] IEEE, "IEEE standard definitions of terms for antennas," *IEEE Std 145-2013*, pp. 1-50, 2014.
- [15] A. Linux, "Polarization," *Microwaves101*, [Online]. Available: <https://www.microwaves101.com/encyclopedias/polarization>. [Accessed 25 08 2022].
- [16] Dassault Systèmes SE, "CST studio suit," [Online]. Available: <https://www.3ds.com/products-services/simulia/products/cst-studio-suite/>. [Accessed 5 Dec. 2019].
- [17] TATA Communications, "Unleashing cellular connectivity for IoT applications," July 2019. [Online]. Available: <https://www.tatacommunications.com/wp-content/uploads/2019/07/Whitepaper-Unleashing-cellular-connectivity-for-IoT-applications.pdf>. [Accessed 10 Dec 2019].
- [18] Inmarsat plc, "Inmarsat BGAN for land," 2018. [Online]. Available: https://www.inmarsat.com/wp-content/uploads/2015/06/Inmarsat_BGAN_For_Land_USGov_April_2014_EN_LowRes.pdf. [Accessed 12 Dec 2020].
- [19] Ground Control, "The BGAN coverage map," [Online]. Available: <https://www.groundcontrol.com/bgancoveragemap.htm>. [Accessed 14 Apr. 2020].

- [20] Inmarsat plc, “Cobham EXPLORER 323 and EXPLORER 6075LX terminals receive Inmarsat type approval,” 15 Dec 2020. [Online]. Available: <https://www.inmarsat.com/en/news/latest-news/enterprise/2020/cobham-explorer-323-and-explorer-6075lx-terminals-receive-inmarsat-type-approval.html>. [Accessed 15 Dec 2020].
- [21] H. Bayer, A. Krauss, T. Zaiczek, R. Stephan, O. Enge-Rosenblatt and M. A. Hein, “Ka-band user terminal antennas for satellite communications,” *IEEE Antennas Propag. Mag.*, vol. 58, pp. 76-88, 2016.
- [22] A. V. Shishlov, “Vehicular antennas for satellite communications,” in *2011 VIII Intern. Conf. Antenna Theory and Techn.*, Kyiv, 2011.
- [23] Intellian, “GX60NX,” Intellian, [Online]. Available: www.intelliantech.com/products/inmarsat-gx-maritime-terminal/gx60nx. [Accessed 20 Jun. 2022].
- [24] Y.-B. Jung, A. V. Shishlov and S.-O. Park, “Cassegrain antenna with hybrid beam steering scheme for mobile satellite communications,” *IEEE Trans. on Antennas and Propag.*, vol. 57, no. 5, pp. 1367-1372, 2009.
- [25] P. Mousavi, M. Fakharzadeh, S. H. Jamali, K. Narimani, M. Hossu, H. Bolandhemmat, G. Rafi and S. Safavi-Naeini, “A low-cost ultra low profile phased array system for mobile satellite reception using zero-knowledge beamforming algorithm,” *IEEE Trans. on Antennas and Propag.*, vol. 56, no. 12, pp. 3667-3679, 2018.
- [26] N. Buchanan, V. F. Fusco, D. Zelenchuk and M. van der Vorst, “A circular polarized self-tracking L band array with high bandwidth and scan beamwidth for Inmarsat BGAN applications,” in *Proc. of the 5th Eur. Conf. on Antennas Propag. (EUCAP)*, Rome, 2015.

- [27] J. Huang, "L-band phased array antennas for mobile satellite communications," in *37th IEEE Vehic. Technol. Conf.*, Tampa, 1987.
- [28] A. Deshmukh, R. Patil, R. Maurya and V. A. P. Chavali, "Modified feed corner truncated square microstrip antenna for circular polarized response," in *2020 3rd Int. Con, on Commun. Syst., Comput. and IT Appl. (CSCITA)*, 2020.
- [29] J. A. Kasemodel, C.-C. Chen and J. L. Volakis, "Wideband planar array with integrated feed and matching network for wide-angle scanning," *IEEE Trans. Antennas Propag.*, vol. 61, no. 9, pp. 4528-4537, 2013.
- [30] R. Wang, B.-Z. Wang, X. Ding and X.-S. Yang, "Planar phased array with wide-angle scanning performance based on image theory," *IEEE Trans. Antennas Propag.*, vol. 63, no. 9, pp. 3908-3917, 2015.
- [31] N. Haider, A. G. Yarovoy and A. G. Roederer, "L/S-band frequency reconfigurable multiscale phased array antenna with wide angle scanning," *IEEE Trans. Antennas Propag.*, vol. 65, no. 9, pp. 4519-4528, 2017.
- [32] H. Zhou, A. Pal, A. Mehta, D. Mirshekar-Syahkal and H. Nakano, "A four-arm circularly polarized high-gain high-tilt beam curl antenna for beam steering applications," *IEEE Antennas Wireless Propag. Letters*, vol. 17, no. 7, p. 1034 – 1038, 2018.
- [33] B. Schneiderman, "The next wave: low earth orbit constellations," 4 Mar. 2019. [Online]. Available: <http://satellitemarkets.com/news-analysis/next-wave-low-earth-orbit-constellations>. [Accessed 15 Dec. 2019].
- [34] H. Nakano, K. Hitosugi, N. Tatsuzawa, D. Togashi, H. Mimaki and J. Yamauchi, "Effects on the radiation characteristics of using a corrugated reflector with a helical antenna and an electromagnetic band-gap reflector with a spiral antenna," *IEEE Trans. Antennas Propag.*, vol. 53, no. 1, pp. 191-199, 2005.

- [35] F. Yang and Y. Rahmat-Samii, "A low-profile circularly polarized curl antenna over an electromagnetic bandgap (EBG) surface," *Microw. Opt. Technol. Lett.*, vol. 31, no. 4, 2001.
- [36] P. Deo, A. Mehta, D. Mirshekar-Syahkal, P. J. Massey and H. Nakano, "Thickness reduction and performance enhancement of steerable square loop antenna using hybrid high impedance surface," *IEEE Trans. Antennas Propag.*, vol. 58, no. 5, 2010.
- [37] P. Deo, A. Mehta, D. Mirshekar-Syahkal and H. Nakano, "An HIS-based spiral antenna for pattern reconfigurable applications," *IEEE Antennas Wireless Propag. Lett.*, vol. 8, pp. 196-199, 2009.
- [38] W. Zhang, A. Pal, A. Mehta, D. Mirshekar-Syahkal and H. Nakano, "Low profile pattern-switchable multibeam antenna consisting of four L-shaped microstrip lines," *IET Microwaves, Antennas Propag.*, vol. 12, no. 11, pp. 1846-1851, 2018.
- [39] H. Nakano, S. Okuzawa, K. Ohishi, H. Mimaki and J. Yamauchi, "A curl antenna," *IEEE Trans. Antennas Propag.*, vol. 41, no. 11, pp. 1570-1575, 1993.
- [40] Rhode and Schwartz, "R&S ZVA vector network analyzer specifications," 03 2014. [Online]. Available: https://scdn.rohde-schwarz.com/ur/pws/dl_downloads/dl_common_library/dl_brochures_and_datasheets/pdf_1/ZVA_dat-sw_en_5213-5680-22_v1100.pdf. [Accessed 17 08 2022].
- [41] C.-K. Hsu and S.-J. Chung, "Compact multiband antenna for handsets with a conducting edge," *IEEE Trans. on Antennas Propag.*, vol. 63, no. 11, pp. 5102-5107, 2015.
- [42] C. Huang, Y.-C. Jiao, Z.-B. Weng and X. Li, "A planar multiband antenna based on CRLH-TL ZOR for 4G compact mobile terminal applications," in *2018 Intern. Workshop Antenna Technol.*, Nanjing, 2018.

- [43] Microwave Vision Group., “MVG Star Lab 650-1800 MHz,” [Online]. Available: <https://www.mvg-world.com/en/products/antenna-measurement/multi-probe-systems/starlab>. [Accessed 19 Oct. 2018].
- [44] H. Zhou, A. Pal, A. Mehta, H. Nakano, A. Modigliana, T. Arampatzis and P. Howland, “Reconfigurable phased array antenna consisting of high-gain high-tilt circularly polarized four-arm curl elements for near horizon scanning satellite applications,” *IEEE Antennas Wireless Propag. Lett.*, vol. 17, no. 12, p. 2324 – 2328, 2018.
- [45] Ensilica, “Home page,” [Online]. Available: <https://www.ensilica.com/>. [Accessed 31 08 2022].
- [46] Celestia UK, “Celestia UK,” [Online]. Available: <https://www.celestia-uk.com/>. [Accessed 31 08 2022].
- [47] Satellite Applications Catapult, “Satellite Applications Catapult,” [Online]. Available: <https://sa.catapult.org.uk/>. [Accessed 31 08 2022].
- [48] SpaceX Starlink, “Starlink for RVs,” 2022. [Online]. Available: <https://www.starlink.com/rv>. [Accessed 19 08 2022].
- [49] Autorité de Régulation des Communications Électroniques, des Postes et de la Distribution de la Presse (ARCEP), “Décision n° 2022-1102: de l’Autorité de régulation des communications électroniques, des postes et de ladistribution de la presse en date du 25 mai 2022,” 25 05 2022. [Online]. Available: https://www.arcep.fr/uploads/tx_gsavis/22-1102.pdf. [Accessed 19 08 2022].
- [50] O. Kutkov, “Inside the new square Starlink terminal.,” 18 05 2022. [Online]. Available: <https://twitter.com/olegkutkov/status/1526986473114935298>. [Accessed 19 08 2022].
- [51] O. Kutkov, “Closer inspection of the square Starlink Dishy antenna array.,” 08 15 2022. [Online]. [Accessed 19 08 2022].

- [52] O. Wilks, "Photos of a Gen 3 rectangle dishy (gravity disassembled)...," 02 03 2022. [Online]. Available: <https://www.facebook.com/groups/446129073286883/posts/643823606850761/>. [Accessed 19 08 2022].
- [53] M. Sheetz, "SpaceX does not plan to add 'tiered pricing' for Starlink satellite internet service, president says," 06 04 2021. [Online]. Available: <https://www.cnbc.com/2021/04/06/spacexs-shotwell-no-plan-for-tiered-starlink-internet-pricing.html>. [Accessed 05 01 2023].
- [54] Amazon Project Kuiper, "Custom-built antenna architecture will allow Amazon to deliver a small, affordable customer terminal to connect unserved and underserved communities around the world.," Amazon, 16 12 2020. [Online]. Available: <https://www.aboutamazon.com/news/innovation-at-amazon/amazon-marks-breakthrough-in-project-kuiper-development>. [Accessed 19 08 2022].
- [55] Amazon, "Amazon's Project Kuiper satellites will fly on the new Vulcan Centaur rocket in early 2023," 12 10 2022. [Online]. Available: <https://www.aboutamazon.com/news/innovation-at-amazon/amazons-project-kuiper-satellites-will-fly-on-the-new-vulcan-centaur-rocket-in-early-2023>. [Accessed 05 01 2023].
- [56] C. P. Scarborough, J. P. Turpin, D. F. DiFonzo and J. Finney, "Lens antenna system". United States Patent US20200144719A1, 7 05 2020.
- [57] ALL.SPACE, "Homepage," ALL.SPACE, 2022. [Online]. Available: <https://all.space/>. [Accessed 19 08 2022].
- [58] Ensilica, "EnSilica to Develop Next-Generation Ka Band Satellite Transceivers for the European Space Agency," 30 01 2020. [Online]. Available:

<https://www.ensilica.com/news/ensilica-to-develop-next-generation-ka-band-satellite-transceivers/>. [Accessed 05 01 2023].

- [59] J. Sumantyo, K. Ito and M. Takahashi, "Dual-band circularly polarized equilateral triangular-patch array antenna for mobile satellite communications," *IEEE Trans. on Antennas and Propag.*, vol. 53, no. 11, pp. 3477 - 3485, 2005.
- [60] E. Ezhilarasan and M. Dinakaran, "A Review on Mobile Technologies: 3G, 4G and 5G," in *2017 Second Int. Conf. on Recent Trends and Challenges in Computational Models (ICRTCCM)*, Tindivanam, India, 2017.
- [61] M. D. Dangut and Z. Skaf, "An integrated machine learning model for aircraft components rare failure prognostics with log-based dataset," *ISA Trans.*, vol. 113, pp. 127-139, 2019.
- [62] P. Schoberg, "Secure ground-based remote recording and archiving of aircraft "Black Box" data," in *Ph.D dissertation*, Monterey, CA., Naval Postgraduate School, 2003.
- [63] C. Brenninkmeijer and et al., "Civil Aircraft for the regular investigation of the atmosphere based on an instrumented container: The new CARIBIC system," *Atmos. Chem. Phys.* , vol. 7, p. 4953–4976 , 2007.
- [64] H. Marques, P. Marques, J. Ribeiro, T. Alves and L. Pereira, "Experimental Evaluation of Cellular Networks for UAV Operation and Services," in *2019 IEEE 24th Int. Workshop on Comput. Aided Modeling and Design of Communication Links and Networks (CAMAD)*, Limassol, Cyprus, 2019.
- [65] 3GGP, "3rd generation partnership project; technical specification group services and system aspects; release 15," 2020. [Online]. Available: https://www.3gpp.org/ftp/Specs/archive/21_series/21.915/21915-f00.zip. [Accessed 09 08 2022].

- [66] F. Yang, X. Zhang, X. Ye and Y. Rahmat-Samii, "Wide-band E-shaped patch antennas for wireless communications," *IEEE Trans. Antennas Propag.*, vol. 49, no. 7, pp. 1094-1100, 2001.
- [67] R. Chair, C.-L. Mak, K.-F. Lee, K.-M. Luk and A. Kishk, "Miniature wide-band half U-slot and half E-shaped patch antennas," *IEEE Trans. on Antennas and Propag.*, vol. 53, no. 8, pp. 2645-2652, 2005.
- [68] L. Ping, C. Chakrabarty and R. Khan, "Design of ultra wideband slotted microstrip patch antenna," in *2009 IEEE 9th Malaysia Int. Conf. on Commun. (MICC)*., Kuala Lumpur, Malaysia, 2009.
- [69] H. Nakano, K. Nogami, S. Arai, H. Mimaki and J. Yamauchi., "A spiral antenna backed by a conducting plane reflector," *IEEE Trans. on Antennas and Propag.*, vol. 34, no. 6, pp. 791-796, 1986.
- [70] T. Chen and G. Huff, "Stripline-Fed Archimedean Spiral Antenna," *IEEE Antennas and Wireless Propag. Lett.*, vol. 10, pp. 346-349, 2011.
- [71] H. Nakano, R. Satake and J. Yamauchi, "Extremely low-profile, single-arm, wideband spiral antenna radiating a circularly polarized wave," *IEEE Trans. on Antennas and Propag.*, vol. 8, no. 5, pp. 1511-1520, 2010.
- [72] C. Christodoulou, Y. Tawk, S. Lane and S. Erwin, "Reconfigurable Antennas for Wireless and Space Applications.," *Proc. of the IEEE.* , vol. 100, no. 7, pp. 2250-2261, 2012.
- [73] A. Mehta and D. Mirshekar-Syahkal, "Spiral antenna with adaptive radiation pattern under electronic control," *IEEE Antennas and Propag. Soc. Symp.*, pp. 843-846, 2004.
- [74] B. Falkner, H. Zhou, A. Mehta, T. Arampatzis, D. Mirshekar-Syahkal and H. Nakano, "A circularly polarized low-cost flat panel antenna array with a high impedance surface

- meta-substrate for satellite on-the-move medical IoT applications,” *IEEE Trans. on Antennas and Propag.*, vol. 69, no. 9, pp. 6076-6081, 2021.
- [75] H. Fang, R. Balakrishnan, K. Mouthaan and R. Guinvarc'h, “Wideband dual-circular polarized spiral antenna phased array,” *2015 IEEE Int. Symp. on Antennas and Propag. & USNC/URSI Nat. Radio Sci. Meeting.*, pp. 21-22, 2015.
- [76] A. Hovsepian, E. Alwan and J. Volakis, “A wideband, scanning array of four-arm spiral elements for simultaneous transmit and receive,” *IEEE Antennas and Wireless Propag. Lett.*, vol. 19, no. 4, pp. 537-541, 2020.
- [77] I. Hinojosa Sáenz, R. Guinvarc'h, L. Haupt and K. Louertani, “A 6:1 bandwidth, low-profile, dual-polarized ring array of spiral antennas with connecting arms,” *IEEE Trans. Antennas Propag.*, vol. 64, no. 2, p. 752–756, 2016.
- [78] H. Zhang, S. Yang, Y. Chen, J. Guo and Z. Nie, “Wideband dual-polarized linear array of tightly coupled elements,” *IEEE Trans. on Antennas and Propag.*, vol. 66, no. 1, pp. 476-480, 2018.
- [79] J. X. Sun, Y. J. Cheng and Y. Fan, “Planar ultra-wideband and wide-scanning dual-polarized phased array with integrated coupled-marchand balun for high polarization isolation and low cross-polarization,” *IEEE Trans. on Antennas and Propag.*, vol. 69, no. 11, pp. 7134-7144, 2021.
- [80] N. H. Noordin, A. O. El-Rayis, N. Haridas, B. Flynn, A. T. Erdogan and T. Arslan, “Triangular lattices for mutual coupling reduction in patch antenna arrays,” in *2011*, Loughborough, 2011.
- [81] W.-M. Zou, S.-W. Qu and S. Yang, “Wideband wide-scanning phased array in triangular lattice with electromagnetic bandgap structures,” *IEEE Antennas and Wireless Propag. Lett.*, vol. 18, no. 3, pp. 422-426, 2019.

- [82] S. Hwangbo, H. Y. Yang and Y.-K. Yoon, "Mutual coupling reduction using micromachined complementary meander-line slots for a patch array antenna," *IEEE Antennas and Wireless Propag. Lett.*, vol. 16, pp. 1667-1670, 2017.
- [83] J. Tang, F. Faraz, X. Chen, Q. Zhang, Q. Li, Y. Li and S. Zhang, "Metasurface superstrate for mutual coupling reduction of large antenna arrays," *IEEE Access*, vol. 8, pp. 126859 - 126867, 2020.
- [84] K. Zhang, Y. Wang, S. N. Burokur and Q. Wu, "Generating dual-polarized vortex beam by detour phase: from phase gradient metasurfaces to metagratings," *IEEE Trans. on Microwave Theory and Techniques*, vol. 70, no. 1, pp. 200-209, 2022.
- [85] J.-C. S. Chieh, E. Yeo, R. Farkouh, A. Castro, M. Kerber, R. B. Olsen, E. J. Merulla and K. S. Sharma, "Development of flat panel active phased array antennas using 5G silicon RFICs at Ku- and Ka-bands," *IEEE Access*, vol. 8, pp. 192669-192681, 2020.
- [86] Avient Corporation, "Dielectric materials with ultra-low losses even at mmWaves," [Online]. Available: <https://www.preperm.com/>. [Accessed 04 09 2022].
- [87] Starlink, "Order Starlink," [Online]. Available: <https://www.starlink.com/>. [Accessed 01 05 2023].